DOCTORAL THESIS

Defended by

Thi Thanh Ngan NGUYEN

To obtain the title of

PhD OF ÉCOLE NORMALE SUPÉRIEURE DE CACHAN

Domain

PHYSICS

Thesis title

Fabrication and optimization of polymer-based photonic structures and applications to nonlinear optics

Examining committee

Chia Chen HSU	Professor (National Chung Cheng Univ., Taiwan)	Referee
Sophie BRASSELET	Research director (Institut Fresnel, CNRS)	Referee
Pascal BALDI	Professor (Université de Nice Sophia Antipolis)	Examinator
Joseph ZYSS	Professor (ENS Cachan)	Director
Ngoc Diep LAI	Associate Professor (ENS Cachan)	Co-director
Quang Liem NGUYEN	Professor (IMS, VAST, Vietnam)	Supervisor

Laboratoire de Photonique Quantique et Moléculaire (UMR 8537 CNRS)

École Normale Supérieure de Cachan, France

September 2015

Acknowledgements

First and foremost, I would like to express my sincere appreciation and deepest gratitude to my supervisors, Professor Joseph ZYSS, Associate Professor Ngoc Diep LAI and Professor Quang Liem NGUYEN for their encouragement, guidance and support during my thesis. Especially, Associate Professor LAI, you have been a tremendous mentor for me.

My sincere thanks also goes to Professor Isabelle LEDOUX-RAK who provided me encouraging and also financial supporting when my scholarship ending. I would like to thank the staffs and colleagues at LPQM, Cachan for their insightful comments and discussions throughout my study.

I would also like to thank all of my friends who supported me in my life, in writing, and aids me to strive towards my goal.

A special thanks to my family. Words cannot express how grateful I am to my mother-in law, father-in-law, my mother, and father, my brothers, and my sisters for all of the sacrifices that you've made on my behalf. At the end I would like express appreciation to my beloved husband Cuong who was always my support in the moments when there was no one to answer my queries.

Abstract

This dissertation deals with the fabrication of various polymer-based photonic structures (PSs) and their applications in nonlinear optics. In the first part, we have demonstrated the fabrication of desired PSs by interference lithography technique. The two-beam interference method is theoretically and experimentally demonstrated as a best choice for fabrication of all kinds of PSs with large and uniform area. Desired 1D, 2D, and 3D, periodic and quasi-periodic PSs are successfully fabricated on SU8 photoresist. We also demonstrated a way to overcome the material's absorption effect, which imposes a limitation of PSs thickness. By adding one more exposure of a uniform laser beam in opposite direction of two interfering beams, the fabricated PSs became more uniform and their thickness increased to 25 μm. A tentative of using low one-photon absorption technique was also realized showing the possibility to obtain a PS with a thickness upto 600 μm. Furthermore, by using the interference technique combined with mass transport effect, we have demonstrated the fabrication of desired surface relief grating structures, with a controllable depth, on passive polymer (SU8) and active polymer (DR1/PMMA). In the second part, we applied these fabricated structures for enhancement of nonlinearity of polymer materials by two different ways: quasi-phase-matching (QPM) and waveguide resonance grating (WRG). Both theoretical calculation and experimental realization of these techniques have been investigated. The QPM structures allowed to overcome the phase mismatch of fundamental and harmonic waves, thus increasing the conversion efficiency. The second-harmonic generation (SHG), one of the most important applications of frequency conversion, is significantly enhanced thanks to the QPM condition. Another method basing on the WRG structures allowed to increase the intensity of fundamental wave, thus enhancing the SHG signal by a factor of 25.

Résumé

Ce travail porte sur la fabrication des structures photoniques (SPs) à base de polymères et leurs applications en optique non-linéaire. Dans la première partie, nous avons démontré la fabrication des SPs souhaitées par la méthode d'interférence. En particulier, l'interférence de deux faisceaux laser avec une exposition multiple est démontrée théoriquement et expérimentalement comme un meilleur choix pour la fabrication des structures souhaitées, qui sont uniformes et de grande taille. Diverses structures à 1D, 2D, et 3D, périodiques et quasi-périodiques sont fabriquées avec succès dans la résine SU8. Nous avons également démontré un moyen pour surmonter l'effet d'absorption de la photorésine, qui impose une limitation de l'épaisseur des structures, en ajoutant un faisceau laser uniforme en sens opposé par rapport à deux faisceaux d'interférence. Les SPs fabriquées deviennent plus uniformes et leur épaisseur augmente jusqu'à 25 μm. Une autre approche utilisant la méthode d'absorption ultra-faible à un photon a également été mise en oevre montrant la possibilité d'obtenir des SPs avec une épaisseur jusqu'à 600 μm. De plus, en utilisant la technique d'interférence et l'effet de transport de masse, nous avons également démontré la fabrication des structures à relief de surface (SRG), avec une profondeur contrôlable, dans des polymères passives (SU8) et des polymères actives (DR1/PMMA). Dans la deuxième partie, nous avons utilisé ces structures pour l'amélioration de la génération de seconde harmonique des matériaux polymères par deux manières différentes: quasi-accord de phase (QPM) et mode de résonance de guide d'onde (WRG). Les structures de QPM permet de surmonter le déphasage entre les ondes fondamentale et harmonique, et par conséquence augmente le rendement du taux de conversion. En outre, les structures de guide d'onde avec une surface modulée (WRG) ont également été démontrées comme une excellente méthode permettant d'amplifier le signal de SHG par un facteur de 25.

List of publications **(related to this work)**

- M. H. Luong, **T. T. N. Nguyen**, C. T. Nguyen, I. Ledoux-Rak, and N. D. Lai, *"Study of all-polymer-based waveguide resonant grating and its application for optimization of second-harmonic generation"*, J. Appl. Phys. D., **48**, 365302 (8pp) (2015).

- M. T. Do, Q. Li, **T. T. N. Nguyen**, H. Benisty, I. Ledoux-Rak, and N. D. Lai, *"High aspect ratio submicrometer two-dimensional structures fabricated by one-photon absorption direct laser writing"*, Microsystem Technologies (Springer-Verlag) **20**, 2097-2102 (2014).

- M. T. Do, **T. T. N. Nguyen**, Q. Li, H. Benisty, I. Ledoux-Rak, and N. D. Lai, *"Submicrometer 3D structures fabrication enabled by one-photon absorption direct laser writing"*, Opt. Express **21**, 20964-20973 (2013).

- **T. T. N. Nguyen**, Q. L. Nguyen, J. Zyss, I. Ledoux-Rak, and N. D. Lai, *"Optimization of thickness and uniformity of photonic structures fabricated by interference lithography"*, Appl. Phys. A - Materials Science & Processing **111**, 297-302 (2013).

- X. Wu, **T. T. N. Nguyen**, I. Ledoux-Rak, C. T. Nguyen, and N. D. Lai, *"Optically formation of one- and two-dimensional holographic surface relief grating"*, Chapter 7, "Holography - Basic principles and Contemporary applications", INTECH book, 147-170 (2013).

- X. Wu, **T. T. N. Nguyen**, D. Sun, I. Ledoux-Rak, C. T. Nguyen, and N. D. Lai, *"Incoherent UV/VIS lasers assisted surface relief grating formation"*, Advanced Materials Research **560-561**, 456-461 (2012).

- X. Wu, **T. T. N. Nguyen**, I. Ledoux-Rak, C. T. Nguyen, and N. D. Lai, *"UV beam-assisted efficient formation of surface relief grating on azobenzene polymers"*, Appl. Phys. B - Laser and Optics **107**, 819-822 (2012).

Conference contributions

- T. T. N. Nguyen, M. H. Luong, M. T. Do, D. M. Kieu, Q. Li, D. T. T. Nguyen, Q. C. Tong, I. Ledoux-Rak, and N. D. Lai, *"Micro and nanostructuration of polymer materials and applications"*, Invited Paper, Proc. SPIE 9171, Nanobiosystems: Processing, Characterization, and Applications VII, 91710O (August 2014).

- T. T. N. Nguyen, Q. L. Nguyen, J. Zyss, I. Ledoux-Rak, and N. D. Lai, *"Optimisation de l'épaisseur et de l'uniformité des structures photoniques fabriquées par interférence"*, Oral, OPTIQUE Paris (2013).

- M. T. Do, Q. Li, T. T. N. Nguyen, H. Benisty, I. Ledoux-Rak, and N. D. Lai, *"One-photon absorption direct laser writing: a novel approach for fabrication of three-dimensional sub-micrometric structures"*, Oral, CLEO/Europe-IQEC, Munich, Germany (May 2013).

- M. T. Do, Q. Li, T. T. N. Nguyen, H. Benisty, I. Ledoux-Rak, and N. D. Lai, *"Fabrication of sub-micrometer 3D structures by one-photon absorption direct laser writing"*, Poster, The 6th International Workshop on Advanced Materials Science and Nanotechnology (IWAMSN2012), Ha Long Bay, Vietnam (November 2012).

- M. T. Do, Q. Li, T. T. N. Nguyen, H. Benisty, I. Ledoux-Rak, and N. D. Lai, *"Ultra low one-photon absorption (LOPA) microscopy and applications"*, Invited Talk, The 6th International Workshop on Advanced Materials Science and Nanotechnology (IWAMSN2012), Ha Long Bay, Vietnam (November 2012).

- T. T. N. Nguyen, I. Ledoux-Rak, and N. D. Lai, *"Optimization of two-beam interference technique for fabrication of polymer-based 2D and 3D photonic crystals"*, Poster, The 1st AVSE Annual Doctoral Workshop, Paris, France (September 2012).

- M. T. Do, Q. Li, T. T. N. Nguyen, H. Benisty, I. Ledoux-Rak, and N. D. Lai, *"Fabrication of sub-micrometer 3D structures by LOPA direct laser writing"*, Poster, The 1st AVSE Annual Doctoral Workshop, Paris, France (September 2012).

- M. T. Do, Q. Li, T. T. N. Nguyen, H. Benisty, I. Ledoux-Rak, and N. D. Lai, *"Generation of sharper focal spot for super-resolution imaging and nanofabrication"*,

Poster, P34, The French Japanese Workshop - The Nanotech Revolution from Science to Society, Cachan, France (December 2011).

Contents

Abstract iii

Résumé iv

List of publications v

1 Introduction 1

1.1 Photonic structures . . . 1

1.1.1 Photonic crystals (PCs) . . . 3

1.1.2 Quasi-phase matching (QPM) structures . . . 6

1.1.3 Nonlinear photonic crystals (NLPC) . . . 7

1.1.4 Surface relief gratings (SRG) . . . 8

1.2 Polymer-based photonic structures . . . 9

1.2.1 Passive polymers: SU8 photoresist . . . 10

1.2.2 Active polymers: DR1/PMMA azopolymer . . . 12

1.3 Fabrication techniques of photonic structures . . . 14

1.4 Motivation and thesis plan . . . 15

2 Fabrication of large and uniform polymer microstructures by interference techniques 19

2.1 Fabrication of SU8-based photonic structures by multi-beam interference . 20

2.1.1 Overview . . . 20

2.1.2 Sample preparation and fabrication procedure . . . 21

2.1.3 Fabrication of 2D structures by three-beam interference . . . 23

2.1.4 Three-beam-plus-one interference technique for fabrication of 3D structures . . . 26

2.2 Fabrication of desired 1D, 2D and 3D microstructure by 2-beam interference 29
2.2.1 Theory and simulations . . . 29
2.2.2 Experimental realization . . . 36
2.3 Conclusion and discussion . . . 40

3 Optimization of thickness and uniformity of 2D & 3D microstructures 43
3.1 Influence of absorption effect on structures fabricated by interference technique . . . 43
3.1.1 Absorption characteristics of SU8 . . . 43
3.1.2 Theory of two-beam interference taking into account the absorption effect . . . 45
3.1.3 Influence of exposure dosage on the uniformity and the thickness of fabricated structures . . . 45
3.2 Optimization of film thickness and uniformity . . . 47
3.2.1 Working principle . . . 47
3.2.2 Experimental demonstration . . . 49
3.3 Ultra-low absorption technique . . . 51
3.3.1 Sample preparation . . . 52
3.3.2 Experimental results . . . 53
3.4 Conclusion . . . 55

4 Formation of one- and two-dimensional surface relief gratings 57
4.1 SRG on passive polymer . . . 57
4.1.1 Shrinkage effect . . . 58
4.1.2 Fabrication process . . . 59
4.1.3 Experimental results . . . 61
4.1.4 Discussions . . . 63
4.2 SRG on active polymer . . . 64
4.2.1 Mass transport effect . . . 64
4.2.2 Sample preparation and experimental setup . . . 65
4.2.3 Experimental results . . . 68
4.2.4 Conclusions and Discussions . . . 71

5 Realization of quasi-phase-matching structures and application for second-harmonic generation 75

5.1 Introduction . . . 75

5.2 Theoretical analysis . . . 77

5.2.1 Second-harmonic generation (SHG) effect . . . 77

5.2.2 Quasi-phase matching (QPM) technique . . . 80

5.3 Realization and characterization of QPM structures using DR1/PMMA nonlinear material . . . 89

5.3.1 Sample preparation . . . 89

5.3.2 Creation of $\chi^{(2)}$ by corona poling method . . . 92

5.3.3 Experimental results . . . 94

5.4 Discussions and Conclusions . . . 100

6 Optimization of nonlinear optics effects by waveguide resonance grating (WRG) coupling 104

6.1 Theoretical calculation . . . 105

6.1.1 Property of WRG . . . 105

6.1.2 Numerical calculations . . . 106

6.2 Fabrication and characterization of all-polymer-based WRGs . . . 111

6.2.1 WRGs structure based on copolymer DR1/PMMA . . . 111

6.2.2 Characterization of WRGs . . . 111

6.3 Enhancement of the second-harmonic generation by WRG coupling . . . 115

6.3.1 Dependence of SHG on incident angle (α) . . . 115

6.3.2 Optimization of SHG signal by WRGs . . . 116

6.4 Conclusions . . . 117

Conclusion and Prospects 121

Chapter 1

Introduction

1.1 Photonic structures

Photonic structures exist widely in the natural world. Some insects and birds display beautiful colors that don't come from pigmentation, but due to photonic structures, for example, in Morpho butterfly, there exists discrete multilayers of cuticle and air on their wings. Incident light reflects repeatedly at successive layers, leading to interference effect and thus forming iridescent blue color [1].

Differ from Morpho butterfly, the moth eyes consists of a hexagonal lattice of bumps in nanoscale. This structure allows moth's eyes reflecting very little light at night and therefore not only increases moth's sense of sight but also decreases their detection by nocturnal predators [2]. Figure 1.1(a) shows eyes of a moth and Figure 1.1(b) magnifies them by a scanning electron microscope. The natural photonic structures appear not only in animals but also in plants. In flora, photonic structures are developed to manipulate light on the wavelength scale and produce iridescent and striking colors in leaves, flowers and fruits. For example, pietsnot flower creates regular striations on the petal surface. They have a role as a diffraction gratings (or one-dimensional photonic structure) and cause of the iridescent colours of pietsnot, as illustrated in Figures 1.1(c) and (d). Creating iridescent and striking colors also increase the chance of pollination of flower species and seed dispersal of many fruits. Besides, natural gemstones with iridescent colors, shown in Figures 1.1(e) and (f), also are photonic structures [6]. By observing and imitating nature, many kinds of photonic structures have been proposed and theoretically and ex-

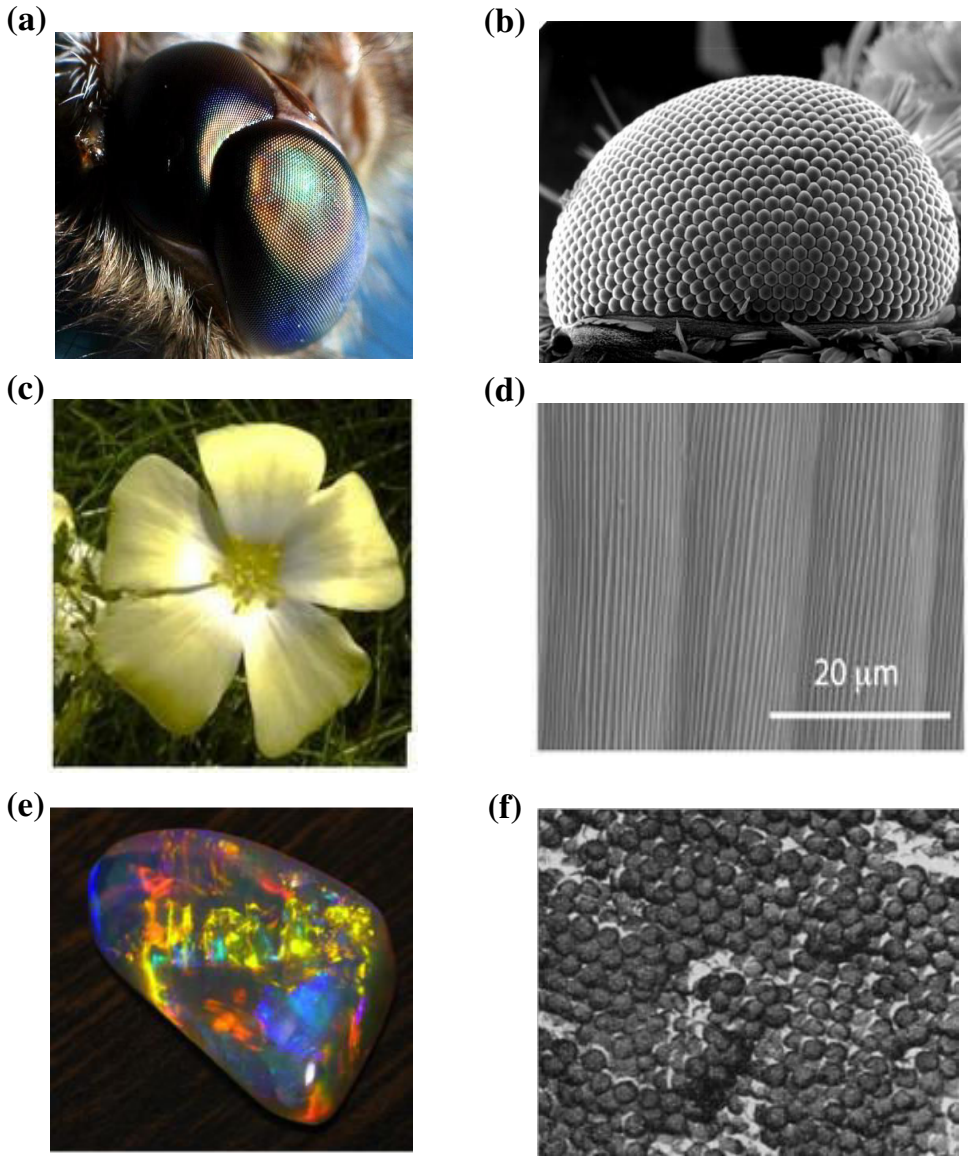


Figure 1.1: Photonic structures in nature. (a) eyes of a moth [2]. (b) SEM image of the moth eye [3], which is constituted by an array of hexagonal pattern of pumps. Each tiny bumps is only 200 to 300 nanometers in height. This structure enable a moth's eye to trap light at different angles. (c) and (d) represent the petal and its SEM image [4]. The iridescent color of the petal is produced by regular striation structure that plays a role as a diffraction grating. (e) and (f) illustrate a gemstone and SEM image obtained from its surface [5]. There are layers, which are arranged hexagonally and can be packed either as a face-centered cubic sequence or a hexagonal close packed sequence.

perimentally studied, which offer many interesting applications, such as second-harmonic gereration as it will be demonstrated in this thesis.

1.1.1 Photonic crystals (PCs)

Photonic crystals (PCs) are artificial optical structures in which the refractive index is modulated periodically in one-dimensional (1D), two-dimensional (2D) and three-dimensional (3D), as illustrated in Figure 1.2, by which photons can be manipulated and controlled.

Although PC structures exist in nature million years ago but human only knew them a century ago as Bragg mirror [7]. In particular, in 1987 Eli Yablonovitch and Sajeev John [8, 9] published two independent papers, which allowed us to understand the natural photonic structures and to fabricate unusual PCs with new optical properties. Yablonovitch proposed that 3D periodic structures could exhibit an electromagnetic bandgap - a range of frequencies at which light can not propagate through structure in any direction. While John showed that if the refractive index contrast of PC structure is sufficiently large, strong light localization can occur, in analogy to the electronic bandgap of semiconductor. Since then PCs have received much attentions owing to the existence of photonic band gap (PBG) and to their unique optical properties. These optical properties depend on periodicity, geometry, refractive index contrast and filling factor of the photonic structure. For example, the width of PBG depends on the refractive index contrast between the high and low refractive indices. The contrast is higher, the width of PBG is wider. The complete PBG also depends strongly on the topology of PC structure, but it's difficult to get a structure with such a complete gap. It only exists in 3D PCs and some kinds of 2D PCs, for example, 2D triangular lattice [10] and hexagonal (honeycomb) structure [11], etc.

Due to the existence of PBG, PC can provide ability to control, bend, trap, reflect and extract the light, which are useful in many applications. A classical application of 1D PC is high quality mirrors. The strong reflection for a certain frequency band of 1D PC was also widely applied, for instance, antireflection coatings, distributed feedback lasers or filters [12–14]. The use of 2D PCs allows to realize many interesting applications, such as: waveguides, fiber, microcavities, light source, optical switching, detectors [15–19]. In particular, 3D PCs are very attractive due to their potential in full confinement of photons

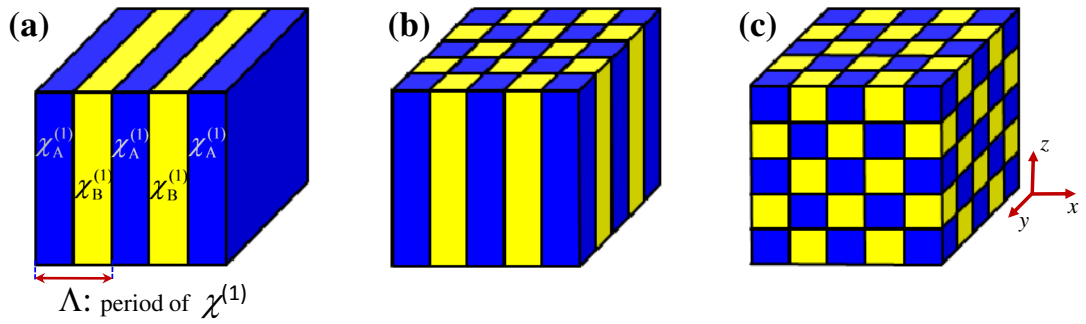


Figure 1.2: Photonic crystal in (a) one-dimensional, (b) two-dimesional, and (c) three-dimensional. The modulation of refractive index (represented by $\chi_A^{(1)}$ and $\chi_B^{(1)}$) was presented by different colors. Λ is called the period of the artificial structures.

and their possibility to control their interaction with materials through complete PBG [20, 21]. However, because of challenging on fabrication of desired 3D structures, there are some restrictions in applications of 3D PCs.

Indeed, while the periodicity arrangement of atoms occurs naturally in semiconductors, PCs need to be fabricated artificially. The properties and the functional spectra range of PCs are determined by their lattice constant. For example, a PC working in the optical range of visible spectrum will possess a period on the order of submicrometer, while PC designed for microwaves has a period at centimeter scale, and PC using in X-rays range should possess a period at several angstroms. So, depending on the working spectra range, the period of PC structure should be chosen appropriately.

1.1.1.1 Photonic band gap (PBG)

In general, the physical nature of the PBG is based on the interference of light. For the frequencies inside the band gap, forward- and backward-propagating components can interfere destructively inside the structure, leading to a complete reflection. Usually, the periodicity of PC structure has the same length-scale as half of the PBG wavelengths. For example, a PC operating in the visible spectrum should have a period in the interval from 200 nm to 350 nm. Figure 1.3(a) shows the band modes of an uniform material (GaAs). As soon as $n_1/n_2 \neq 1$ (we knew that refractive index is related to dielectric

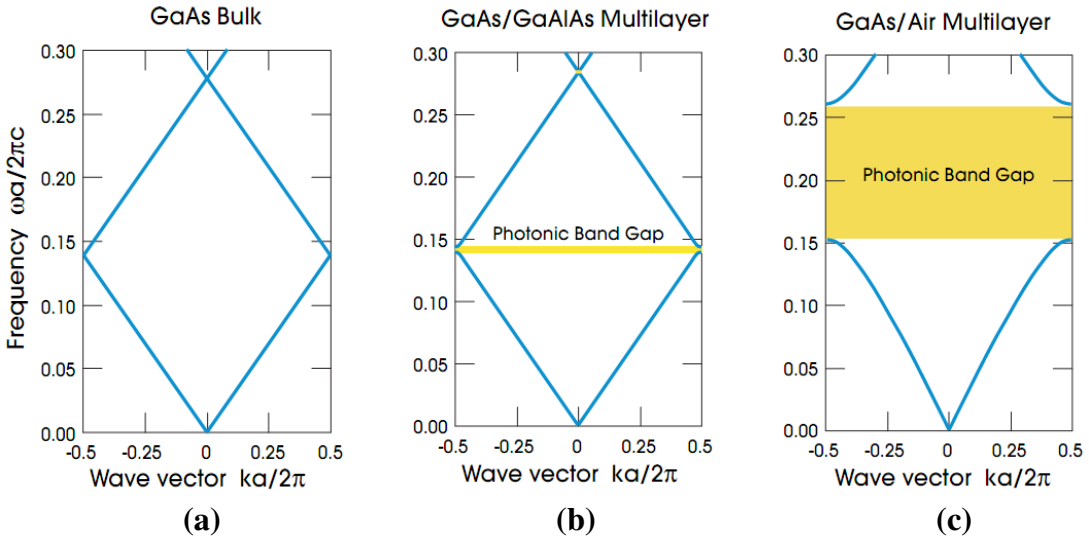


Figure 1.3: Photonic band structure of 1D PC. (a) Homogeneous medium of GaAs bulk ($\varepsilon = 13$). (b) GaAs/GaAlAs multi-layers with $\varepsilon_1 = 13$ and $\varepsilon_2 = 12$. (c) GaAs/Air multi-layers alternate between $\varepsilon_1 = 13$ and $\varepsilon_2 = 1$ [22].

and permeability constants, $n = \sqrt{\varepsilon\mu}$), PBG appears as depicted in Figure 1.3(b) and become wider with a large difference of the dielectric constants between alternate layers as in Figure 1.3(c). Note that 1D structure mostly reflects light in one dimension. It is thus applied for high efficiency mirrors, optical filters ans Bragg grating.

In contrast, 2D PCs, which are modulated along two axes and homogeneous in the third one, can reflect light from any direction in a plane, i.e., in two dimensions. It is therefore applied widely for LED [23, 24], low threshold lasers [25, 26], etc. Besides, 2D PCs also attracted much investigation because they could be made with defects, such as cavities or waveguides by changing or removing a single pillar or a line of pillars. These structures can be integrated into optoelectronic devices for various applications [27–30].

In particular, 3D PC structures allow to achieve a complete PBG, i.e. the light is forbidden in all dimensions. These structures are very interesting for numerous applications (lasers, nonlinear optics, etc) and very rich in optical properties, which can not be obtained with other bulk materials. Thanks to the improvement in fabrication techniques and materials processing, many lattice geometries with small scale of 3D PCs structures

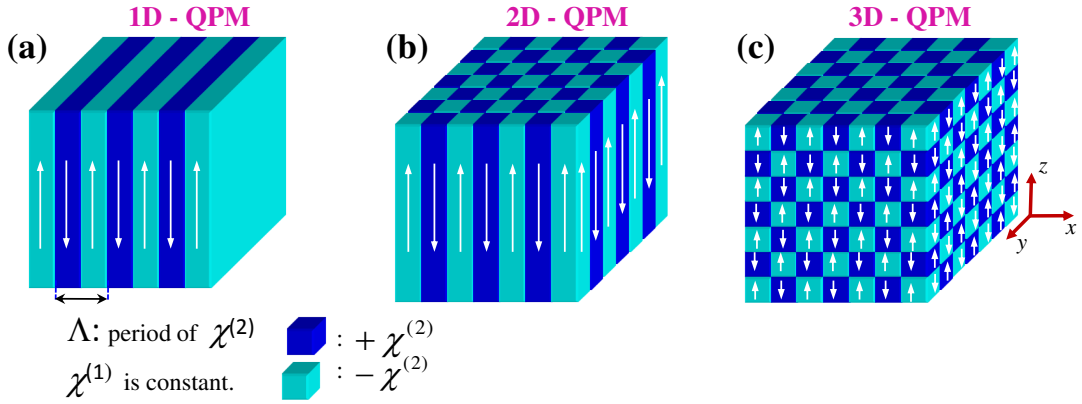


Figure 1.4: QPM structures in (a) one-dimensional, (b) two-dimensional and (c) three-dimensional. The second-order of susceptibility is modulated while the first-order one remains constant. Thus, they do not possess PBG. The nonlinear properties depend only on the configuration of $\chi^{(2)}$ coefficient.

have been reported [31–33]. Nevertheless, fabricating desired 3D PCs still remains as a big challenge, specially for 3D structures working in visible range.

1.1.2 Quasi-phase matching (QPM) structures

In fact, all materials show a nonlinear respond when they are exposed to high enough light intensity. The nonlinear optics effect was first demonstrated by Franken and coworkers [34] just after the invention of the laser in 1960. Nonlinear optics can produce many exotic effects such as frequency conversion, generation of new light source, and optical imaging, etc. The mismatching between the interacting waves propagating inside the nonlinear materials, which originates from material dispersion, is a problem of nonlinear optics. Various techniques have been proposed for optimizing phase matching such as birefringence, quasi-phase matching, modal phase matching, and abnormal dispersion of PCs. Among of them, quasi-phase matching (QPM) technique is a very attractive way for obtaining good phase matching and allowing high efficiency frequency conversion process [35]. In QPM technique, the phase velocity dispersion was compensated by a periodic modulation of the second-order susceptibility, $\chi^{(2)}$, while the linear susceptibility, $\chi^{(1)}$, of the nonlinear material remains constant. Similar to PC, the second-order susceptibility in these structures are modulated in one (1D), two (2D) or three-dimensions (3D), as shown

in Figure 1.4. In this figure, Λ is the lattice constant of QPM structures, which is in the order of several micrometers, much larger than the wavelength of interaction light.

QPM technique has been widely studied in nonlinear optics to enhance nonlinear wave interactions since the first proposed by Armstrong [36] and Franken [37] independently. Originally, QPM was studied in 1D geometry (Figure 1.4(a)), which consists of reversing the sign of the second-order nonlinear susceptibility of the material every coherence length (l_c). However, 1D structure is limited in matching only a single fundamental wavelength and for only one direction [35]. The extension to 2D and 3D QPM structures in which the second-order susceptibility are modulated in two- and three directions (Figure 1.4(b) and (c)), allows phase-matched in multiple directions, and for multiple wavelengths. These structure are therefore useful for non-collinear second harmonic generation, for simultaneous wavelength interchanges, for third and forth harmonic generation, etc. This first 2D QPM structure was proposed by Berger [38] in 1998. Since then, it became more attractive with many studies in both theoretical [39, 40] and experimental [41–43] aspects. Nevertheless, till now the fabrication and characterization of 2D QPM structure remains an open subject. Specially, 3D QPM structure, which provides abundant phase matching directions, still limited to theoretical calculations [44, 45] due to the difficulty in fabrication.

1.1.3 Nonlinear photonic crystals (NLPC)

In recent years, many structures were proposed to compensate for the phase mismatch in nonlinear optical interaction processes. However, the increase of nonlinear conversion efficiency is still a long-standing goal in nonlinear optics. The development of PC brings not only abundant applications in linear optics but also a method to enhance the nonlinear conversion efficiency. There are several ways to use PCs for enhancement of nonlinear optics effect. Many investigations are focused on using photonic band gap edge (PBGE) of PC [46–48], in which frequency of the fundamental wave is fixed near the edge of PBG. Alternatively, it is possible to use a PC with defect mode [49–51] where electromagnetic field is strongly localized around it thus enhancing the nonlinear conversion. The most easy way is to realize PC structures in a nonlinear material, resulting in a so called the nonlinear photonic crystal (NLPC). In this structure, the linear and nonlinear suscepti-

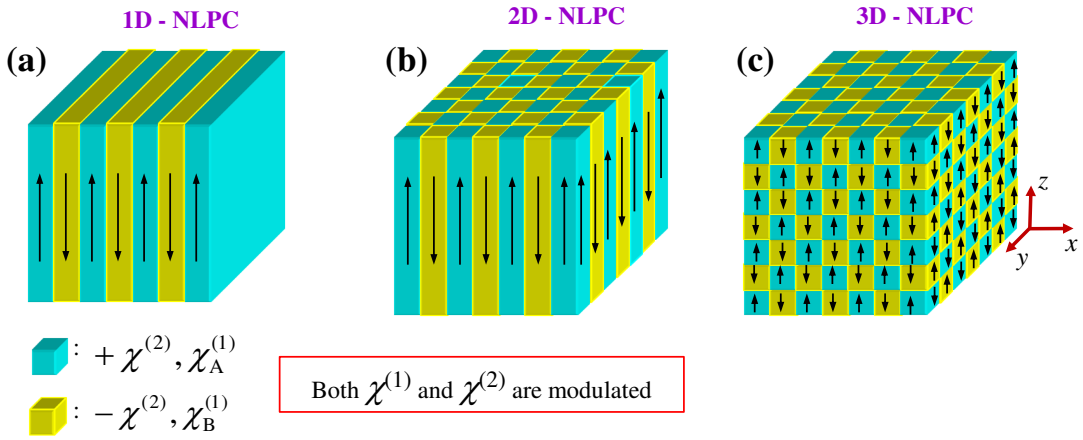


Figure 1.5: Nonlinear photonic crystal in (a) one-dimensional, (b) two-dimesional, and (c) three-dimensional. The modulation takes place with both the first- and the second-order susceptibilities.

bility are both periodically modulated in 1D, 2D or 3D as illustrated in Figure 1.5.

Although, the NLPC is very interesting for nonlinear optics, the use of these structures is still limited due to the fabrication technology.

1.1.4 Surface relief gratings (SRG)

Normally, the modulation of optical parameters of above mentioned photonic structures attains the entire thickness of the material. But there exists one kind of photonic structure, called surface relief grating (SRG) in which the periodical modulation of the material occurs only on the surface. The groove of grating can have sinusoidal, square-wave, triangular, or sawtooth shapes, etc. Similar to other photonic structures, SRGs have different geometries in 1D, 2D and 3D as illustrated in Figure 1.6, with sinusoidally modulated surface shapes. Note that SRG-based 3D structures have not been fabricated yet. Besides, the PCs require a large contrast of refractive index ($n_1/n_2 \gg 1$) in order to possess a PBG, but SRGs can be simply realized in a material of low refractive index, such as polymers [52–54]. SRGs have great attention due to their various applications in quantum electronics such as distributed-feedback laser (DFB) [55–59], waveguide couplers [60], optical filters, etc. They are also easy associated in integrated optics as waveguide

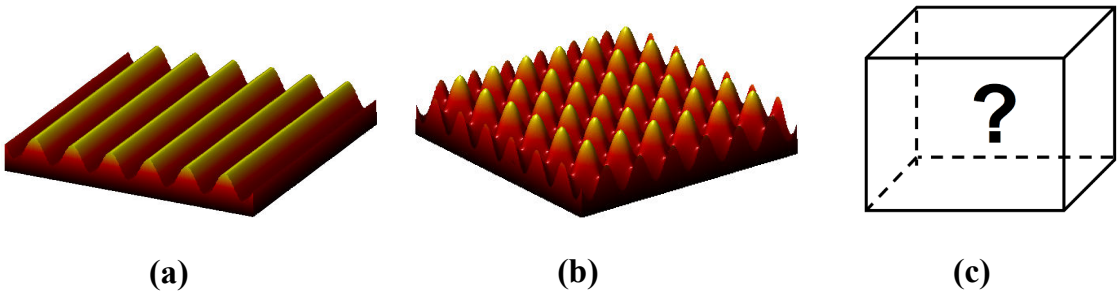


Figure 1.6: Surface relief grating in (a) 1D, (b) 2D, and (c) 3D. Till now, 3D SRG remains as a challenge of fabrication technologies. The modulation of $\chi^{(1)}$ and $\chi^{(2)}$ only occurs in surface.

resonant grating to enhance nonlinear signals [61, 62].

1.2 Polymer-based photonic structures

To possess a full bandgap, PCs are usually made of high refractive index materials such as semiconductor, inorganic materials, which require complex and expensive fabrication technique. While, polymer-based PC do not possess a complete PBG because of the low refractive index contrast, but it could be used in many applications due to simple fabrication, low processing cost, and easy functionalization [63–65]. Besides, it easy to tune their optical properties by optical or electrical way. These polymer structures can be also used as templates to obtain structures with high-index material, which possesses a complete PBG.

Polymers are substances made of recurring structural units, which is called a monomer. Each polymer has very distinct characteristics but most polymers have some general attributes such as: polymer can be both thermal and electrical insulators, polymers can be processed in various ways, in particular by optical lithography. Polymers possess useful optical properties such as photoluminescence and nonlinear optics. We distinguish passive and active polymers, which are both used for fabrication of photonic structures.

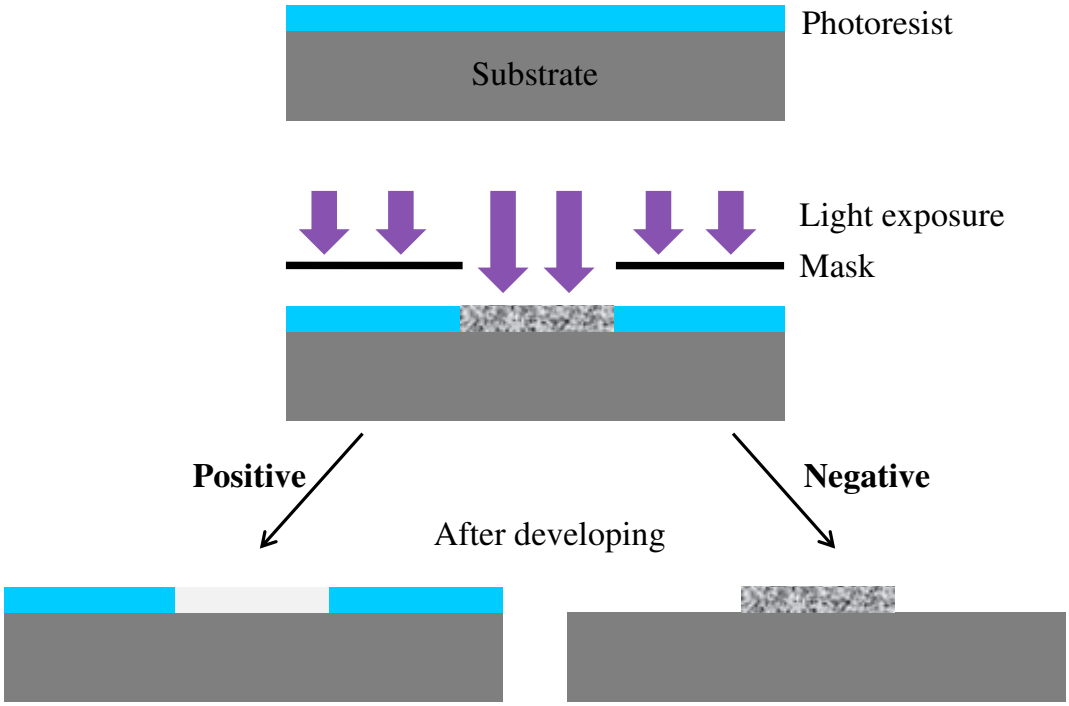


Figure 1.7: Positive and negative photoresists in lithography process.

1.2.1 Passive polymers: SU8 photoresist

Photoresist material is one kind of polymer compound, a typical representative of passive polymers, whose chemical properties change when exposed to ultraviolet light. Photoresists are used widely in the manufacture of microelectronics, microelectromechanical systems (MEMS) and nanoelectromechanical systems (NEMS), etc. Photoresists are divided into two types: positive and negative tones. For positive resists, the chemical structure at the exposed region is changed and become more soluble in the developer solution. Negative resists have the opposite behavior. The exposed region becomes polymerized and more difficult to dissolve. The developer solution removes only the unexposed portions. Figure 1.7 shows the different responses of positive and negative tones after applying lithography process. Each kind of photoresist has own characteristics appropriate for different applications. Negative photoresist seems to be widely used because it provides a good adhesion and tougher films. It is also not sensitive to over developing. SU8 is a kind of negative photoresist, which when exposed to light becomes insoluble to the developer

and the unexposed portion can be dissolved by the developer. Because of high aspect ratio and potential for ultra-thick, SU8, initially, was designed for use in the manufacture of printed circuit boards in MEMS applications by IBM company in 1989. Until 1996, SU8 commercial products was introduced for the first time by MicroChem company. As other photoresists, SU8 consists of three components:

- Resin, "plastic-like" or "glue-like" compound is solid in undiluted state. A single SU8 molecule contains eight epoxy resin groups (EPON SU8 resin, Shell Chemical), as shown in Fig. 1.8. The number "8" in the SU8 means the eight epoxy groups.

- Sensitizer, a kind of photoacid generator (PAG) compound. PAG acts to inhibit (in negative tone) or promote (in positive tone) the dissolution of the resin in the developer. For SU8 it is taken from the family of the triarylium-sulfonium salts.

- Solvent dissolves the resin and keeps the resist in liquid state is gamma-butyrolactone ($C_4H_6O_2$) compound. However, in SU8-2000 series resists, which are widely used recently, cyclopentanone (C_5H_8O) compound is used instead of gamma-butyrolactone. This changing has improved coating and adhesion properties and faster processing time. The quantity of the solvent determines the viscosity and thereby the range of available thickness. For SU8-2000 series, the film thickness is between several hundreds nanometer to 300 μm [66].

The SU8 monomer has low molecular weight so it dissolves easily in solvents and provides a high contrast, high aspect ratio and easily in fabrication. The absorption of SU8 is very low and SU8 films become optically transparent for wavelengths above 400 nm. This is very useful for many optical applications such as waveguides, gratings, PC. The polymerization of SU8 based on cationic photo-polymerization mechanism. When SU8 is exposed to light, the PAG decomposes and generates a strong acid (Lewis acid). This acid acts as a catalyst to ring-open and subsequent cross-linking of the epoxy groups creating a stable three-dimensional network. After this process, SU8 exhibit high mechanical strength and thermal stability. This SU8 photoresist will be used throughout experiments of this thesis.

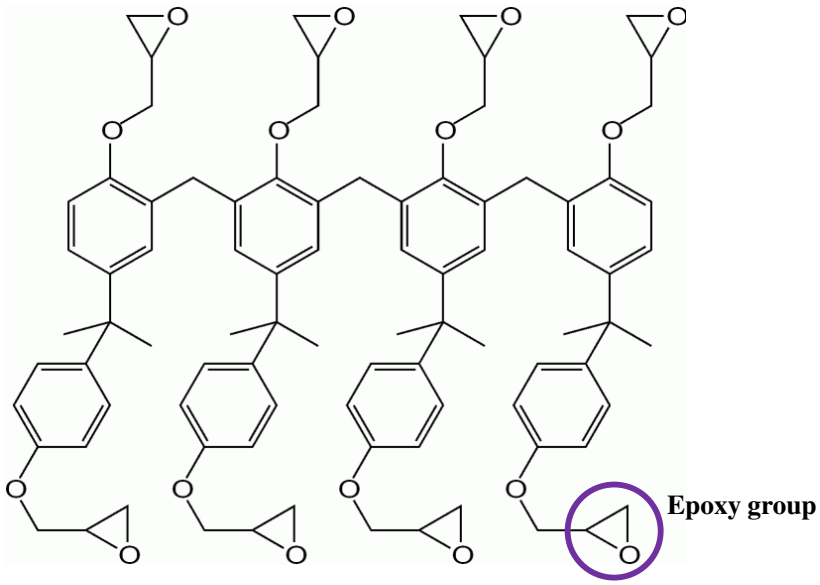


Figure 1.8: The chemical structure of a SU8 molecule with eight epoxy groups

1.2.2 Active polymers: DR1/PMMA azopolymer

Active polymers are also called intelligent polymers. They respond to external stimuli such as an electric field, mechanical energy or light by changing shape or size. Due to these advantages, they have been known and studied for several decades [67, 68]. There are many types of active polymers with different controllable properties depending on the external stimuli. One of them is azopolymer, which includes polymer functionalized with an azobenzene chromophore group. This kind of polymer has various applications as optical storage, integrated optical devices and specially significant applications in nonlinear optics based on photoisomerization of azobenzene group [53, 69, 70]. When illuminated with a polarized light of appropriate wavelength, the azobenzene groups undergo a reversible $trans \Longrightarrow cis \Longrightarrow trans$ isomerization process resulting in an associated orientational redistribution of the chromophores.

In this thesis, the azpolymer DR1/PMMA (polymethylmethacrylate-co-disperse red 1 methacrylate) was used to inscribe the photonic structures. The chemical structure of the commercial copolymer DR1/PMMA is shown in Figure 1.9(a). The DR1 azobenzen group has two isomers *trans* (T) and *cis* (C). The *cis* configuration is less stable than the *trans* configuration. So, DR1 molecules mostly exist in *trans*-form at the ambient temperature.

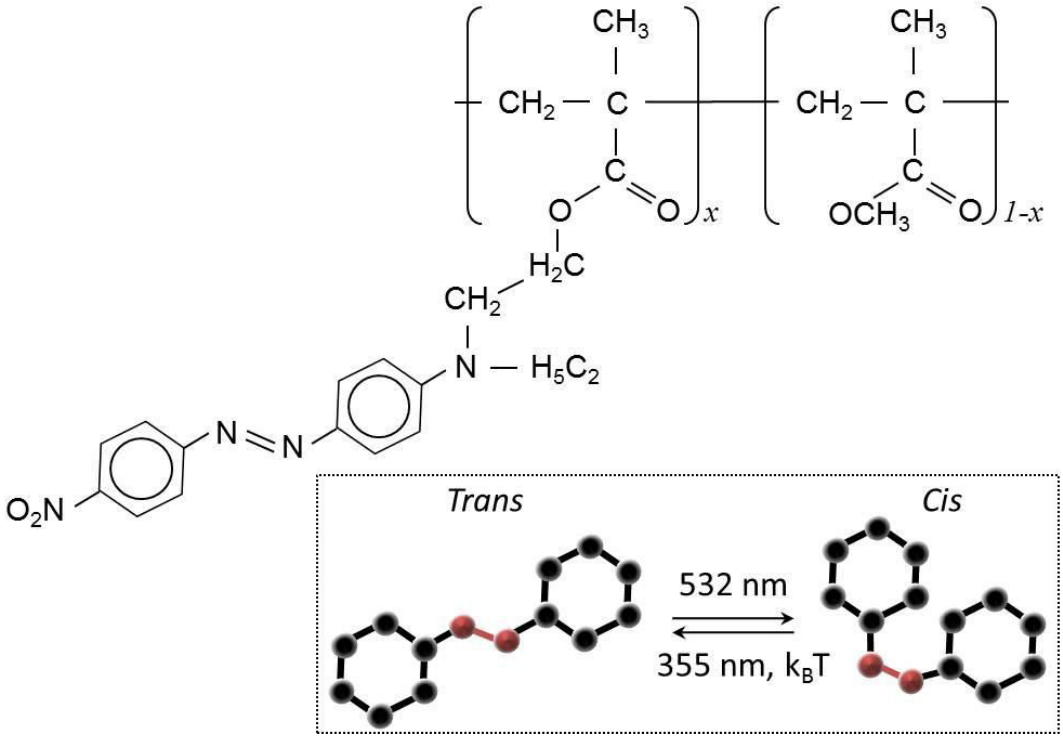


Figure 1.9: (a) A copolymer molecule consists of polymethylmethacrylate (PMMA) and disperse red 1 methacrylate (DR1). (b) State model of azobenzene DR1 molecule. Absorbing the light in the *trans* absorption range (ν), the DR1 molecule will convert from *trans*-form to *cis*-form. The back conversion is occurred when DR1 molecule absorbs the light in the *cis* absorption band (ν') or via thermal relaxation.

Under the excitation of the light in the *trans* absorption range, the azobenzene will convert, with high efficiency, into the *cis*-form. The back conversion, from *cis*-form to *trans*-form, takes place when DR1 molecule absorbs the light in the *cis* absorption band or via thermal back relaxation, as illustrated in Figure 1.9(b). The *trans*-form $\Longleftrightarrow$ *cis*-form photoisomerization process causes rotation motions of DR1/PMMA molecules and leads consequently to their potential applications in photonics [71, 72], optical storage [73] and holographic optical elements.

1.3 Fabrication techniques of photonic structures

The first PCs were fabricated in millimeter scale by simple drill technique [74] and their PBGs are located in microwave regions. Until 1996, Krauss demonstrated for the first time a 2D PC operating at optical wavelength [75]. Since then, there were numerous important applications of PCs working in visible and near-IR regions. This leads to various developments of practical fabrication technologies, also called micro-fabrication. Phase mask lithography has been used very soon for fabrication of 1D PCs [76]. Then it was associated with other techniques for creation of 2D and 3D PCs [77]. Till now, many fabrication techniques are developed together with development of materials science. For instance, PCs based on semiconductor materials require complex and more expensive methods, such as a combination of e-beam lithography [78], nanoimprint lithography [79], and reactive ion etching [80], etc. Thanks to many advantages of polymer-based PCs, various techniques are also adopted to create these structures such as optical lithography by mask, holographic lithography, and direct laser writing, etc. Each method has its own advantage and limitation.

- In optical lithography by mask technique, the photomasks were designed with various patterns, circles, squares, rectangles, etc. This technique does not require complex and sophisticated equipment. Light passing through the mask generates an intensity distribution throughout the thickness of the polymer film. PCs were created after the polymer film absorbed this intensity distribution according to the configuration determined by the photomask pattern [81]. However, there are several drawbacks with this technique, for example, the contact between photomask and polymer film is degraded, the structure along film thickness is non-uniform and it allows to fabricate only 1D and 2D PCs.

- In direct laser writing (DLW), the laser light is tightly focused inside a small volume of the photoresist. The light energy becomes very strong, larger than the threshold of polymerization of photoresist. Initially, DLW is based on multiphoton polymerization of the resist [82–84], then a new approach based on ultralow one-photon absorption is recently developed by the LPQM laboratory [85]. This technique can fabricate any kind of PSs with or without defect with the feature sizes as small

as 100 nm. However, this technique has a limitation that it requires complex and expensive equipment. It is also time-consuming and allows to fabricate structures of small size.

- Holography is one of the main methods used for fabrication of polymer-based PSs, with numerous advantages such as low cost, and capability of producing large-size at high speeds and defect-free PCs templates [86, 87]. In holographic lithography, a photoresist is placed in the multiple-beams interference region and the interference pattern is transferred into the photoresist with a corresponding matter distribution. The resolution of patterns varies from micrometers to sub-100 nanometers. Depending on the number of laser beams and their arrangements, one can fabricate different types of 1D, 2D, and 3D, periodic and quasi-periodic PSs.

Although, there are various research concerning fabrication of PCs, the realization of PCs fulfilling criteria, such as uniform in large area, high quality, and desired periodicity, is still a big challenge for the photonic community. Regarding fabrication techniques, holographic lithography approach seems to be an important and practical one, with many advantages such as cheap, rapid, convenient and effective process. Therefore, fabrication of polymer-based PSs using holographic lithography (interference lithography) method is the heart of this dissertation.

1.4 Motivation and thesis plan

Throughout the last decades, PCs are always the hot topics of scientists in over the world. Besides the attraction of new properties, PCs are also attracted by the flexibility in choosing working range, the diversity in using materials and the appropriate fabrication methods for each kind of materials. Polymer materials, with their ease of fabrication, low temperature processing, and combined with their optical nonlinearities, are potential contenders for PCs applications. In this work, multiple exposures of two-beam interference technique will be investigated to fabricate all 1D, 2D and 3D polymeric PCs. The passive polymer, SU8, will be used for fabrication of desired structures and fabricated structures will be used as templates for PCs and nonlinear applications. However,

the strong absorption in UV range of SU8 leads to the limitation of the uniformity and thickness of fabricated structures. A new technique to optimize this drawback will be proposed. A good template is then associated with active polymer with nonlinear properties (DR1/PMMA) to enhance nonlinear signals through QPM and waveguide resonant grating (WRG) structures.

This thesis is divided into six chapters:

In chapter 1, we introduce the basic concepts and typical photonic structures. Some particular polymer materials and suitable fabrication techniques are analyzed in details, leading to main motivation of the dissertation work.

In chapter 2, we present the theoretical and experimental studies of multi-beam and two-beam interferences techniques. First, we demonstrate the use of a multi-surface prism to create three-beam and four-beam interferences to realize 2D and 3D PCs, respectively. Second, in order to fabricate desired 1D, 2D, 3D structures, we investigate the the use of two-beam interference technique with multiple exposures.

In chapter 3, the influence of absorption of the material on the fabricated PC structures is investigated. We propose a new technique to improve the uniformity and thickness of these structures. The idea is based on the expose of an uniform beam in the opposite direction of two-beam interference, which allows to compensate the diminution of the interference pattern intensity. The use of ultra-low absorption effect is also presented in order to create ultra-thick PCs.

In chapter 4, we investigate the fabrication of surface relief grating (SRG), one simple type of PSs, in both passive and active polymers, whose formation is based on different mechanisms. The interference technique is used to fabricated SRG in all two cases. The characteristics and applications of SRG is also studied.

In chapter 5, one of the most interesting applications of PCs, nonlinear optics based on quasi-phase matching (QPM) technique, is addressed. We investigate in detail the theory theoretical overview of second-harmonic generation (SHG), and the well-known QPM technique for compensate the phase mismatch of the nonlinear processes. The fabrication and characterization 1D and 2D QPM structures will be carried out.

In chapter 6, we demonstrate an alternative method to optimize the SHG efficiency

by using the waveguide resonant grating (WRG) structures. The theoretical calculations, fabrication method and characterization of WRGs are realized, discussed and applied.

In the conclusion, we show all the main results of this work and discuss about their potential prospects.

Chapter 2

Fabrication of large and uniform polymer microstructures by interference techniques

Holographic lithography has been proven as a promising method for fabrication of photonic microstructures [88–90]. The principle of this technique is that the interference pattern is printed onto a photoresist film. After polymerization and development steps, the photonic crystals (PCs) are created. In this chapter, we will first present the use of three-beam interference for fabrication of 2D PCs and three-beam-plus-one interference for fabrication of 3D periodic PCs and quasi-periodic PCs. The interference is realized by using a multi-surface and top-cut prism, which enhances the accuracy of optical setup and is easy to use. Nevertheless, there only one kind of PC possessing one period is fabricated for each designed prism. The period of fabricated 3D PCs is also not similar in three dimensions. We then investigate the two-beam interference method to overcome the shortcomings of above methods. Different 1D, 2D, and 3D structures can be fabricated by such two-beam interference technique by employing multiple exposures.

2.1 Fabrication of SU8-based photonic structures by multi-beam interference

2.1.1 Overview

The variety of 1D grating geometries, one kind of 1D PCs, leads to diverse applications. It can be an important component in spectra analysis, beam splitting or modulation in integrated optics [91, 92]. Many fabrication methods have been developed to obtain desired 1D structures such as photo-mask [76, 93], photo-electrochemical etching [94], electrochemical micromachining [95], and interference lithography (IL). Among these techniques, the IL has a great potential for rapid fabrication of large and uniform patterns and it is easy to control the gratings period. To fabricate 1D PCs, one-exposure of two- beam interference pattern can be used. For 2D or 3D PCs, the number of interfering beams needs to be increased. The fabrication of 2D PCs by IL was first proposed and demonstrated by Berger *et al.* [88] in 1997. By employing the interference of three laser beams, a 2D hexagonal pattern was created on a photoresist, which was then used as a mask to etch the pattern into a high refractive index substrate. This method was then applied for many high-index material to obtain PCS possessing a PBG [96] or associated with other methods to introduce desired defects into 2D PCs [97]. Following this idea, in 2000, Campbell *et al.* [89] have successfully created 3D PC structures by using the interference of three laser beams plus one. The polymeric 3D structure was then filled with Si resulting in a 3D PC with high contrast index. The challenge in fabrication of 3D PC operating in optical range was thus partially resolved. Since then, multi-beam interference technique has been widely employed for fabrication of numerous PCs thanks to their advantages such as low cost, possibility for fabrication of uniform structures with large size and defect-free. Nevertheless, there exists some drawbacks in this multiple beams interference technique. Indeed, the number of laser beams in this method is at least three, so the parameters of the beams (beam angle, beam intensity ratio, polarization, and phase) should be carefully adjusted and the beams alignment presents often some errors. Only a small misalignment of the beams geometry will cause an undesired change of the lattice structure. These problems can be solved by using a compact method as reported in the next session.

2.1.2 Sample preparation and fabrication procedure

Before applying any fabrication technique, we need to prepare the samples. For each technique, the sample preparation procedure is different. To fabricate PCs by the interference method, we used the samples based on SU8 negative tone photoresist. It is the most popular photoresist used in holographic method for PC fabrication. The commercialized SU8 photoresist (Microchem) is sensitive to the light in UV wavelength range. In a series of SU8 the varying solvent contents leads to different viscosities and therefore different thicknesses of the film.

The sample fabrication process is illustrated in Figure 2.1. First, a large cover glass (25 $\times$ 75 mm) is cut into smaller pieces for different experiments. These pieces were immersed in an ultra-sonic bath containing distilled water for 10 minutes to remove all dusts. Then, organic compounds were rinsed off by ultra-sonic cleaning in acetone and iso-propanol (IPA) solutions. The glass substrates are now very clean and ready to use. However, the adhesion between SU8 and glass surface is very poor. To promote the sustainability of this contact, a very thin buffer layer was deposited on glass substrate by spin-coating. Photoresist SU8-2000.5 is spin-coated for a thickness of about 0.5 μm on glass substrate, followed by an exposure to UV irradiation for 30 seconds in an UV box. The cured film was then developed and rinsed to avoid the influence on the main layer. After that, a SU8-2025 film was spin-casted on the top of the polymerized buffer layer, with appropriate parameters (such as speed, acceleration, time, etc) to obtain desired thickness of the film. For 25 μm thickness of the film, 2500 rpm of speed, 300 rpm/s of acceleration and 30 seconds of spin time are needed. The spin-coated films were then soft-baked on a hot plate at 65°C for 3 minutes and at 95°C for 8 minutes to remove all residual solvents. Note that the residual solvent in the film will cause strong acid diffusion and patterns would be washed out as a result. Since the polymerization reaction is affected by the solvent content, the soft bake condition should be consistent for all samples. After soft bake, the films were cooled down to ambient temperature and were stored in a black box before exposure.

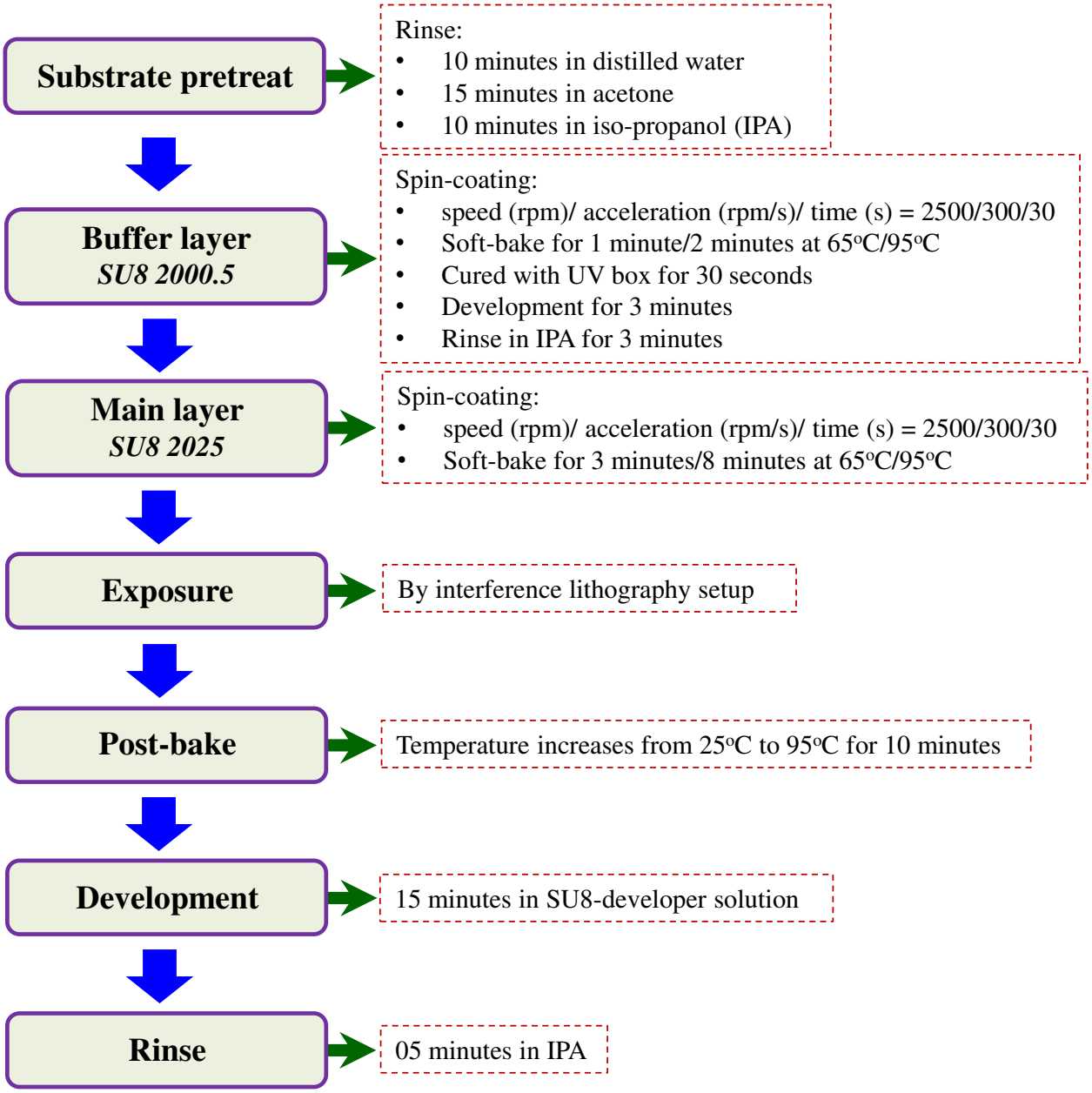


Figure 2.1: Sample preparation and elaboration processes.

2.1.3 Fabrication of 2D structures by three-beam interference

In the first proposal of Berger *et al.*, three diffracted beams were created by a photolithographic mask containing three diffraction gratings, which are oriented by 120° relative to each other. The sample was placed at the overlapping area of the diffraction beams. This method can fabricate various structures by preparing suitable grating masks [98, 99]. Besides, there are other techniques to separate one beam to three coherent beams, such as Fourier gratings [100] or three-pinhole interferometer [101]. In order to avoid alignment complexity and inaccuracies, as well as mechanical vibration instability, we use a multi-surface prism to create three-beam interference.

The prism, also called tri-prism (with the size of 40 x 23.96 x 6.4 mm), possesses three symmetric surfaces and a base, as shown in Figure 2.2(a). A pulsed laser emitting at 355 nm is first extended to about 2 cm in diameter and then sent into the tri-prism surfaces. The laser beam is separated to three coherent beams, represented by the wave vectors $\mathbf{k}_1$, $\mathbf{k}_2$, and $\mathbf{k}_3$, by three surfaces noted A_1, A_2, and A_3, respectively. After passing through the prism, three beams changed their directions and overlapped at a common area. Each beam made an angle θ with respect to the propagation axis (corresponds to the z-axis). A photoresist sample fixed in a holder was placed at the common area of these beams, in which the interference pattern could be recorded by the sample. The interference pattern of three-beam is a 2D hexagonal structure. The sample holder could be rotated around the z-axis by an angle α as shown in Figure 2.2(a). By this way, we can make multi-exposure of the interference pattern corresponding to different α angles for fabrication of 2D quasi-periodic structures (QPSs) with multi-fold symmetry.

2.1.3.1 Theory of three-beam interference

Three coherent beams separated from tri-prism are represented by three plane waves as follow:

$$\mathbf{E}_1(\mathbf{r},t) = \mathbf{E}_{01}e^{i(\mathbf{k}_1\cdot\mathbf{r}-\omega t+\varphi_1)}, \tag{2.1}$$

$$\mathbf{E}_2(\mathbf{r},t) = \mathbf{E}_{02}e^{i(\mathbf{k}_2\cdot\mathbf{r}-\omega t+\varphi_2)}, \tag{2.2}$$

$$\mathbf{E}_3(\mathbf{r},t) = \mathbf{E}_{03}e^{i(\mathbf{k}_3\cdot\mathbf{r}-\omega t+\varphi_3)}, \tag{2.3}$$

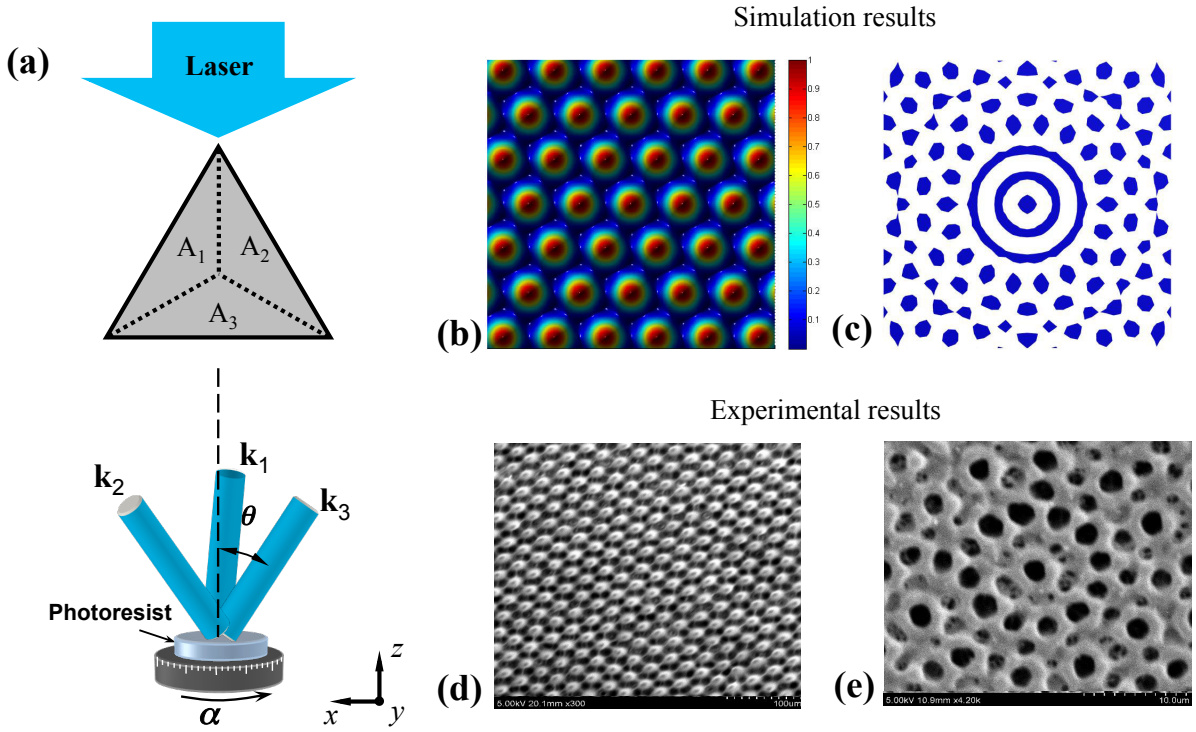


Figure 2.2: (a) Three-beam interference setup by using a multi-surface prism. A large and uniform laser source comes into the prism along the z-axis and it is separated to three coherent beams by three surfaces A_1, A_2, and A_3, represented by the wave vectors $\mathbf{k}_1$, $\mathbf{k}_2$, and $\mathbf{k}_3$, respectively. Three beams after passing through the prism changed their directions and overlapped at a common area in the z-axis. The photoresist sample is placed at the this area and can be rotated by an angle α for each exposure. If the angle α is 0, 2D hexagonal PC structure can be created with one-exposure. (b) and (d) are the simulation and experimental results, respectively, for this case. (c) and (e) are the simulation and experimental results of a 2D QPS formed by three exposures at $\alpha = 0°$, 20° and 40°.

where $\mathbf{k}_1$, $\mathbf{k}_2$, and $\mathbf{k}_3$ are the wave vectors, $\mathbf{E}_{01}$, $\mathbf{E}_{02}$, and $\mathbf{E}_{03}$ are electric field amplitude vectors and φ_1, φ_2, and φ_3 are the initial phases of three beams, respectively. $\mathbf{r}$ is the position vector in the overlapping space. In our simulation, we assumed that $|\mathbf{k}_1| = |\mathbf{k}_2| = |\mathbf{k}_3| = k$ and $|\mathbf{E}_{01}| = |\mathbf{E}_{02}| = |\mathbf{E}_{03}| = E_0$. The circular polarization is applied to all three beams because of the same form throughout the interference pattern and the high intensity modulation. All the initial phases are also assumed zeros ($\varphi_1 = \varphi_2 = \varphi_3 = 0$). The total field in the interference area is the sum of the electric fields of individual plane waves:

$$\mathbf{E}(\mathbf{r}, t) = \mathbf{E}_1(\mathbf{r}, t) + \mathbf{E}_2(\mathbf{r}, t) + \mathbf{E}_3(\mathbf{r}, t). \tag{2.4}$$

The interference intensity is calculated by:

$$I(\mathbf{r}, t) = \langle |\mathbf{E}(\mathbf{r}, t)|^2 \rangle_t. \tag{2.5}$$

With one-exposure, a 2D hexagonal PC can be fabricated. The simulation and experimental results are shown in Figures 2.2(b) and (d). The period of structure (Λ) can be determined by:

$$\Lambda = \frac{2\lambda}{3 \sin\theta}, \tag{2.6}$$

where λ is the wavelength of the laser beam and θ is the angle between each beam to the z-axis. In our case, the θ angle is 17.65^o resulting in a period of 1.2 μm.

Three-beam interference by tri-prism also allows to fabricate 2D QPSs with a high rotational symmetric level by multi-exposure. The relationship between the rotational symmetric level and the exposure parameters can be written as

$$R = 6n; \qquad \alpha_n = 60^\circ/n; \qquad t_n = t_1/n, \tag{2.7}$$

where R is the rotational symmetric level, n is the exposure number; α_n is the rotation angle increment [for example, for n exposures, $\alpha_n(i) = i * (60^\circ/n)$; i = 0,1,2,... $n-1$]; t_n is the exposure time; and t_1 is the exposure time needed to fabricate a hexagonal structure by one-exposure [102].

The exposure dosage is accumulated after each exposure, and the total interference intensity therefore is the sum of the interference intensity of each exposure, which can be expressed as

$$I_{\text{multi-exposure}} = \sum_n I_{\alpha_n(i)}, \tag{2.8}$$

where $I_\alpha(i)$ is the intensity distribution of a three-beam interference pattern in a sample oriented at angle $\alpha_n(i)$.

To model the theory of the interference technique, we used Matlab software, which is a powerful tool for numerical computation and simulation. All the calculations are performed based on the personal code scripts. Figures 2.2(c) and (e) shows the simulation and experimental results of a QPS obtained by three exposures at the angles: $\alpha = 0°$, $20°$, $40°$. In this part, the simulation results present no absorption of material. By increasing the number of exposure, this technique allows us to obtain QPSs with very high rotation symmetry level, e.g. up to 60-fold with 10 exposures [103]. It is worth to mention that this technique does not allows to change easily the period and the geometry of PCs. Each prism is fixed to one kind of PCs, with well-determined periodicity.

2.1.4 Three-beam-plus-one interference technique for fabrication of 3D structures

The first 3D PC created with four-beam interference was reported by Campbell *et al.* in 2000 with an umbrella beam geometry [89]. In such case three outer beams are symmetrically placed around the central beam and make a same angle with it. Face centered cubic-like (fcc-like) structures were fabricated by this configuration. Other structures can be also possible by controlling the polarization, phase, intensity of each beam and the angle between the center beam and three outer beams. For example, to form a diamond-like structure, which possesses a large PBG, this angle should be set at 38.9° [89, 104]. Using a single optical element avoids complicated optical alignment and inaccuracies. So, a single top-cut prism (or tetra-prism) was employed, allowing to simplify the optical setup [105–107].

In our experiments, we used a tetra-prism with the three outer symmetrical beams, which makes an θ angle of 15.7 ° with the central beam as illustrated in Figure 2.3(a). This results in a period of 1.1 μm in the *(xy)* plan of interference pattern. When the large and uniform pulsed laser beam, wavelength $\lambda = 355$ nm, passes though the prism, the beam O (center beam) continues propagating along the z-axis, while the other three beams A_1, A_2, and A_3 (ambient beams) changes their directions and direct towards the

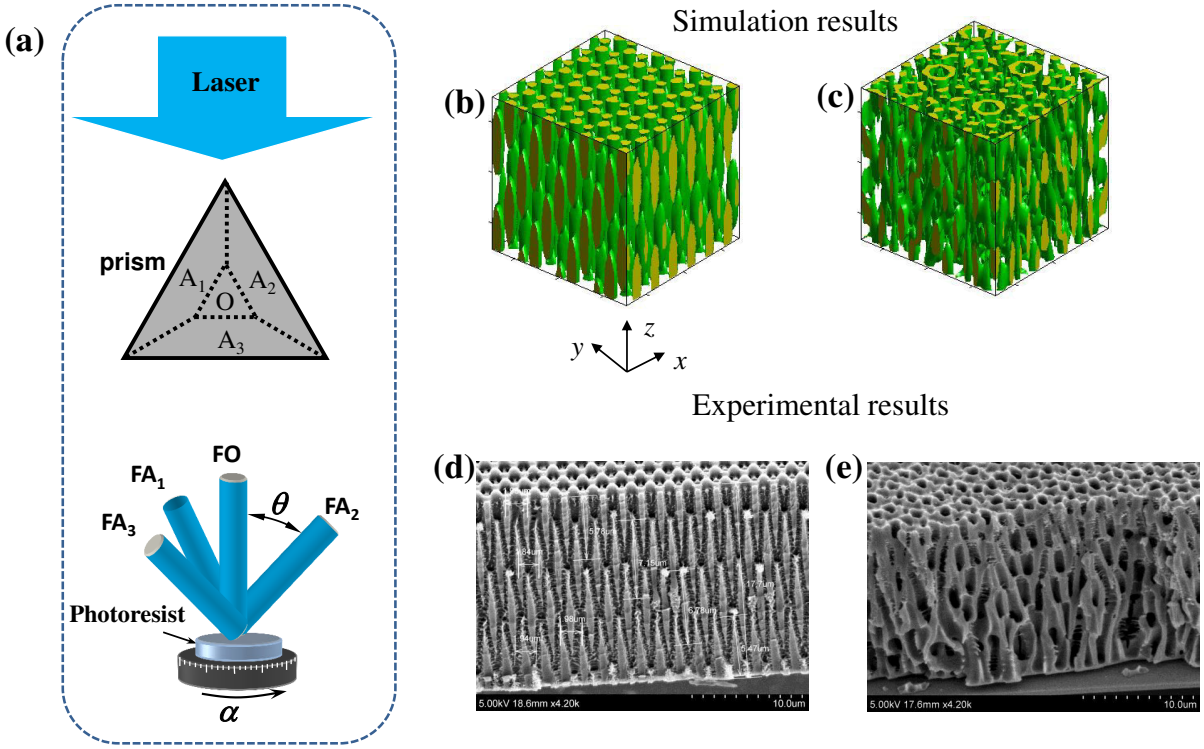


Figure 2.3: (a) Three-beam-plus-one interference realized by a tetra-prism. The central beam propagates along the z-axis while three outer beams, which make an θ angle with it, change their directions and overlap at an area below the bottom surface of the prism. The photoresist sample is placed at this area for recording the interference pattern. (b) and (d) show simulation and experimental results of a fcc-like structure in the case of one-exposure. (c) and (e) present simulation pattern and SEM image of 3D QPS obtained by two exposures at $\alpha = 0°$ and $\alpha = 90°$.

center beam and all overlap at a zone after the bottom surface of the prism. The sample holder that could be rotated around the z-axis by an angle α was placed at the overlapping area of these four laser beams and the interference pattern was recorded into photoresist sample.

Similar to the case of three-beam interference, three outer beams separated from three surfaces of prism are represented by three plane waves as follow:

$$\mathbf{E}_1(\mathbf{r},t) = \mathbf{E}_{01}e^{i(\mathbf{k}_1\cdot\mathbf{r}-\omega t+\varphi_1)}, \tag{2.9}$$

$$\mathbf{E}_2(\mathbf{r},t) = \mathbf{E}_{02}e^{i(\mathbf{k}_2\cdot\mathbf{r}-\omega t+\varphi_2)}, \tag{2.10}$$

$$\mathbf{E}_3(\mathbf{r},t) = \mathbf{E}_{03}e^{i(\mathbf{k}_3\cdot\mathbf{r}-\omega t+\varphi_3)}, \tag{2.11}$$

where the orientations of the wave vectors of the three beams can be defined as:

$$\mathbf{k}_1 = k(-x\sin\theta, 0, -z\cos\theta), \tag{2.12}$$

$$\mathbf{k}_2 = k(0.5x\sin\theta, \sqrt{3}/2y\sin\theta, -z\cos\theta), \tag{2.13}$$

$$\mathbf{k}_3 = k(0.5x\sin\theta, -\sqrt{3}/2y\sin\theta, -z\cos\theta). \tag{2.14}$$

The central beam, which goes along z-axis, is also a plane wave and is represented as:

$$\mathbf{E}_4(\mathbf{r},t) = \mathbf{E}_{04}e^{i(\mathbf{k}_4\cdot\mathbf{r}-\omega t+\varphi_4)}, \tag{2.15}$$

where the wave vector is:

$$\mathbf{k}_4 = k(0, 0, -z\cos 0^o). \tag{2.16}$$

Assuming that all the initial phases are zeros ($\varphi_1 = \varphi_2 = \varphi_3 = \varphi_4 = 0$) and the beams possess circular polarizations, the total intensity given by the interference of these four waves can be written as:

$$I(\mathbf{r},t) = \langle|\mathbf{E}_1(\mathbf{r},t) + \mathbf{E}_2(\mathbf{r},t) + \mathbf{E}_3(\mathbf{r},t) + \mathbf{E}_4(\mathbf{r},t)|^2\rangle_t. \tag{2.17}$$

The periods along coordinate axes are different and depend on θ angle. They can be calculated as follow:

$$\Lambda_x = \Lambda_y = \frac{2\lambda}{3\sin\theta} \qquad \text{and} \qquad \Lambda_z = \frac{\lambda}{(1-\cos\theta)}, \tag{2.18}$$

To fabricate a fcc-like structure, only one exposure is required. Theoretical modeling and experimental results are presented in Figure 2.3. 3D QPSs are also fabricated by two

exposures of the interference pattern at $\alpha = 0°$ and 90°. SEM images of 3D QPSs and corresponding simulation pattern are presented in Figure 2.3(c) and (e). These structures are expected to possess an isotropic gap thanks to their high symmetry level. With the use of such a single optical element, we have produced large-scale, high quality 3D fcc-like and 3D quasi-periodic PC structures. However, the 3D interference pattern obtained by this tetra-prism has longer period in the z direction than those in the x or y directions. As mentioned in previous section, this method also does not allow to fabricate PCs with different periods and geometries.

2.2 Fabrication of desired 1D, 2D and 3D microstructure by 2-beam interference

2.2.1 Theory and simulations

Employing multi-surface prisms to create multi-beam interference overcomes some drawbacks and increase the stability of multi-beam interference technique. Nevertheless, this technique does not allow to fabricate any structure, also its periods are quite different for different directions. Lai *et al.* proposed a method based on two-beam interference with multiple exposures to fabricate different 1D, 2D and 3D PCs [86]. This fabrication method presents a number of advantages over other holographic techniques based on three- or four-beam interference technique, such as, simple, low cost, and flexible, etc. Besides, this method can fabricate not only 1D, 2D and 3D periodic structures but also quasi-periodic structures.

In the case of two-beam interference, illustrated in Fig. 2.4, two collimated beams obtained from a coherence source are sent into a common area where they interfere. The electric fields of these two beams can be represented as:

$$\mathbf{E}_1(\mathbf{r}, t) = \mathbf{E}_{01} e^{i(\mathbf{k}_1 \cdot \mathbf{r} - \omega t + \varphi_1)}, \tag{2.19}$$

$$\mathbf{E}_2(\mathbf{r}, t) = \mathbf{E}_{02} e^{i(\mathbf{k}_2 \cdot \mathbf{r} - \omega t + \varphi_2)}, \tag{2.20}$$

where $\mathbf{k}_1$, $\mathbf{k}_2$ are the wave vectors, $\mathbf{E}_{01}$, $\mathbf{E}_{02}$ are electric field amplitude vectors and φ_1, φ_2 are the initial phase of two beams, respectively. $\mathbf{r}$ is the position vector in the overlapping

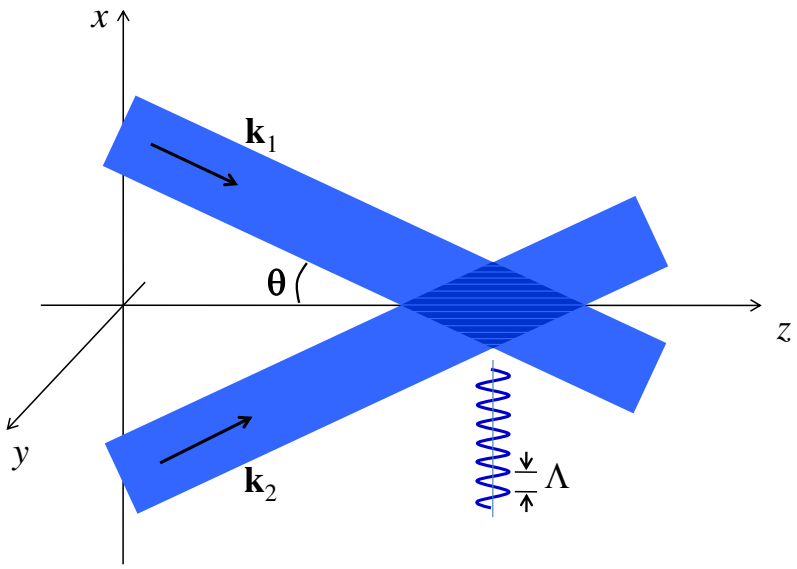


Figure 2.4: Two-beam interference configuration. θ is the angle between each beam and the symmetrical axis (z). The period of interference pattern (Λ) depends on the θ angle and the wavelength of laser beam. The S-S polarizations of two beams were chosen due to the best amplitude modulation (100%) of the intensity pattern.

space. Applying the superposition principle, the total field in the interference area can be calculated by:

$$\mathbf{E}(\mathbf{r},t) = \mathbf{E}_1(\mathbf{r},t) + \mathbf{E}_2(\mathbf{r},t). \tag{2.21}$$

The intensity distribution is calculated by:

$$\begin{aligned} I(\mathbf{r},t) &= \langle |\mathbf{E}(\mathbf{r},t)|^2 \rangle_t \\ &= \langle |\mathbf{E}_1|^2 \rangle_t + \langle |\mathbf{E}_2|^2 \rangle_t + \langle \mathbf{E}_1 \cdot \mathbf{E}_2^* \rangle_t + \langle \mathbf{E}_1^* \cdot \mathbf{E}_2 \rangle_t \\ &= I_1 + I_2 + I_{12}, \end{aligned} \tag{2.22}$$

where I_{12} is the interference term. With the assumption of all the initial phases are zeros, $\varphi_1 = \varphi_2 = 0$, this term can be detailed as:

$$\begin{aligned} I_{12} &= \langle \mathbf{E}_1 \cdot \mathbf{E}_2^* \rangle_t + \langle \mathbf{E}_1^* \cdot \mathbf{E}_2 \rangle_t \\ &= 2\mathbf{E}_{01} \cdot \mathbf{E}_{02} \cos[(\mathbf{k}_1 - \mathbf{k}_2) \cdot \mathbf{r}] \\ &= 2\mathbf{E}_{01} \cdot \mathbf{E}_{02} \cos\delta. \end{aligned} \tag{2.23}$$

When $\mathbf{E}_{01}$ and $\mathbf{E}_{02}$ are perpendicular, $I_{12} = 0$, there will be no interference effect. In the case if $\mathbf{E}_{01}$ and $\mathbf{E}_{02}$ are parallel, the phase difference creates alternative bright and dark bands, which are referred to as interference fringes. Figure 2.5 illustrates this intensity modulation. Total constructive interference (bright fringe) is $I_{\max} = I_1 + I_2 + 2\sqrt{I_1 I_2}$ and total destructive interference (dark fringe) is $I_{\min} = I_1 + I_2 - 2\sqrt{I_1 I_2}$. To get the maximum intensity modulation ($I_{\min} = 0$, $I_{\max} = 1$) of the interference pattern, the S-S polarization configuration, i.e. the polarizations of two beams are parallel to each other and they are perpendicular to the plane made by two beams, is a best choice [108].

The fringe period depends on the angle between the two interfering beams (see Figure 2.4). The period (Λ) of 1D PCs fabricated by one exposure of two-beam interference pattern can be calculated by:

$$\Lambda = \frac{\lambda}{2\sin\theta}, \tag{2.24}$$

where λ is the wavelength of laser source. As the angle between the beams gets larger, the period decreases and can reach $\lambda/2$.

The S-S polarization of two beams will be chosen for all simulations. Figure 2.6(b) shows the simulation result of 1D PC structure fabricated by two-beam interference method.

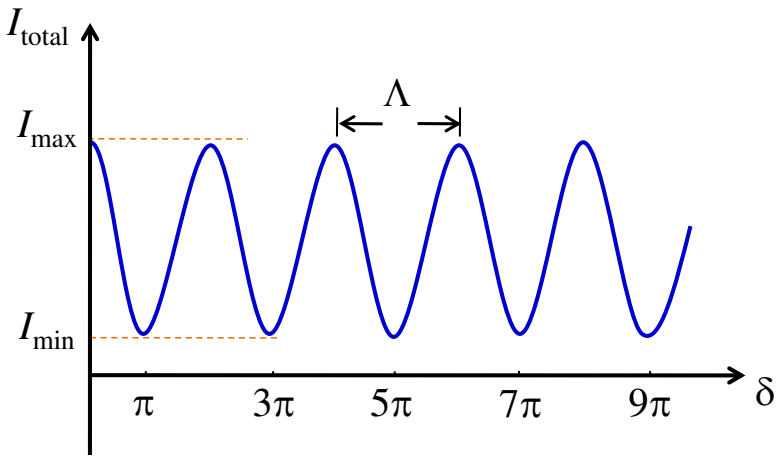


Figure 2.5: The intensity modulation of the two-beam interference pattern as a function of the phase difference between two interfering beams.

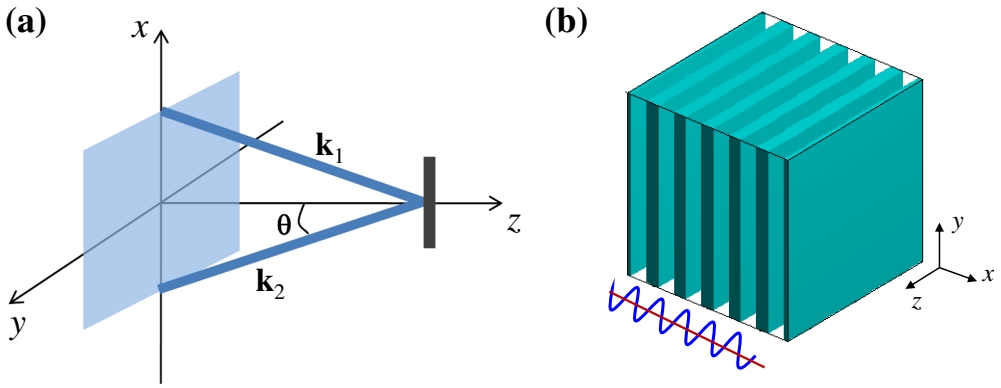


Figure 2.6: (a) Configuration of two-beam interference in case of one exposure. Two beams make the same θ angle with the z-axis. (b) Simulation result of 1D interference pattern obtained by one exposure of two-beam interference.

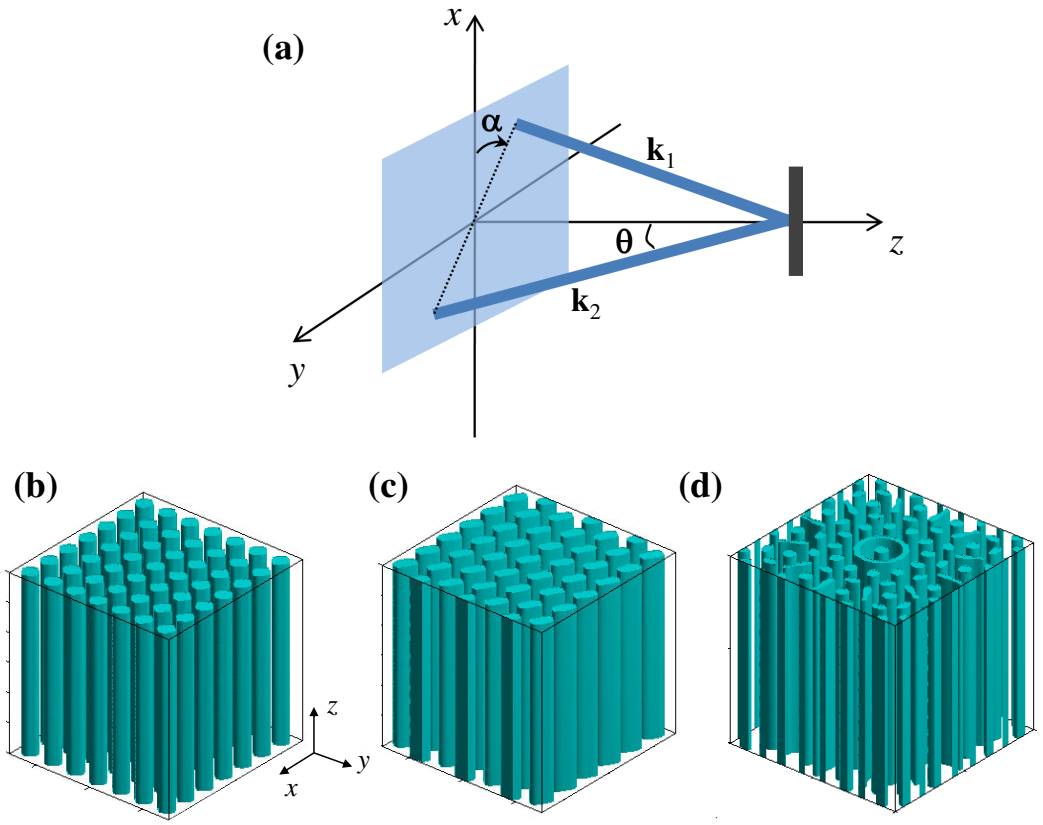


Figure 2.7: (a) Two-beam configuration used for fabrication of 2D PC structures. By rotating the plane containing two beams around z-axis and exposing multiple times, 2D photonic structures can be created. The geometry of structures depends on the rotation angle and the number of exposure. Simulation results of a 2D square structure (b) obtained by two exposures at $\alpha = 0°$ and $\alpha = 90°$ and a 2D hexagonal structure (c) formed by two exposures at $\alpha = 0°$ and $\alpha = 60°$. (d) With six exposures at $\alpha = 0°, 30°, 60°, 90°, 120°$ and $150°$, quasi-periodic structure was obtained.

Traditionally, 2D and 3D structures were created by increasing the number of the beams because the number of the interfering beams determines the dimensionality of the resultant periodic interference pattern. In this work, we demonstrate that by employing multi-exposure of two-beam interference pattern, different types of periodic structures (1D, 2D, and 3D) can be created, depending on the number of exposure and the rotation angle of the sample for each exposure. Theoretically, 2D periodic structure can be fabricated by a combination of the first exposure, which is similar to the 1D case and a second exposure after rotating the plane containing two laser beams by an α angle. The wave vectors of two beams in this case are:

$$\mathbf{k}_1 = k(x\sin\theta\cos\alpha, y\sin\theta\sin\alpha, z\cos\theta), \tag{2.25}$$

$$\mathbf{k}_2 = k(-x\sin\theta\cos\alpha, y\sin\theta\sin\alpha, z\cos\theta), \tag{2.26}$$

and the total intensity of two beams at the α angle becomes:

$$\begin{aligned} I_\alpha &= I_1 + I_2 + I_{12} \\ &= 4E_0^2\cos^2[k(x\cos\alpha + y\sin\alpha)\sin\theta]. \end{aligned} \tag{2.27}$$

When the interference pattern is exposed many times at different α angles, the exposure dose is accumulated and the total interference intensity can be given by:

$$I_{\text{multi-exposure}} = \sum_i I_{\alpha_i}. \tag{2.28}$$

Figure 2.7 shows the simulation results in the case of multiple exposures of two-beam interference. By changing the value of α angle, we obtained different geometries of PC structures. Figure 2.7(b) shows a 2D square structure created by two exposures at $\alpha = 0°$ and $\alpha = 90°$ and Figure 2.7(c) shows a hexagonal structure obtained with $\alpha = 0°$ and $\alpha = 60°$. Specially, when increasing the number of exposures, we can create any 2D QPS on demand. Figure 2.7(d) shows a QPS created by six exposures at α angles: $0°, 30°, 60°, 90°$, $120°$ and $150°$, respectively.

To obtain 3D PC structures, we introduce a second rotation angle β as illustrated in Figure 2.8. We varied both α and β angles for different exposures. The wave vector of two beams in this case is:

$$\mathbf{k}_1 = k(x\sin(\theta-\beta)\cos\alpha, y\sin(\theta-\beta)\sin\alpha, z\cos(\theta-\beta)), \tag{2.29}$$

$$\mathbf{k}_2 = k(-x\sin(\theta+\beta)\cos\alpha, y\sin(\theta+\beta)\sin\alpha, z\cos(\theta+\beta)). \tag{2.30}$$

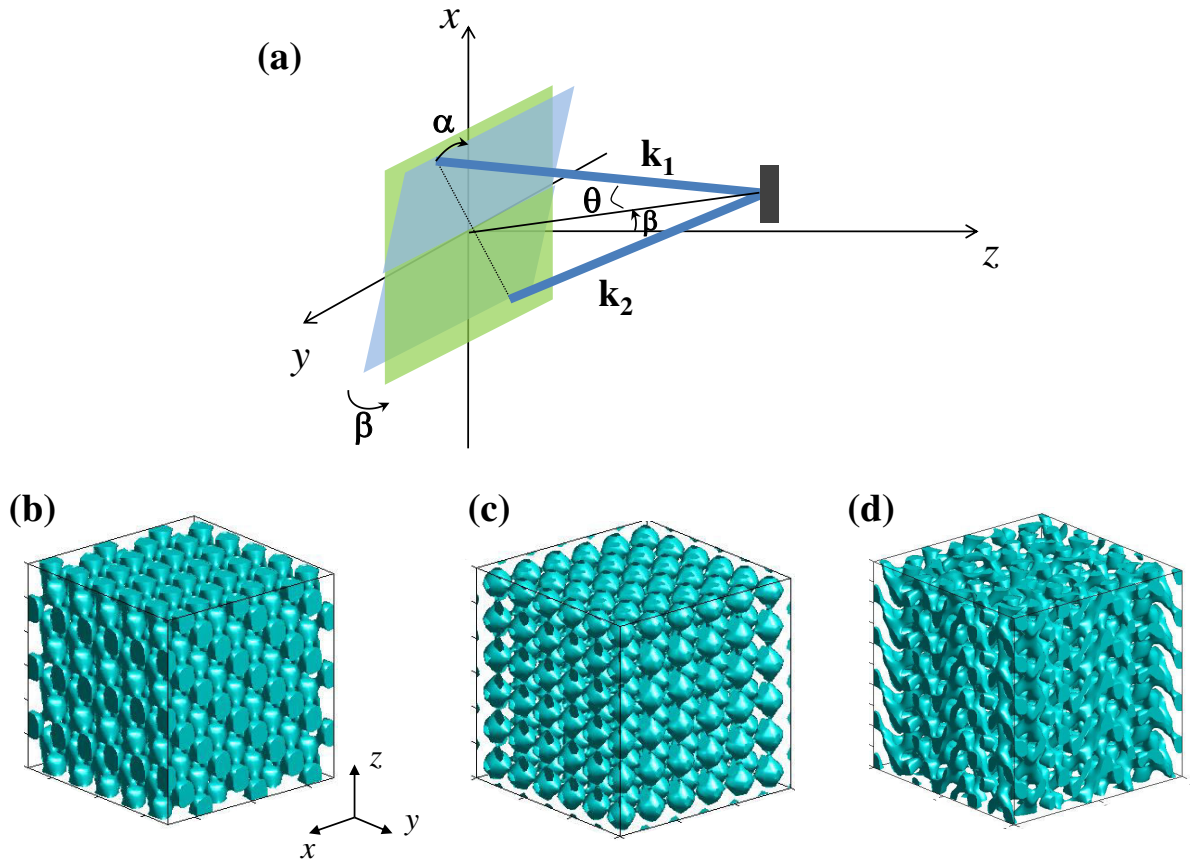


Figure 2.8: (a) Beams configuration of two-beam interference for fabrication of 3D photonic structures. Desired 3D structures are obtained by three or multiple exposures at different orientation angles α and β. (b), (c) Examples of simulation results of 3D periodic structures obtained by three exposures. (d) 3D quasi-periodic structure obtained by six exposures.

The total intensity of the two-beam interference is now written as:

$$\begin{aligned} I_{\alpha,\beta} &= I_1 + I_2 + I_{12} \\ &= 4E_0^2 \cos^2[k(x\cos\alpha + y\sin\alpha)\sin\theta\cos\beta - kz\sin\theta\sin\beta]. \end{aligned} \tag{2.31}$$

The exposure dose is accumulated by all exposures, and the total intensity is written as:

$$I_{\text{multi-exposure}} = \sum_i I_{\alpha_i,\beta_i}. \tag{2.32}$$

Many kinds of 3D structures could be created by multiple exposures with appropriate α and β angles. Figures 2.8(b) and (c) show the simulation results of 3D periodic structures. A hexagonal close-packed-like structure was created by three exposures at $(\alpha, \beta) = (0°, 30°)$, $(120°, 30°)$ and $(240°, 30°)$ and a simple cubic structure was obtained by three exposures at $(\alpha, \beta) = (0°, 0°)$, $(90°, 0°)$ and $(0°, 90°)$, respectively. 3D QPSs were also formed, for example, by six exposures at $(\alpha, \beta) = (0°, 30°)$, $(30°, 30°)$, $(120°, 30°)$, $(150°, 30°)$, $(240°, 30°)$, and $(270°, 30°)$, which is represented in Fig. 2.8(d). In particular, this technique provides similar lattice constants in transverse and longitudinal directions, which is difficult to be obtained by the commonly used multi-beam interference technique [86].

We note that the fabrication of 2D PC structures is a special case when $\beta = 0°$.

2.2.2 Experimental realization

2.2.2.1 Experimental setup

Experimentally, instead of rotating two beams, we rotated the sample with respect to two laser beams, as illustrated in Figure 2.9. Two laser beams emitted from a coherent laser source (pulsed laser, 1 ns pulse width, 150 kHz repetition rate and 355 nm wavelength), possess the same spatial profiles, the same intensities, and the S-polarization. The beam diameter is about 2 cm and the average power of each beam is 3.5 mW. These two beams interfere with each other, resulting in a modulation of the total intensity along one dimension at the sample area. The semi-angle between the two laser beams is denoted as θ, and can be easily adjusted by a couple of control mirrors. The period, Λ, of the interference pattern is determined by the θ-angle and the laser wavelength, λ, as indicated

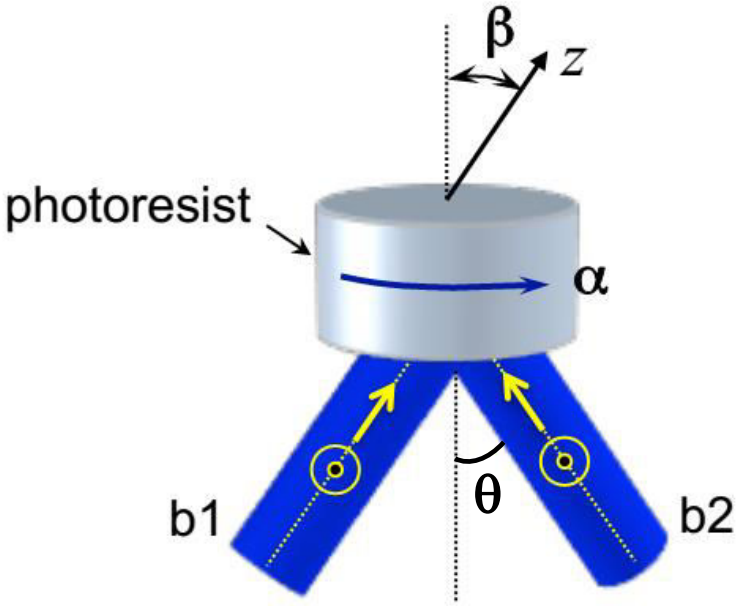


Figure 2.9: Multi-exposure of two-beam interference lithography setup. Two light beams (b_1 and b_2), which have the same polarization, interfere with each other, resulting in a one-dimensional interference pattern. The sample is placed at the interference area and on a double rotation stage. It can rotate around the x-axis and z-axis by α and β angles, respectively, for multiple exposures.

by the formula (2.24). The sample was placed on a double rotation stage: one can rotate around the z-axis by an angle α and the other can rotate around the y-axis by an angle β. This setup is very flexible in fabrication of any kind of PC structures such as: 1D, 2D, 3D periodic and quasi-periodic PCs.

2.2.2.2 Fabricated structures

The SU8 photoresist samples were prepared following the process shown in Figure 2.1, and then exposed by the interference lithography setup shown in Figure 2.9 to obtain desired PC structures. We note that after exposure, the post bake should be done immediately by increasing the temperature from 25°C to 95°C for 10 minutes to finalize the photo-polymerization process. Delaying this step can cause a lower degree of polymerization due to surface contamination and decrease the quality of fabricated structures. The fabricated samples were finally examined by an electron scanning microscope (SEM). Figure 2.10 shows some experimental results and corresponding simulation results of different fabricated structures. 1D structure (Figure 2.10(a)) was fabricated by one exposure at any α and β angle. 2D structures can be fabricated by two or multiple exposures with different α and β angles. 2D square structure (Figure 2.10(b)), for example, was fabricated by two exposures at $(\alpha, \beta) = (0°, 0°)$ and $(90°, 0°)$. 2D quasi-periodic structure was fabricated by six exposures at $(\alpha, \beta) = (0°, 0°)$, $(30°, 0°)$, $(60°, 0°)$, $(90°, 0°)$, $(120°, 0°)$, $(150°, 0°)$, as shown in Figure 2.10(c). Different 3D structures, even those can not be fabricated by commonly used multiple-beam interference, have been obtained by our method. Figure 2.10(d) shows, for example, a 3D hexagonal close-packed-like structure, created by three exposures at $(\alpha, \beta) = (0°, 30°)$, $(120°, 30°)$, $(240°, 30°)$, respectively.

We can conclude that with two-beam interference and multiple-exposure technique, any kind of PC structures can be created. On the other hand, the optical properties of these structures depend strongly on their period. For PCs operating in optical range, especially in visible range, the period should be about several hundreds nanometers. It was demonstrated that when the period of the hexagonal close-packed-like 3D structures was decreased to sub-micron scale ($\Lambda = 400$ nm) the structure possesses a PBG in visible range [103]. However, due to the low refractive index contrast of polymer material, 3D PCs possessing a complete PBG in optical and near-infrared wavelengths are still a challenge.

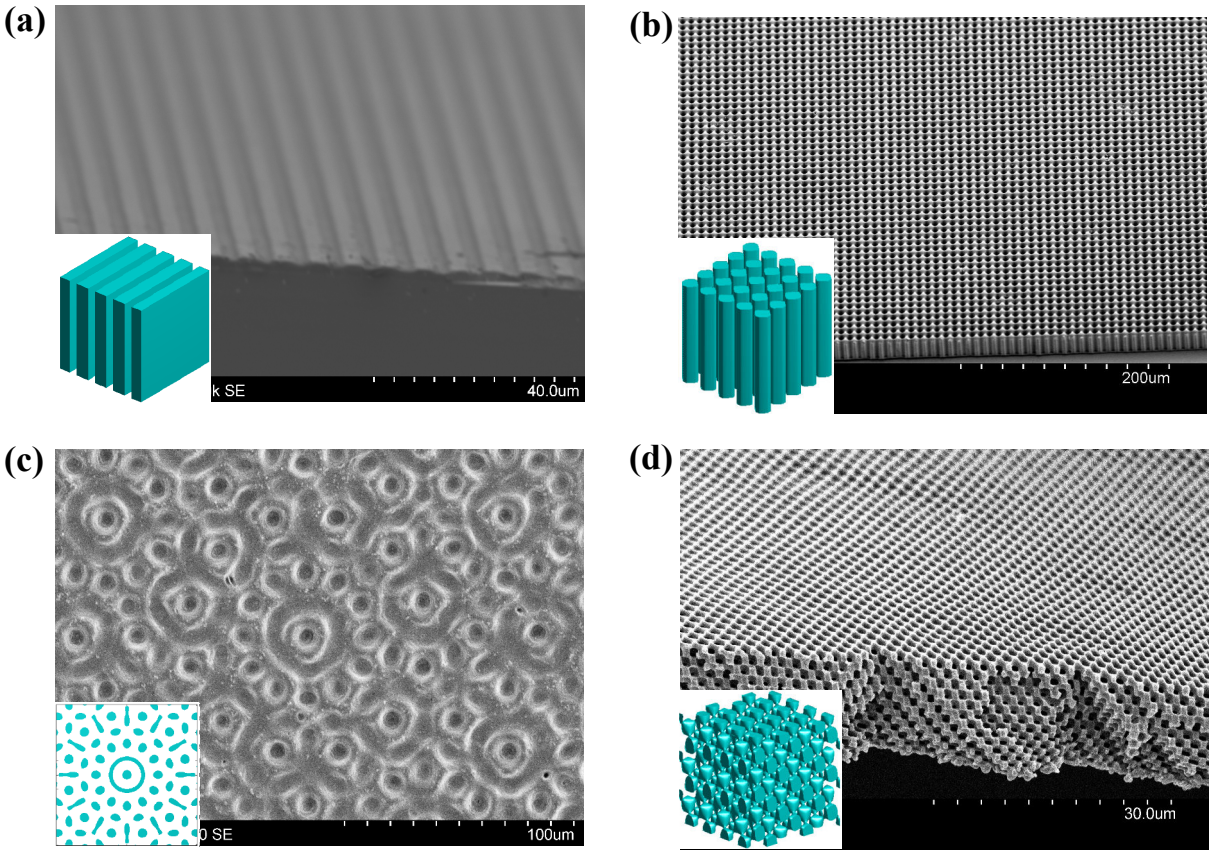


Figure 2.10: SEM images of experimental results obtained by two-beam interference. (a) 1D structure fabricated with one exposure ($\beta = 0°$ and $\alpha = 0°$). (b) 2D square structure obtained with two exposures at $\beta = 0°$ and $\alpha = 0°$, 90°. (c) 2D quasi-periodic structure obtained with six exposures at $\beta = 0°$ and $\alpha = 0°$, 30°, 60°, 90°, 120°, and 150°. (d) 3D structure obtained with three exposures at $\beta = 30°$ and $\alpha = 0°$, 120°, and 240°. Inset of each figure shows corresponding simulation result.

In general, those structures can be used as templates for the creation of structures with higher refractive index contrast. But, in other cases, they can be directly used as PCs. Moreover, PCs with artificial defects could be easily created by associating two-beam interference technique with other techniques such as direct laser writing. These structures allow to manipulate photons through stop band or partly band gap leading to abundant applications. For instance, line defects can guide or bend the light in desired direction [109, 110], point defects make nanocavities with high Q (quality) factor, which are useful for making low threshold lasers [15, 111] and so on.

The flexibility in control of the period of two-beam interference technique also leads to interesting applications in nonlinear optics. Indeed, SU8-based PCs can be used as a template, then the nonlinear material can be filled into the air-gap of structure to create nonlinear structures. PCs with longer period from a few micrometers to a few tens of micrometers are good candidate for nonlinear optics. In such case, we obtain a so-called quasi-phase matching (QPM) structures, as it will be investigated in chapter 5. In contrast, PCs with short period can be used as nonlinear PC (NLPC), which enhances the nonlinear effect by using the anormal dispersion effect mechanism. Multi-exposure two-beam interference method provides an easy way to create all these structures. Moreover, increasing the thickness of nonlinear structures is also necessary for coupling the fundamental beam into them, therefore enhances the frequency conversion efficiency. Whereas, the interference technique has a limitation to produce thick crystal due to the absorption of the resist materials. Some techniques to overcome this limitation will be presented and discussed in next chapter.

2.3 Conclusion and discussion

In this chapter, we have first studied theoretically and experimentally the use of multi-beam interference method for fabrication of polymer-based PCs. There exists many configurations of the beams but we chose three-beam and three-beam-plus-one interferences. These interferences were realized simply by sending a large beam into a multi-surface prism, which allows to compact interference system and to avoid the mechanic vibration. With three-beam interference technique, we have successfully fabricated 2D hexagonal

structures with only one exposure. By rotating the symmetrical axis of three beams around the z-axis and making multiple exposures, 2D quasi-periodic structures were also formed. By using three-beam-plus-one interference setup, it was demonstrated that 3D fcc-like PC was created with only one exposure whereas 3D quasi-periodic structures were obtained by two or more exposures. However, the period of those structures is different along different axes. In details, the period along z-axis is longer than those along x-axis and y-axis. The interference technique basing on multi-surface prisms also does not allow to control the period as well as the geometries of PCs.

To overcome these problems, we have introduced multi-exposure two-beam interference technique as a simple and efficient tool for the fabrication of any kind of PC structures. The periods of 3D structures are similar in transverse and longitudinal directions, which is difficult to be obtained by multi-surface prism technique. This method also allows to control the lattice constant from millimeters to submicrometer scale by modifying the angle between two interfering beams. This technique supplies a rapid and low cost fabrication of large and controllable structures and therefore opens various interesting applications in both linear and nonlinear optics.

Note finally that all the samples in these experiments are limited in thickness (< 10 μm) with the size of 1 cm^2. The influence of materials absorption to the uniformity of structures is not significant. All the calculations omitted the absorption coefficient. However, when increasing the film thickness, the strong absorption of SU8 material in UV range affects the fabricated structures. How to optimize the film thickness and uniformity of these microstructures remains as a challenge and will be solved in next chapter.

Chapter 3

Optimization of thickness and uniformity of 2D & 3D microstructures

In the previous chapter, we have theoretically and experimentally investigated the use of multi-beam interference technique for fabricating different kinds of PCs. Among of them, two-beam interference is better than others thanks to its simplicity in optical setup, its flexibility in changing period and geometry of PCs, etc. Nevertheless, the absorption of material remains as a drawback of this technique. In this chapter, we will study in detail this absorption effect and propose a method to optimize the quality of PC structures.

3.1 Influence of absorption effect on structures fabricated by interference technique

3.1.1 Absorption characteristics of SU8

SU8 absorbs strongly light in the UV range by the photoinitiator content added in its component. This absorption causes a non-uniform light intensity distribution across the photoresist film. Consequently, there is a gradual light intensity drop across the film thickness when an UV beam penetrates the SU8 layer from the top to the bottom. This leads to a limitation in thickness of the film. We have investigated the absorption characteristics of SU8 sample and its influence on the fabricated structures. The absorption spectra were measured by using a UV-VIS spectrometer Lambda 950. Figure 3.1(a) only shows a zoom

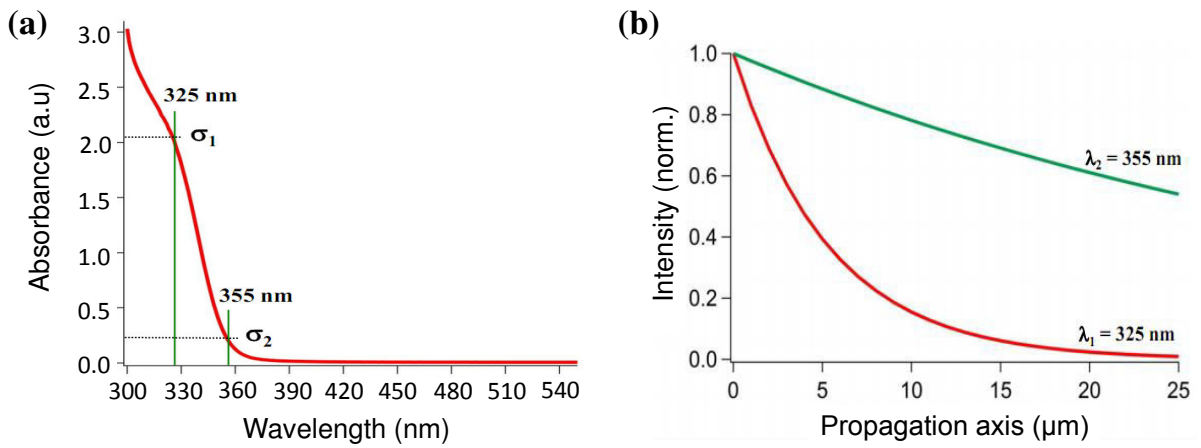


Figure 3.1: (a) Absorption spectrum of a commercial SU8 photoresist. Absorption coefficients, σ_1 and σ_2 are determined for two different wavelengths, 325 nm and 355 nm, respectively. (b) Theoretical calculation of the light intensity versus the propagation inside an absorbing material, showing the influence of absorption.

on the absorption spectrum of SU8 film with 25 μm thickness for wavelengths ranging between 300 nm and 540 nm because of the very low absorption of SU8 in visible range. The absorption coefficients have been determined for two particular wavelengths, namely 325 nm, and 355 nm, and are denoted as σ_1, and σ_2, respectively. The absorption of SU8 is very high at the UV range and decreases rather quick at visible (VIS) range. We then calculated light intensity as a function of propagation length inside the photoresist, taking into account the absorption of material. Figure 3.1(b) illustrates the variation of the light intensity for these two corresponding laser wavelengths. Obviously, the absorption is quite high at 325 nm, resulting in a rapid decrease of light intensity along the propagation. The use of a laser source at this wavelength therefore limits the fabricated structures thickness to about 3 μm corresponding the diminution of 50% of intensity. In the case of a laser emitting at 355 nm, the photoresist presents a lower absorption. Therefore, we expected that the thickness can reach 25 μm. In fact, the absorption of SU8 can be avoided using other irradiation sources, such as x-rays, or pulsed femtosecond lasers working at suitable wavelengths for two-photon excitation. However, for interference lithography using a laser source emitting nearly the absorption limit of SU8 (a 355 nm laser, for example) is suit-

able because of its simplicity and low cost. In the next experiments, we will present our investigation of the absorption effect on holographic fabrication of photonic structures, by using a pulsed 355 nm laser.

3.1.2 Theory of two-beam interference taking into account the absorption effect

To understand more about the influence of absorption effect, we rewrite the equations in the previous chapter, taking into account of the absorption effect:

$$\mathbf{E}_1(\mathbf{r},t) = \mathbf{E}_{01}e^{-\sigma\mathbf{r}}e^{i(\mathbf{k}_1\cdot\mathbf{r}-\omega t+\varphi_1)}, \tag{3.1}$$

$$\mathbf{E}_2(\mathbf{r},t) = \mathbf{E}_{02}e^{-\sigma\mathbf{r}}e^{i(\mathbf{k}_2\cdot\mathbf{r}-\omega t+\varphi_2)}, \tag{3.2}$$

where σ is the absorption coefficient of the photoresist at the excitation wavelength.

The total intensity of two-beam interference pattern in a sample oriented at angles α and β decreases over the propagation inside the material and is represented by equation:

$$\begin{aligned} I_\alpha &= \langle|\mathbf{E}_1(\mathbf{r},t)+\mathbf{E}_2(\mathbf{r},t)|^2\rangle_t \\ &= 2E_0^2\exp[-2\sigma z/\cos(\theta)]\cos^2[kz\sin\theta\sin\beta + k\cos\theta\cos\beta(x\cos\alpha + y\sin\alpha)], \end{aligned} \tag{3.3}$$

where $E_{01} = E_{02} = E_0$ are the real electric field amplitudes of excitation beams.

3.1.3 Influence of exposure dosage on the uniformity and the thickness of fabricated structures

The filling factor of PC structure depends on the exposure dose. In fact, there is a linear relationship between exposure dose and exposure time. In case of IL operation in one-photon absorption regime, the photoresist responds equally to high intensity over short exposure time and low intensity over long exposure time. It can be deduced that the intensity and exposure time play equivalently roles on the formation of photonic structures

To study the influence of dosage on the fabricated structures, we have just considered 2D square PC structures. For that, the sample is exposed twice, at (α,β)= $(0°, 0°)$ and $(90°, 0°)$, respectively. 2D interference patterns were simulated by taking into account the absorption coefficient at λ = 355 nm. We found that the effective thickness of the

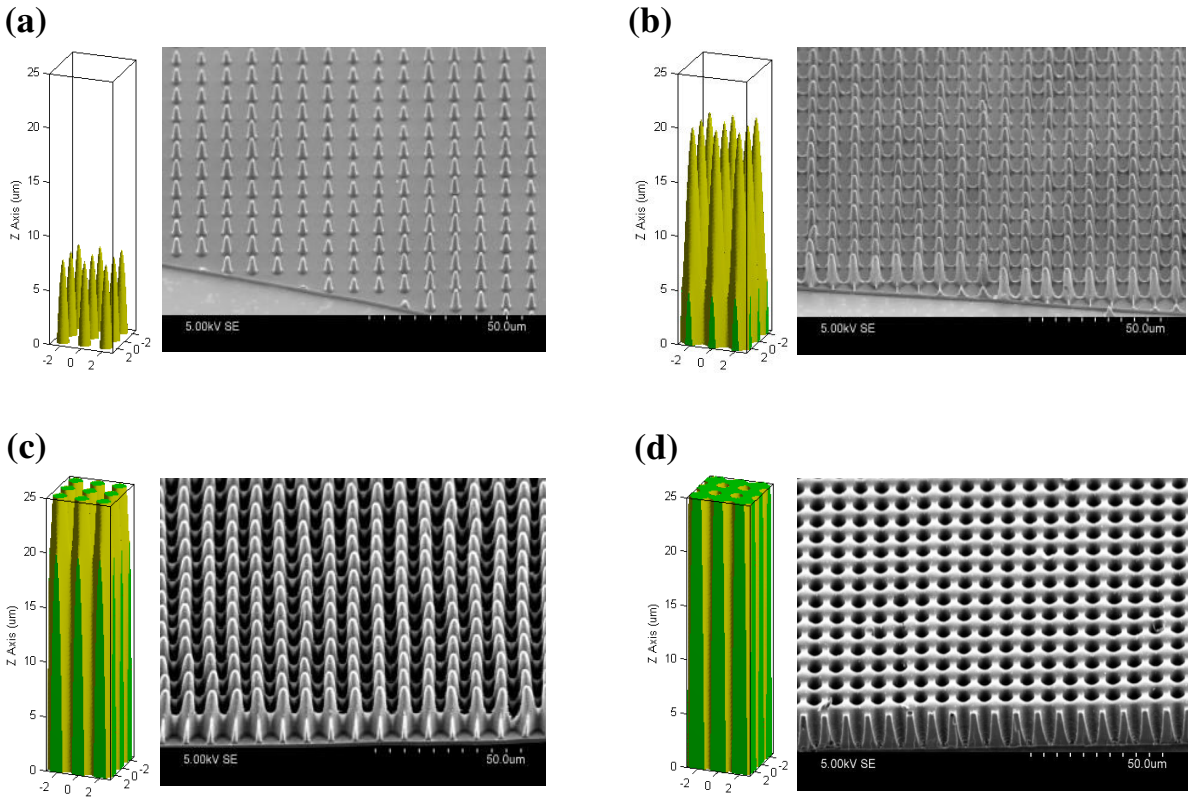


Figure 3.2: 2D photonic structures fabricated by the two-exposure two-beam interference technique with different dosages: (a) 8.25 mJ/cm^2; (b) 18.15 mJ/cm^2; (c) 23.1 mJ/cm^2; (d) 33 mJ/cm^2. The SU8 thickness is 25 μm for both theory (left, simulation) and experiment (right, SEM image). When the dosage is increased, the structure changes from cylinders (a) to air-holes (d), accordingly.

structures depends on the dose. Simulated structures for four different intensities, corresponding to four exposure doses, are shown in the left-hand side of each sub-figure of Figure 3.2. When the dose is weak, 2D conical structures with a thickness of only few micrometers are obtained (Fig. 3.2(a)). When increasing the dose, 2D air-holes structures with a thickness up to 30 μm could be obtained (Fig. 3.2(d)). This is explained by the fact that the interference intensity varies nonlinearly and differently along the transverse (x-, y-axes) and longitudinal (z-axis) directions of the interference pattern. When the dose increases, structures can be efficiently created along the z-axis, resulting in a thicker structure. However, as seen in Fig. 3.2, these 2D structures are not uniform along the z-direction, as a consequence of the absorption effect of the photoresist.

These predictions were then experimentally demonstrated as shown on the right-hand side of each sub-figure of Fig. 3.2. In our experiments, we exposed the samples from glass substrate, so the results in the bottom part of the resist being irradiated with higher dosage than that of the top part. With low dose (8.25 mJ/cm^2) 2D cones with limited thickness (Fig. 3.2(a)) were obtained. When increasing the dose, from 18.15 mJ/cm^2 (Fig. 3.2(b)) to 23.1 mJ/cm^2 (Fig. 3.2(c)), and to 33 mJ/cm^2 (Fig. 3.2(d)), 2D air-holes thicker structures were obtained. These experimental results are in excellent agreement with theoretical calculations.

We remark that this observation is valid for any laser wavelength used in optical interference lithography. Only the effective structure thickness changes according to the respective absorption coefficient. To overcome this absorption effect and to obtain uniform structures, we demonstrated a new technique to compensate the diminution of the interference pattern intensity [112].

3.2 Optimization of film thickness and uniformity

3.2.1 Working principle

From above absorption analysis, we propose to expose the sample once more by an uniform beam in the opposite direction of the previously exposed sample. The experimental setup is illustrated in Fig. 3.3(a). In fact, when the sample is exposed to the interference pattern (two beams, b1, b2), the light intensity decreases through the film thickness, from 0 μm to

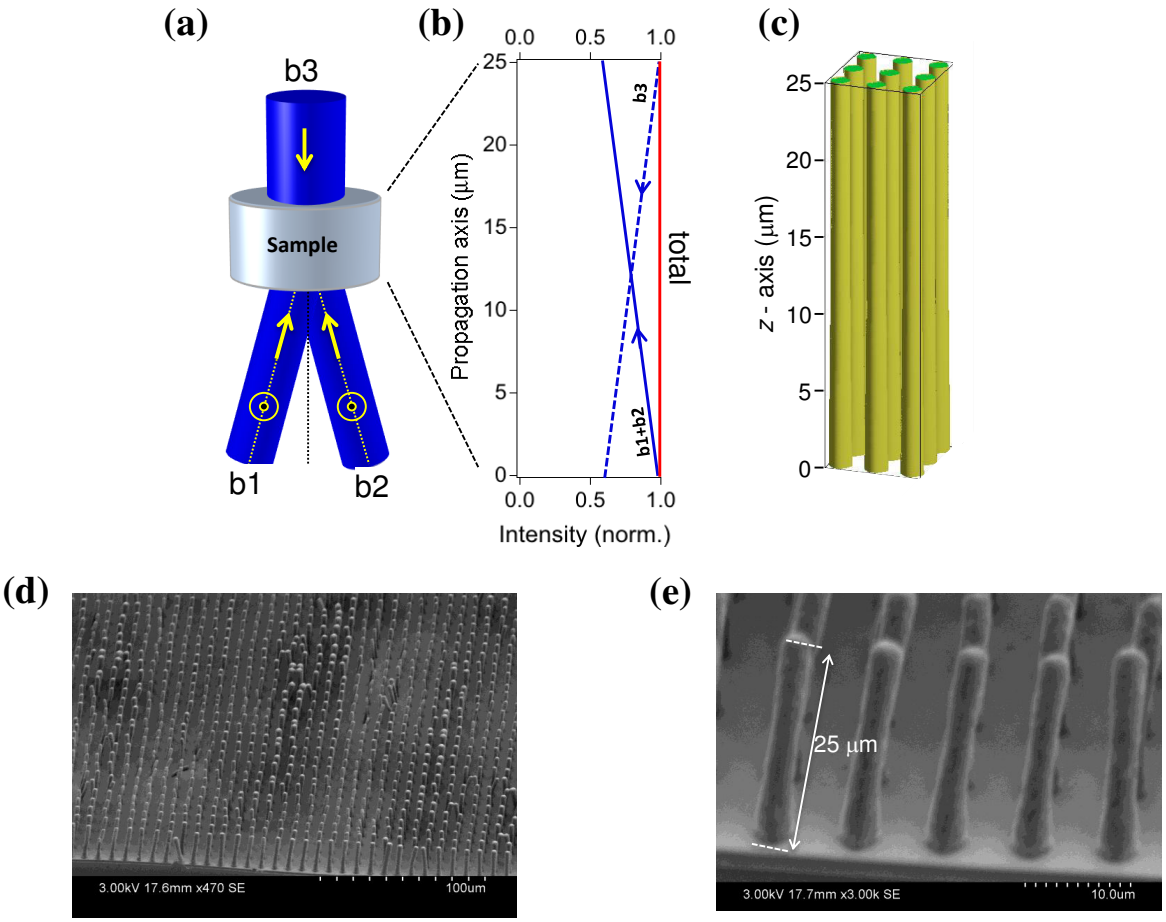


Figure 3.3: (a) Experimental setup of the two-beam interference (b1, b2) plus an additional and independent counterpropagation uniform beam (b3). (b) Theoretical calculation of the light intensity as a function of the propagation distance. The two interfering beams propagate from bottom (0 μm) to top (25 μm) while the additional beam propagates from top (25 μm) to bottom (0 μm). The red curve shows the total intensity of all laser beams. (c) Simulation of the 2D structure created by two-exposure two-beam interference with the assistance of the counterpropagation uniform beam. (d, e) SEM images of corresponding fabricated structures.

25 μm, as illustrated by the blue continuous curve (b1+b2) in Fig. 3.3(b). The sample is then exposed once more by an uniform and independent beam (b3) propagating along the opposite direction. The intensity of this laser beam decreases through the film thickness, from 25 μm to 0 μm, as illustrated by the blue discontinuous curve. The doses of these exposures compensate each other, and the total dose becomes almost the same along the film thickness as illustrated by the red curve. Note that the beam b3 is uniform, irradiates the sample independently with respect to previous exposures, and does not modify the structure already implemented by the (b1, b2) interference pattern. Indeed, in optical lithography, there exists a dose threshold above which the negative photoresist is completely polymerized and remained on substrate after developing process. The dose of the third beam (b3) is lower than the polymerization threshold and is considered as a background, which just compensates the decrease of the interference dose. The final fabricated structure is only determined by the two-beam interference technique. Figure 3.3(c) shows the simulation result of a 2D square structure obtained by this method. Considering only the case of the air-holes structure, when using the assisting beam (b3), uniform and thick structures can be obtained. For a film thickness of 25 μm, both cylinder and air-holes structures are uniform along the z-axis. For each situation, an adjustment of the dose of the assisting beam is necessary in order to obtain uniform structures. Note that the effective structure thickness changes depending on the absorption coefficient. In the case of 355 nm wavelength, the simulation results show the possibility to create uniform 2D and 3D structures with 25 μm thickness. When the film becomes thicker, the areas exposed to the interference pattern and to the assisting beam tend to be separated, and no structures can be obtained at the center of the film.

3.2.2 Experimental demonstration

Figures 3.3(d) and (e) show the experimental results obtained by the two-beam interference technique with the assistance of a counterpropagating uniform beam. To achieve uniform structure, a control of the dose for each exposure was made. Doses are 3.2 mJ/cm^2 + 3.2 mJ/cm^2 (two exposures) and 10.2 mJ/cm^2 for the 2D interference pattern and the assisting beam, respectively. Figure 3.3(e) shows a zoom on a cylinders structure elaborated within a 25 μm thickness, confirming the theoretical prediction. Figure 3.4

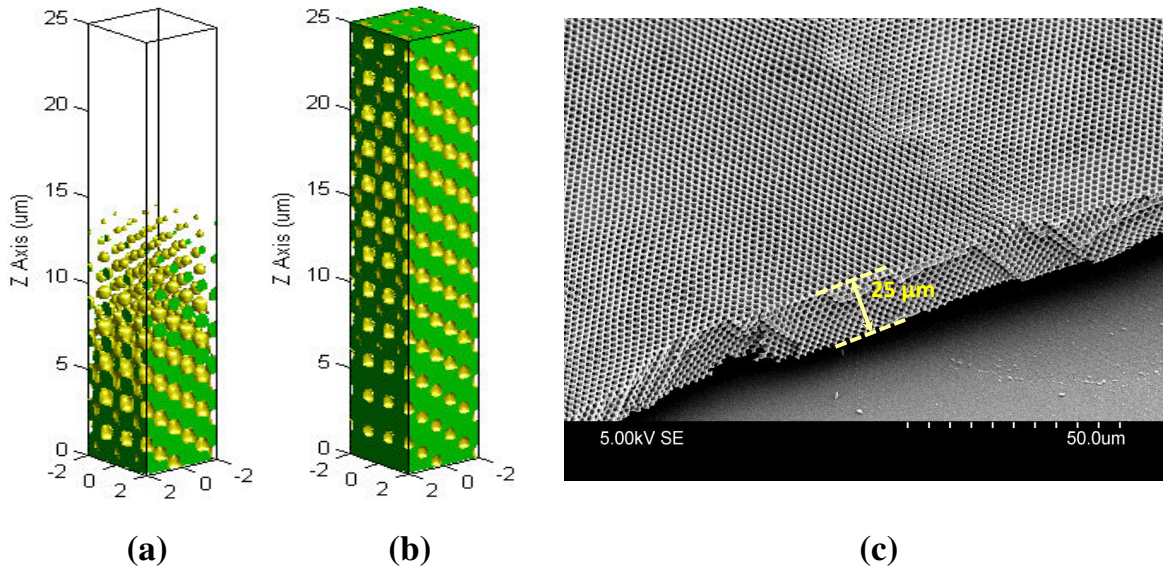


Figure 3.4: Polymer-based 3D photonic crystal fabricated by two-beam interference technique with the assistance of a counterpropagation uniform beam. (a, b) Theoretical calculations of 3D structures created by three exposures at (α, β) = (0°, 30°), (120°, 30°) and (240°, 30°), respectively. Structures are obtained without (a) and with (b) the counterpropagation uniform beam. (c) SEM image of a 3D structure fabricated according to parameters of the figure (b).

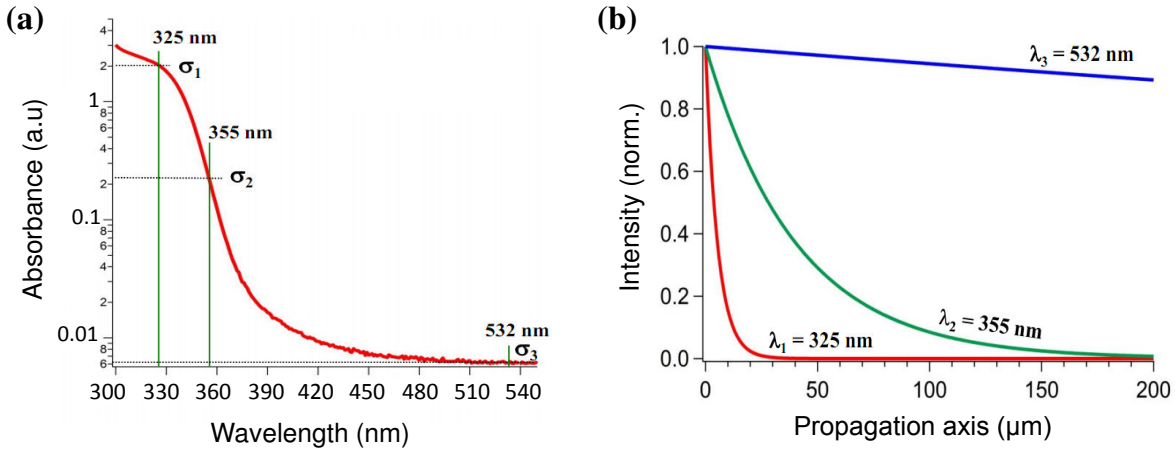


Figure 3.5: (a) Absorption spectrum of SU8 plotted in log scale showing very low absorption coefficient in visible range. (b) Light intensity versus propagation, showing a long penetration depth with a laser beam at $\lambda = 532$ nm.

shows results obtained with three exposures to the 1D interference pattern at (α, β) = (0°, 30°), (120°, 30°) and (240°, 30°), respectively, and with one exposure to the assisting beam. In this case, we obtained a face-centered cubic (fcc) structure. Similar to the case of 2D structures, with the assistance of the beam b3, this 3D fcc structure is very uniform for a thickness of 25 μm. Finally, we remark that this proposed technique can also be applied to other fabrication techniques, for example mask lithography [113] in order to make the structure more uniform along the third dimension.

3.3 Ultra-low absorption technique

The low refractive index contrast of polymeric PCs restricts applications using PBG property. Nevertheless, they are still used widely in many applications as a template to obtain structures of higher refractive index materials. Recently, the ultra-large and ultra-thick PCs open a lot of applications, which does not base on the PBG property, such as clever management of light in biochips, enhancement of nonlinear optical frequency conversion, etc. However, fabrication of these structures with high quality is not easy. Multi-exposure two-beam interference technique is a good way to achieve this purpose

thanks to the absorption property of photoresist materials.

The absorption of SU8 decreases very quickly at VIS range and seems to be zero at the wavelength of 532 nm. So, most researchers believe that SU8 commercial photoresist does not have absorption at $\lambda = 532$ nm, and to date, nobody tried to holographically fabricate structure directly from pure SU8 using this laser source. However, when the absorption spectrum of SU8 is plotted in log scale, the absorption coefficient (σ_3) is though very low but non-zero as shown in Figure 3.5(a). Hence, the intensity of excitation beam (532 nm) remains almost constant for several hundreds μm along the film thickness. The light intensity as a function of propagation length inside the photoresist film is also calculated and shown in Fig. 3.5(b). We therefore propose to use this wavelength to fabricate ultrathick photonic structures by the IL technique.

3.3.1 Sample preparation

To prepare thick film, two ways can be used. The first technique is based on a photoresist with high viscosity. The second way is the use of multiple spin coatings of thin film (only 100 to 200 μm thick film). However, multi-coating is a time-consuming process, non-uniform surface and sometimes the thickness is not sufficient. In our work, we tried two methods to overcome the restrictions in thickness and flatness surface of the spin coating technique.

Fistly, the samples are prepared by using a mould made by two glass slides, which allows to fix the shape and thickness of the resist film. Then SU8 was poured onto the mould and soft-bake in an oven at 120°C for one hour.

In the second method, we manually spread SU8-2025 in SU8 2000 series (MicoChem Corp.) onto a glass substrate and soft-bake in oven at 120°C for 2 hours. SU8 was then cooled slowly down to the room temperature at natural rate. This step evaporates all the solvent inside SU8 thick film. After that, they are separated to many small pieces. Each piece was placed onto another glass substrate and put in oven at 120°C for 10 minutes. SU8 melted and covered the glass substrate. Depending on the size of SU8 piece we can obtain the film with different thickness. Normally, the soft-bake temperature for SU8 was suggested at 65°C or 95°C [114]. For the thicker film, soft-bake temperature was realized at 120°C, which is far from the fully cross-linked film temperature (around 200°C), to

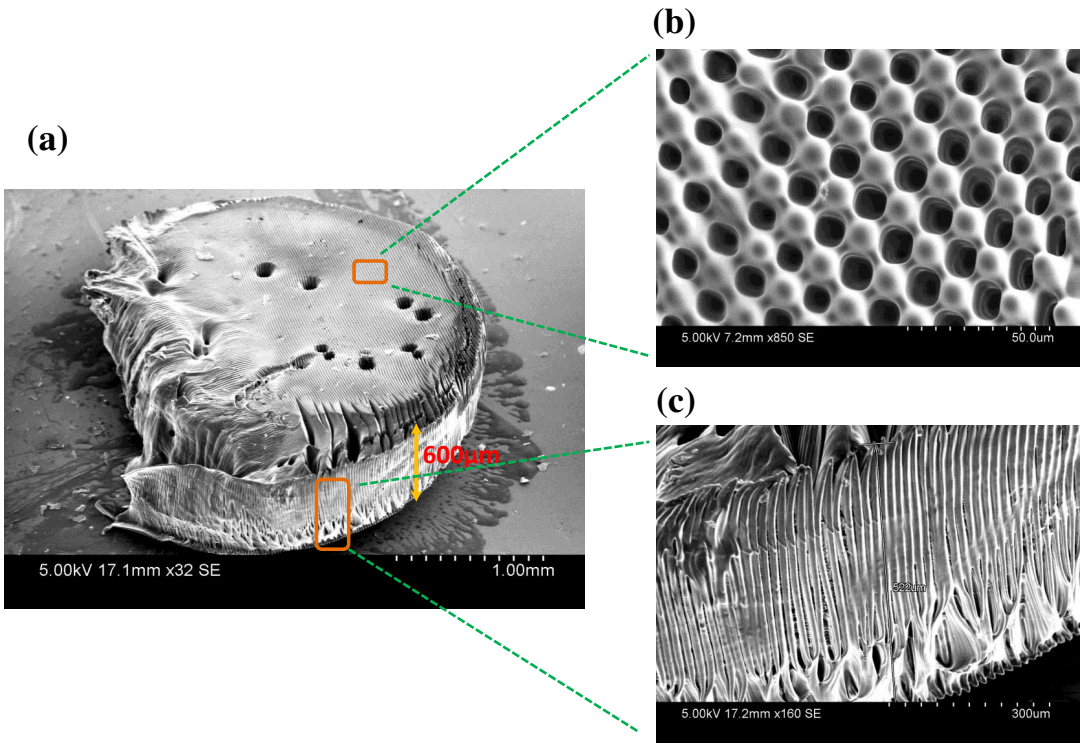


Figure 3.6: Ultra-thick PC fabricated by two-beam interference technique. Two identical beams were obtained from a CW laser at 532 nm wavelength, with an intensity of 80 mW/cm^2 for each. This square structure obtained by two-exposure at $(\alpha, \beta) = (0°, 0°)$ and $(90°, 0°)$. The thickness of structure reached approximately 600 μm and the period of fabricated structure is $\Lambda = 20$ μm.

be sure eliminating all the solvent. The samples were then stored in a black box before exposure.

3.3.2 Experimental results

The preliminary experiments were carried out with a CW laser at $\lambda = 532$ nm. Thanks to the ultra-low absorption of SU8 at this wavelength, ultra-thick 2D square structure is obtained with a thickness of 600 μm, as illustrated in Fig. 3.6. In this experiment the intensity of each laser beam is about 80 mW/cm^2 and an the sample was exposed by 10 minutes + 10 minutes. Obviously, this power is higher than UV excitation source and the exposure time is much longer. In order to restrict the influence of parameters from

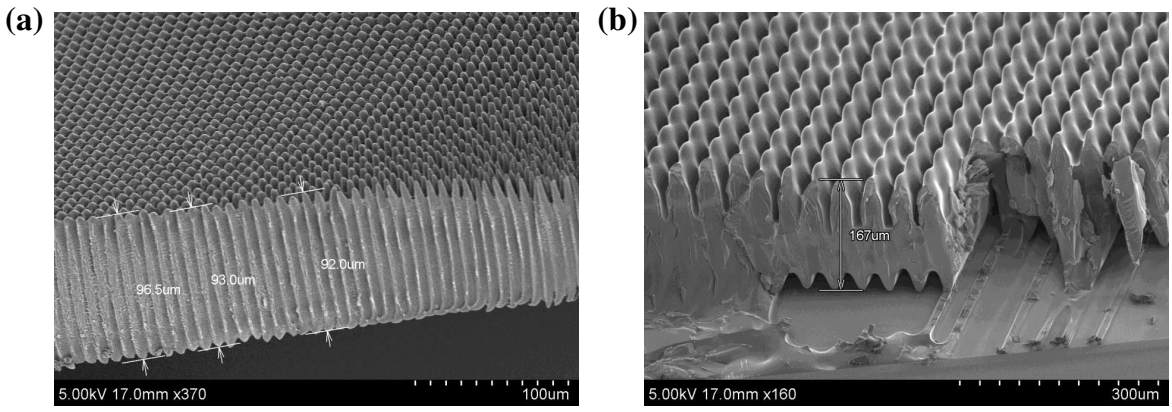


Figure 3.7: Ultra-thick PC structures fabricated by two-beam interference technique using a high power laser source at 532 nm. The interference intensity reaches 350 mW/cm^2. By two exposures at $(\alpha, \beta) = (0°, 0°)$ and $(90°, 0°)$, a 2D square structure was formed with a thickness of about 150 μm. Both structures shown in (a) and (b) present swelling effect at the middle part of structure due to the thermal absorption effect of the material.

environment such as temperature change, mechanic vibration, laser power fluctuation, etc., during the fabrication process, we have then used a high power laser source with high beam quality, good spectral purity and good stability.

A laser Verdi V5 (Coherent Corp.) with an output power around 5W was then used in order to decrease the fabrication time and to enhance the quality of fabricated structures. The optical setup of two-beam interference technique is the same as the one used previously. With this high power laser, the beam size is extended to about 10 cm^2. The power of laser beam at the sample position is about 3.5W and therefore the intensity is approximately about 350 mW/cm^2, which is 55 times higher than the one used in the last experiment. With such a laser source, uniform and ultra-thick structures are expected.

Figure 3.7 shows examples of the ultra-thick fabricated photonic structures. However, they were not uniform along film thickness as prediction. In fact, thanks to the very low absorption of SU8 at 532 nm, the laser beam can penetrate very deeply inside the film thickness and the intensity decreases non-significantly along the propagation. Consequently, the structure should be uniform and consists of perfect cylindrical pillars. However, all of the fabricated samples present swelling effect at the middle part of pillars.

The reason of this phenomenon is probably due to thermal effect of the material at high excitation power at CW regime. Indeed, when the sample was exposed to high energy laser beam and at long exposure time, the molecules were heated. The thermal energy distribution is not uniform along the film thickness. Hence, the structure is swelled in the middle part.

This effect limits the use of high power laser for rapid fabrication of ultra-thick photonic structures. We expect that there exists a compromise of laser power and exposure time so that good structure of large thickness can be obtained at moderate exposure time. This requires a long investigation and can be subject of a future work.

3.4 Conclusion

In this chapter, we have analyzed the influence of absorption effect of photoresist on fabricated structures and demonstrated different ways to overcome this effect.

The first method was employed to improve the uniformity of PCs fabricated by UV excitation source ($\lambda = 355$ nm). In this method, one uniform and independent beam is exposed in the opposite direction to two interfering beams. It does not modify the interference pattern, but just compensates the fading of the interference intensity, so that the total dose of two beams and independent beam becomes almost the same along the film thickness. Nevertheless, the absorption of SU8 at UV range is quite high. So this technique is only improve the thickness of structure from few μm to 25 μm. These structures were then used in applications of frequency conversion and will be shonw in next chapter.

The second method based on the very low absorption of SU8 in the visible range. So, it requires a high power laser and a long exposure time. For this technique, we have used a high-end laser ($\lambda = 532$ nm, $P = 5$W) to decrease the fabrication time and to fabricate very large/thick/uniform structures. The ultra-thick structures of several hundreds μm height were obtained. But the thermal absorption effect prevents the uniformity of fabricated structure along film thickness. We believe that this ultra-low absorption method should be a very good way to achieve ultra-thick photonic structures, but more investigation is required.

Chapter 4

Formation of one- and two-dimensional surface relief gratings

Surface-relief grating (SRG) is one kind of photonic structures that presents a periodical modulation on the sample surface. SRGs have a great interest due to potential applications for erasable and rewritable holographic memory, optical sensors [115, 116], guided-mode resonant filters [117, 118], beam splitters [119] and holographic beam combiners, etc. In this chapter, we demonstrate the fabrication of SRG based on passive and active polymers by using the interference technique.

4.1 SRG on passive polymer

Although passive polymer (SU8 for example) has been widely used as polymer templates for photonic crystal (PC) devices, there exists a drawback of this material: shrinkage effect. This causes a distortion of PCs fabricated by holographic lithography [120] leading to a shift of the photonic stop band toward shorter wavelengths [121]. In some cases, volume shrinkage can reach 40% free volume of the polymer network [122]. In some situations, this problem, however, gives a possibility for fabrication of SRG structures, which only need a modulation on the sample surface.

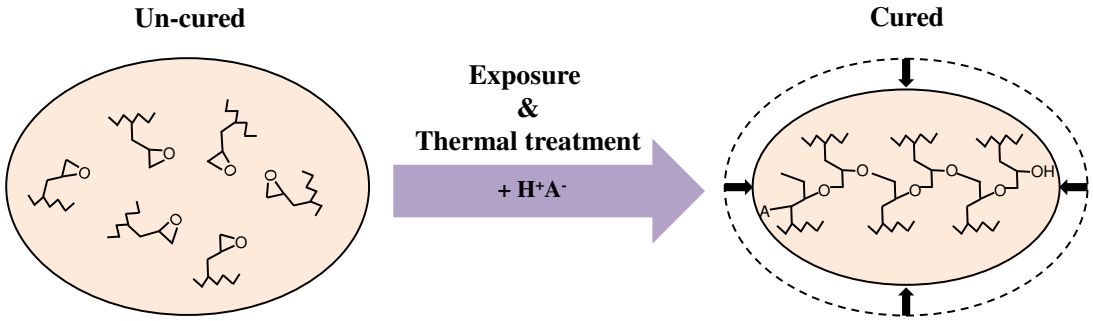


Figure 4.1: Shrinkage effect of SU8 photoresist. The uncured monomers cross-link together to form polymer chains, thanks to a photo-activation or thermal annealing. This process causes a decrease of cured volume with respect to that of uncured monomers volume as illustrated by arrows.

4.1.1 Shrinkage effect

Shrinkage effect, as illustrated in Fig. 4.1, is a volume contraction of material when the SU8 monomers polymerize and cross-link into a polymer network by a light exposure or a thermal treatment. The post-exposure bake (PEB) step, which follows light expose in holographic lithography process, finalizes the cross-link process and the shrinkage occurs when the polymer is cooled down to ambient temperature. The percentage of shrinkage of each type of polymer is different and depends on the exposure dosage, PEB time and PEB temperature. The shrinkage effect can be different depending on the contact of polymer film with the substrate. The shrinkage is isotropic if the film is separated from the substrate. Herein, the shrinkage is an average of perpendicular and parallel shrinkages. Whereas, the shrinkage is anisotropic if the film is in contact with the substrate, so there is a difference between the perpendicular and parallel shrinkages. In our experiments, the shrinkage is anisotropic because the polymer film is deposited on the substrate, and the top surface and the perpendicular direction of the film are free. This shrinkage effect is a well-known problem in microstructures by negative-tone resists. This is, of course, a non-desired effect in fabrication of micro- and nano-structures. Figure 4.2 shows an example of structure that is distorted by anisotropic shrinkage. That structure was fabricated by the direct laser writing technique employing the idea of low one-photon absorption proposed

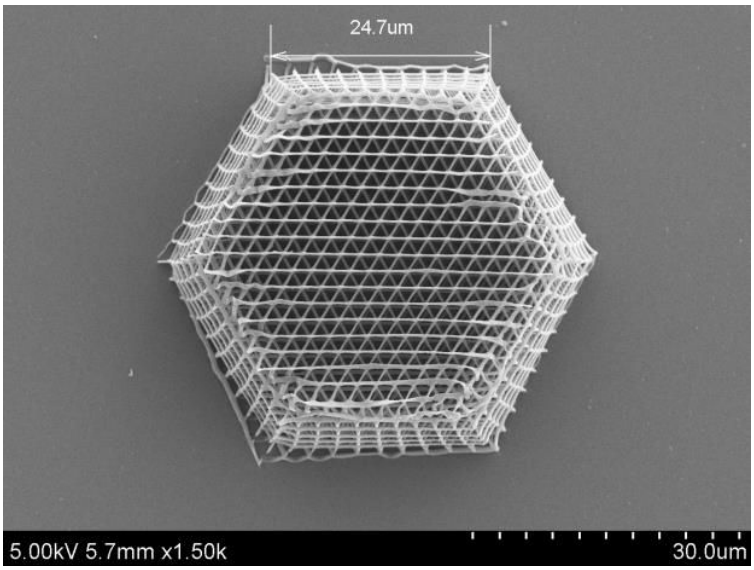


Figure 4.2: The distortion of a 3D photonic structure due to the shrinkage effect of SU8. The bottom of structure is retained by the contact with the substrate while the top is shrank. This structure was fabricated by low one-photon absorption based direct laser writing technique [123].

in previous chapter. Nevertheless, the shrinkage effect sometimes becomes useful. For example, it allows to scale down the stop band of a woodpile PC, from 1.6 μm to 1.3 μm [121], or to the formation of SRG structure [108], etc.

In this section, we will investigate the shrinkage effect of SU8 photoresist by using an interference technique and show how to use it to fabricate SRG structures.

4.1.2 Fabrication process

Two-beam interference technique is used for formation of SRG. First, the SU8 samples were prepared by spin-coating method onto a clean glass substrate. The thickness of the film depends on the type of SU8-2000 series, which possesses different viscosities, and spin-coating parameters such as speed, acceleration and spin time. The resist films were then soft-baked to remove the solvent.

Then, the SU8 films were exposed by two-beam interference setup as presented in previous chapter. Figure 4.3 shows the whole fabrication process of SRG based on the shrinkage effect of SU8 resist. Two coherent laser beams are obtained from a pulsed

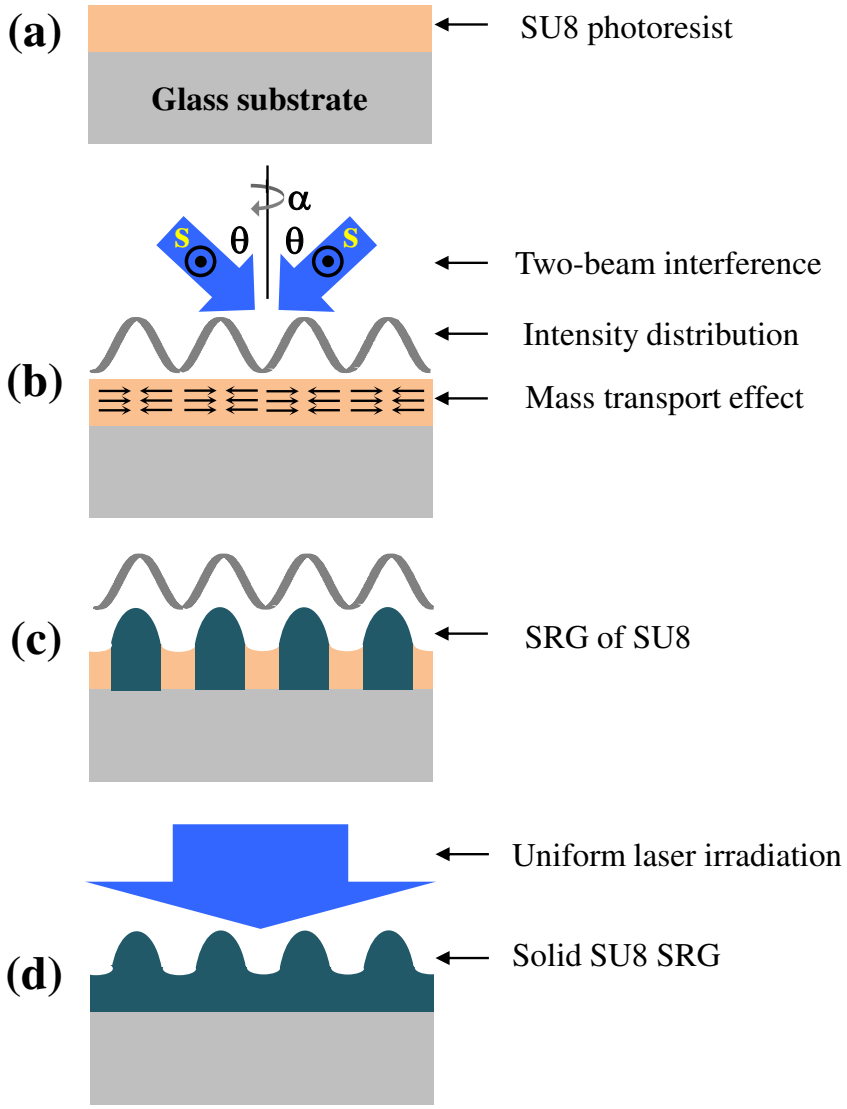


Figure 4.3: Fabrication process of a passive SRG. (a) SU8 photoresist is spread onto a clean substrate by spin coating method. (b) Illumination of the sample by two-beam interference pattern. S indicates the polarization of laser beam, which is perpendicular to the incidence plane. θ and α represent the incidence angle and the rotational angle, respectively. (c) SRG is formed in phase with the intensity distribution. (d) Expose of an uniform laser to finalize the polymerization process and a full solid SRG is obtained.

laser source with $\lambda = 355$ nm, 1 ns-pulse width and 150 kHz-repetition rate. For the best intensity modulation, $S - S$ polarization of two beams are chosen and the average power of each laser beam is about 16 mW. The grating period can be controlled by the angle between two beams. The shrinkage, also called mass transport effect, happens under the intensity distribution of interference beam (Figure 4.3(b)). To finalize the polymerization process of the exposed area, the sample is heated at PEB temperature (95° C). The shrinkage effect appears in this step when the sample is cooled down from PEB temperature to room temperature, and periodical modulation of surface is formed in phase with the intensity distribution as shown in Figure 4.3(c). For fabricated PC structures, the sample is then developed by organic developer solution. The high enough dose areas remain while the lower dose areas, which are not reach the photopolymerization threshold, are dissolved. However, in the case of SRG structure, in order to fully solidify the SU8 film, an uniform laser beam (or thermal treatment) was applied to irradiate the sample as in Figure 4.3(d). Finally, the stable SRG structure was formed after PEB one more time and characterized by atomic force microscopy (AFM).

4.1.3 Experimental results

Figure 4.4(a) shows two-dimensional and three-dimensional views of 1D SRG structure with large area and a period of 8 μm. Obviously, the grating is rather uniform and the grating depth reaches around 223 nm. The peaks of grating structure correspond to the high intensity area. Besides, 2D square and 2D hexagonal SRG structures can be also obtained by rotating the samples at $(\alpha, \beta) = (0°, 90°)$, and $(0°, 60°)$ associating two exposure times. AFM and diffraction images of these structures are presented in Figs. 4.3(b) and (c). The depth of SRG structures is affected by fabrication parameters such as exposure dosage, interference pattern periodicity and thickness of the film, etc. First, the dependence of SRG depth on the exposure dose is investigated. Under the illumination of interference light beams, the induced acid diffuses from the exposed to unexposed areas, opposite to the direction of the monomers. This acid is the catalyst of cross-link process and proportional to exposure time. Increasing the exposure time will rapidly increase the acid concentration, therefore enhancing the cross-linking process during the PEB. The relief height (as well as grating depth) reaches a maximum. However, there is a

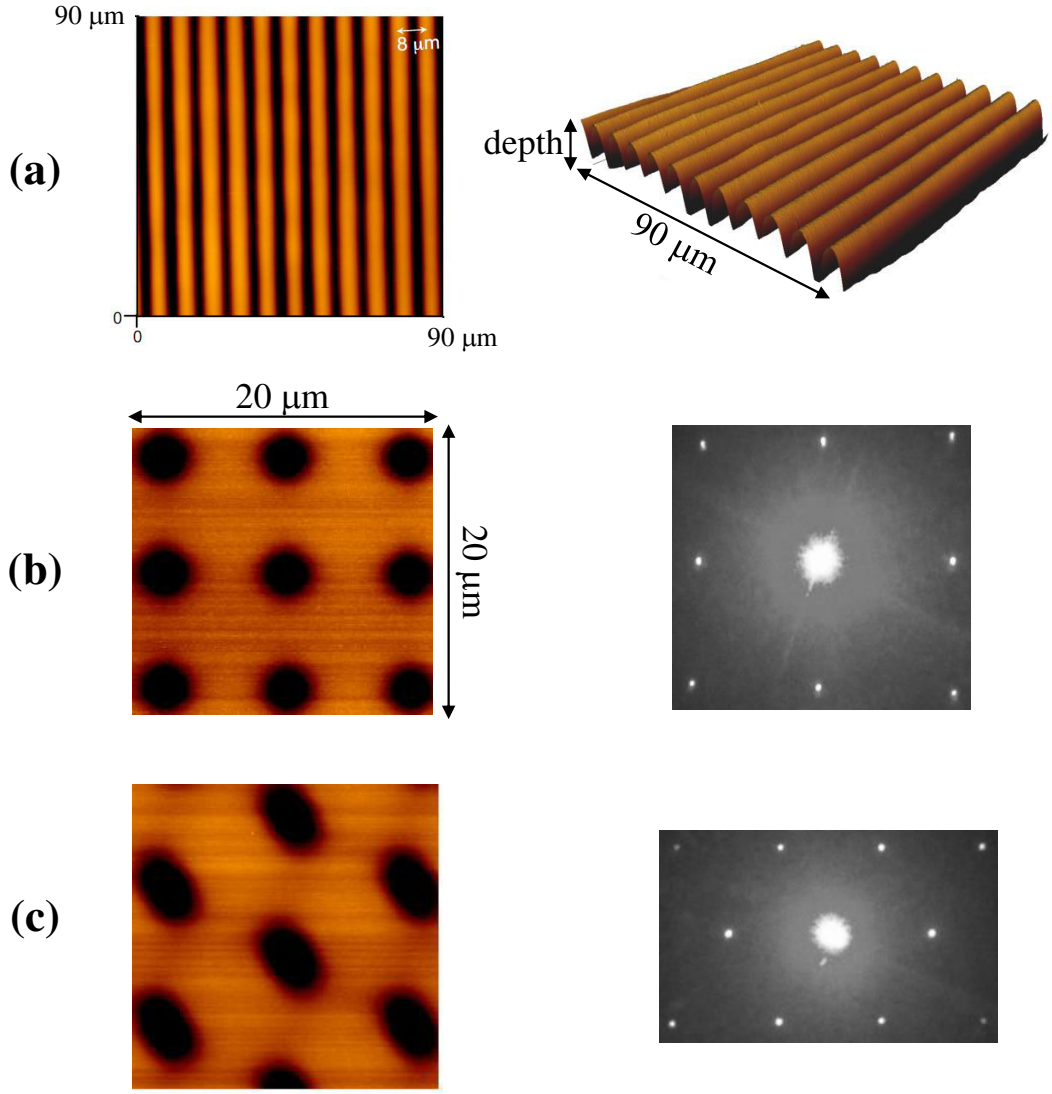


Figure 4.4: (a) AFM images of 1D SRG structure recorded in SU8 photoresist with 3D view and top view. (b) and (c) are AFM and diffraction images of 2D square and 2D hexagonal SRGs, respectively [108]. The grating depth can achieve 223 nm with a film thickness of 21 μm.

saturation value in which maximum SRG depth can be obtained. If we continue increase the exposure time, the whole sample becomes solid and the SRG depth consequently decreases. In our experiments, the best exposure time is 1,5 seconds at 32 mW of laser power.

Thereafter, the SRG depth is observed to be changed with the period. The depth first increases and then keeps almost the same value, because the SU8 monomers can not participate in movement at the large period (> 10 μm).

The dependence of SRG depth on sample thickness is also investigated. The thicker film can provide more SU8 monomers participating in the cross-linking process resulting in larger depth. In our experiments, the maximum depth achieves 223 nm at 21 μm of film thickness. So, to get the best grating depth, the film thickness, the grating period and the exposure dosage must be carefully controlled.

4.1.4 Discussions

SRG can be thus fabricated on SU8 negative photoresist without development thanks to shrinkage effect. The grating depth changes from 0 nm to 223 nm depending on the experimental parameters. Note that, SRG structure is only formed in negative photoresist. In case of the positive photoresists, the chemical structure of the resist changes when absorbing the light and the resist becomes more soluble in the developer solution.

1D and 2D SRGs based on SU8 have many applications in passive devices such as solar concentrators [124], distributed Bragg reflectors (DBR), microlens arrays [125], etc. In these devices, microlens arrays fabricated from 2D SRGs possesses abundant applications, and are widely used in commercial, for example, diffuser [126, 127], enhancing brightness of light-emitting diode (LED) [128] arrays, etc.

Nevertheless, these SRG structures on negative photoresist remain as passive structures, which can not be controlled by light source after fabrication. In the next section, we present our investigation on SRG structures by use of active polymer, such as DR1/PMMA copolymer.

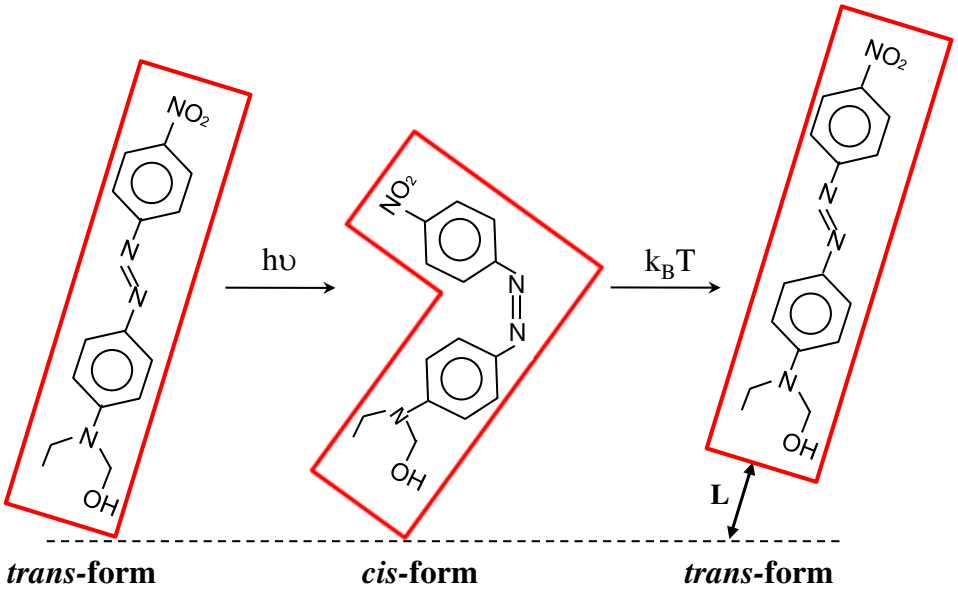


Figure 4.5: The movement of DR1-molecules throughout the photoinduced isomerization. The *trans*-form changes to *cis*-form thanks to a photo-excitation. After relaxation back to the *trans*-form, the molecules move by a distance L.

4.2 SRG on active polymer

DR1/PMMA copolymer has attracted great attention over the years for applications in optical storage, nonlinear optics, etc., thanks to the photoinduced orientation of azobenzene groups due to *trans* $\Longleftrightarrow$ *cis* isomerization. This interconversion isomers causes rotation of DR1/PMMA molecules. Moreover, when DR1/PMMA is irradiated with a light interference pattern, it could induce not only an alignment of the chromophores but also a modification of the film surface. This effect is then used to form the SRG structures in copolymer by interference technique.

4.2.1 Mass transport effect

Besides the light-induced *trans* $\Longleftrightarrow$ *cis* isomerization effect, another phenomenon was observed in DR1/PMMA azopolymer, namely a light-induced molecular displacement (or mass transport effect) when it is irradiated by a modulated light. It occurs on the polymer-free surface and leads to the formation of surface reliefs. The SRG inscription

process is described as follow: At the beginning of the process, as expected, a volume hologram is created by alternating domains of different refractive indices, produced by the photoinduced orientation of the DR1 groups. However, after few seconds, another unexpected phenomenon starts taking place: massive movement of the polymer material, creating micrometer-depth SRGs. This effect is simultaneously discovered by Rochon [52] and Kim [53] in two independent researches when the thin films were irradiated with a periodically modulated pattern from polarized laser beams at a wavelength near the absorption band of chromophore. Different from SU8 photoresist, copolymer-based SRG has a negative amplitude. This means the position of maximum peak corresponding to minimum of interference intensity distribution.

The formed SRGs are stable when the polymers are kept below T_g until to appear external stimuli. Heating the polymer films above T_g could erase the gratings and retrieving initial surface in some cases. Despite many years of research effort, the origin of mass transport effect remains unclearly. Many models have been proposed such as: pressure gradient force model [129, 130], mean-field theory model [131, 132], asymmetric diffusion model [133], etc. Each model solves a part of issue. The anisotropy of photoinduced translation diffusion model, which considers the bulk diffusion of the molecules, can explain well SRGs formation of small molecules. Figure 4.5 describes the translation diffusion of DR1-molecules throughout the photoinduced isomerization. At the stable form (*trans*-form), the chromophore absorbs the light and converts to *cis*-form. After that it thermally relaxes back into *trans*-form with a translation diffusion of a distance L. Generally, we can generate arbitrary structures, not limited in grating structure, by using the appropriate fabrication method. The modulation of SRG depends strongly on the intensity and polarization distributions of incident light. In this dissertation, we have used the two-beam interference technique in generating 1D sinusoidal modulation on the surface of DR1/PMMA film. The surface structure and grating depth can be easily controlled by changing the angle between two interfering beams and the exposure time.

4.2.2 Sample preparation and experimental setup

The samples were prepared by spin-coating method. DR1/PMMA (30/70 of molecules weight ratio) commercial powder was dissolved in TCE (trichloroethylene) solution and

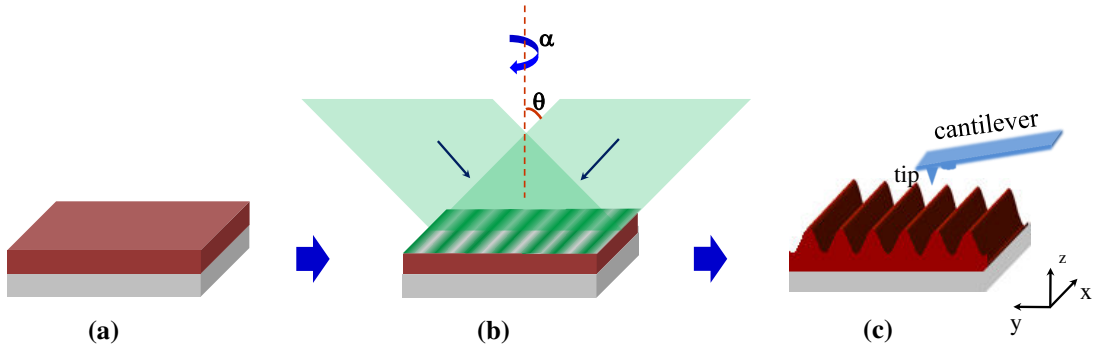


Figure 4.6: Experimental process used for formation of SRG structures. (a) The uniform DR1/PMMA film spread in a glass substrate before exposing. (b) Illumination of DR1/PMMA film by two-beam interference technique. The molecules will move from high intensity irradiation to low intensity irradiation. The SRG is formed with the same phase as the intensity distribution of the interference pattern. (c) SRG is then characterized by AFM method.

stirred for 24 hours. Then it was spread onto the glass substrate. The thickness of the films depends on spin-coating parameters and can reach 1.5 μm at 3000 rpm of spinning speed. After that, they were soft-baked in an oven for 2 hours at 120°C to eliminate the solvent.

The absorption band of DR1/PMMA copolymer is from 300 nm to 570 nm with an absorption peak at 480 nm. We, therefore used a green laser with $\lambda = 532$ nm to inscribe the 1D SRG structures by two-beam interference technique, as illustrated in Figure 4.6. The samples were then characterized by optical microscope and AFM methods. To fabricate SRG and to dynamically monitor their formation, a modified two-beam interference setup is built and illustrated in Figure 4.7. Two coherent beams are separated from one laser source, $\lambda = 532$ nm. Their polarizations are controlled by different wave plates. The original linear polarizations of two beams were changed to circular polarization, or to S-polarization and P-polarization by quater-wave-plates and half-wave-plates, respectively. The grating period can be controlled by changing the θ angle between two interfering beams. In order to monitor the dynamics of SRGs formation, a probe laser ($\lambda = 633$ nm), which is out of copolymer absorption band, is sent

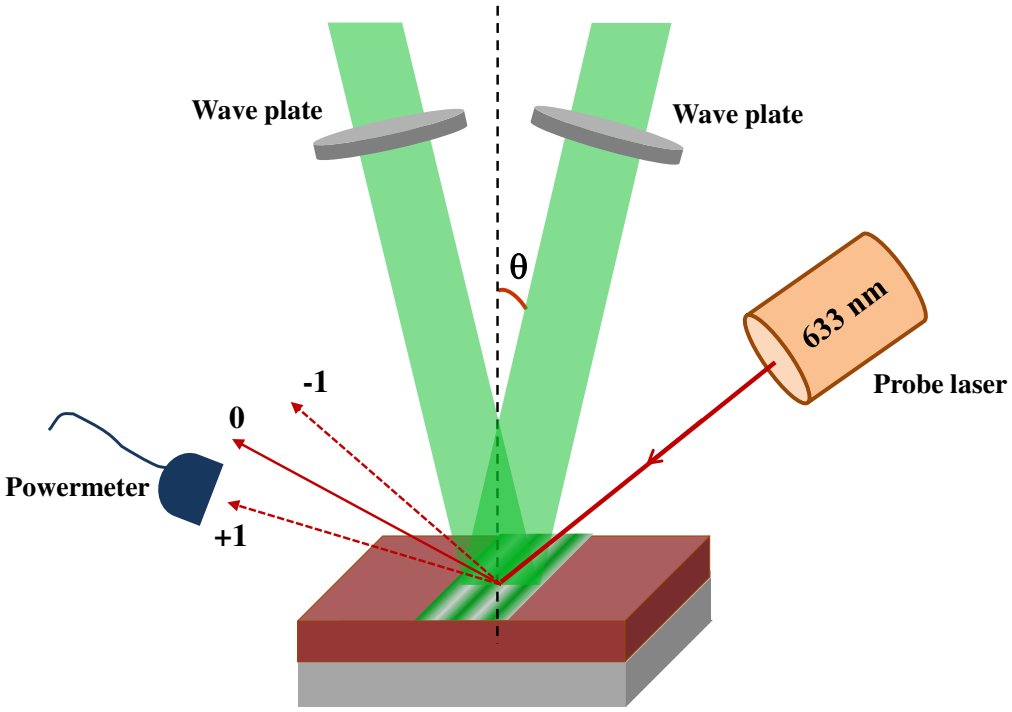


Figure 4.7: The SRGs formation by two-beam interference technique is continuous monitored during the fabrication process by a probing laser. The grating period is controlled by the angle θ. The polarization of two interfering beams are changed by two different wave plates. A powermeter is used to measure the first diffraction order from a probe laser (wavelength $\lambda = 633$ nm).

to the interference area, and the first-order diffraction spectra will be captured. This probe beam will be turned on from the beginning of SRG formation process. Its polarization is TE mode and its power is fixed at 1 mW.

In principle, different configurations of SRG such as: 1D, 2D square, 2D hexagonal can be fabricated with multi-exposure two-beam interference technique. However, we note that, due to the mass transport effect, the shape of fabricated 2D structures is not symmetric. This asymmetric problem can be corrected by employing three beams interference technique, as it will be presented later.

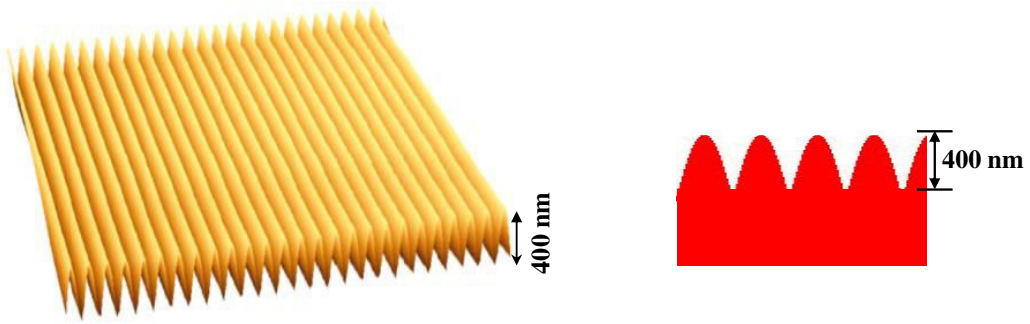


Figure 4.8: AFM image of 1D SRG fabricated by one expose of two-beam interference pattern. The grating depth achieves 400 nm.

4.2.3 Experimental results

4.2.3.1 One-dimensional SRGs

Figure 4.8 shows the AFM image of 1D SRG structure fabricated by two-beam interference method. A large area and uniform SRG was obtained with 400 nm of grating depth after exposing with 40 minutes. In contrast to the SRG on SU8 polymer, the position of maximum height of SRGs in DR1/PMMA film corresponds to the minimum intensity of the interference pattern. This indicates that the DR1 molecules move from high intensity to low intensity area by mass transport effect.

In order to obtain good quality SRGs with small period and large grating depth, the influence of fabrication parameters was then investigated. Firstly, the dependence of SRG formation on the polarization configurations of the writing beams is considered. Four polarization configurations including S-S, P-P, S-P and RC-LC (right circular and left circular) are tested while other parameters such as grating period (1.7 μm), and irradiation intensity (84 mW/cm^2) are kept constant. The results show that the circular polarization (RC-LC polarization) is the best for grating formation [108]. Whereas, the S-S polarization, which enables the best efficiency in case of SRG based SU8 photoresist, is the worst case in DR1–PMMA-based SRG. The grating depth is only few tens nanometers by using this polarization configuration.

Secondly, the depth of SRGs varies as a function of SRGs period. The experimental results indicate that the best SRGs amplitudes were obtained with structure whose period

lying between 1,5 μm and 3 μm of grating period (Λ). The optimum period is due to the movement distance of the azobenzene group under the light illumination, as shown in Figure 4.5. The movement distance of azo molecules can not match with Λ in case if the period is larger than 3 μm. While the diminution of SRGs amplitude in case of smaller period (1,5 μm) is due to the overlapping movement between highest and lowest intensities. Note that due to the mass transport process in SRG occurs slowly, the exposure time normally requires 40 or 60 minutes at 84 mW/cm^2 of beam intensity. Changing this value shows that, below the photobleaching threshold, the SRG depth increases proportionally with the rise of writing beam intensity. However, the quality of SRG becomes poor. Thus, it should be better to realize SRG at lower intensity range as well as long exposure. Note also that, the depth is only limited to about 30 % of film thickness. To optimize the diffraction efficiency and the modulation depth of the SRGs, an assisting beam, which allowed to enhance the cycle *trans* - *cis* - *trans*, is added [108].

Indeed, the $trans \Longleftrightarrow cis$ isomerization process is considered as an essential condition for the SRG formation. So, the enhancement of this process could improve the formation of SRGs. Herein, we investigated two different assisting beams. At the VIS wavelength (λ = 532 nm), the absorption of *trans*-form is higher than *cis*-form. Whereas, the absorption of *cis*-form is higher than *trans*-form at UV wavelength (λ = 355 nm). The experimental setup is shown in Figure 4.9. In the two-beam interference setup, an assisting beam, which propagated in perpendicular direction to the sample surface is added. Different polarizations of writing and assisting beams were studied to find out the best configuration for SRG formation. Besides, all experimental parameters and sample parameters were fixed, for example, the writing beam intensity at 84 mW/cm^2, the probe beam intensity (λ = 633 nm) is at 1.8 mW, the film thickness is 1.4 μm and the grating period is 2 μm.

In the case of UV beam assisted, the *cis*-form is supported to return back to the *trans*-form. Therefore, the speed of cycle $trans \Longrightarrow cis \Longrightarrow trans$ is increased. The grating depth is improved by 12 times, from ten nm to 120 nm when the writing and assisting beam have the same S-polarization. But the maximum grating depth achieves 410 nm by using a circular polarization of writing beams. The role of assisting beam, in this case, is not efficient.

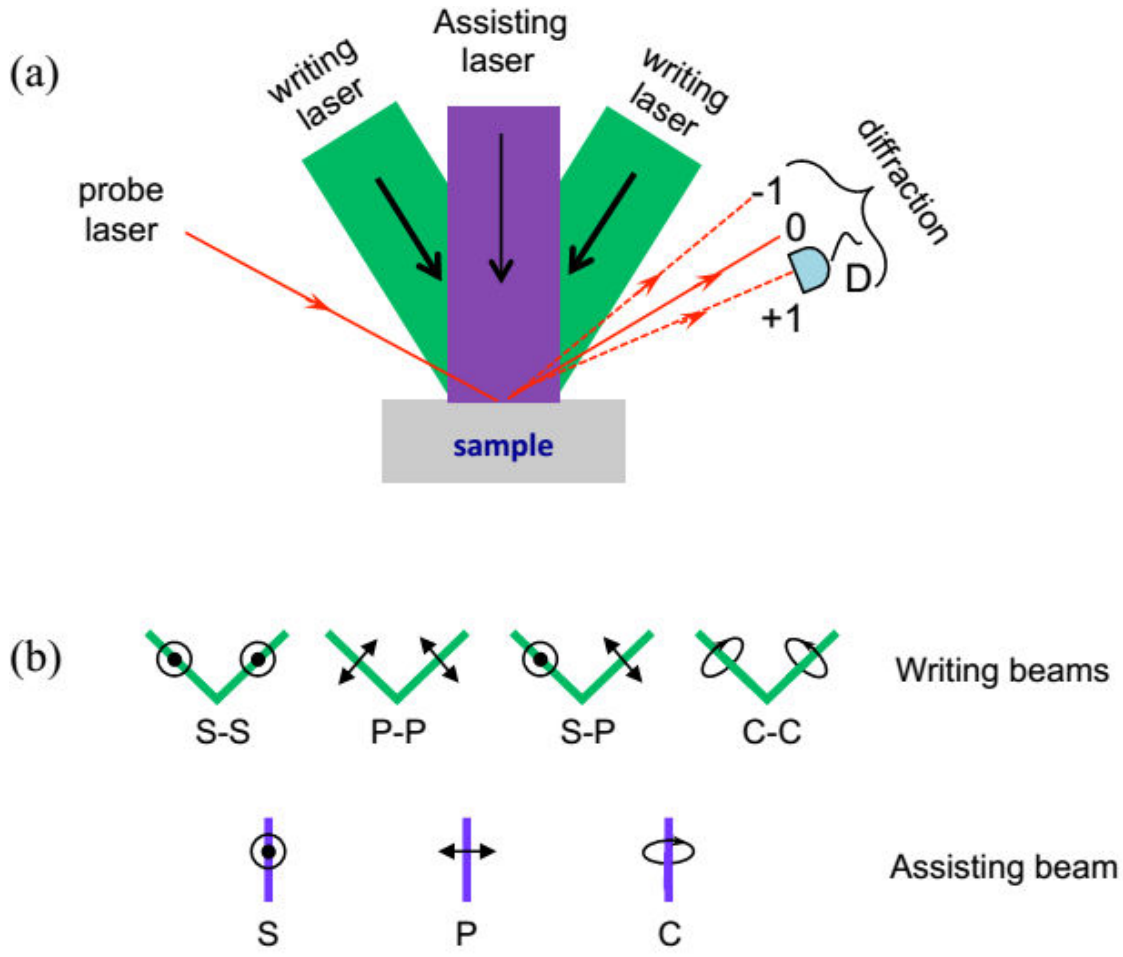


Figure 4.9: (a) Optical arrangement of two-beam interference experiment with an incoherent assisting beam. Two green (VIS) beams interfere on the surface of the DR1/PMMA and an assisting beam comes into sample at normal incidence. (b) Different possibilities of polarizations configurations of writing (VIS) and assisting beam (UV or VIS).

With VIS beam assisted, the *trans*-form transfers to the *cis*-form simultaneously with the absorption of interference pattern. The grating depth increases 8 times from ten nm to 80 nm, when writing beams possess S-polarization and assisting beam possesses P-polarization. However, the best grating depth, in this case, reaches 200 nm at P-polarization of writing beam and S-polarization of assisting beam. Although VIS assisted beam has less enhancement than UV assisted beam, it is still interesting for SRG fabrication thanks to the use of a simple and compact fabrication setup.

4.2.3.2 Two-dimensional SRGs

The mass transport effect prevents the symmetry of SRGs when applying multi-exposure two-beam interference technique [134]. To overcome this drawback, a tri-prism allowing to fabricate a 2D hexagonal SRG with one-exposure is utilized. The experimental setup is similar to the one used in chapter 2 and is presented in Figure 4.10(a). The tri-prism separates one laser beam (λ=532 nm in this case) to three coherent beams, which are then recombined on the sample surface. In this case, only circular polarization was used for all beams. Uniform and symmetric 2D hexagonal SRG is presented in Fig. 4.10(b) with a period of 1.2 μm. Figures 4.10(c) and (d) show surface modulation and diffraction image of fabricated SRG, respectively. The diffracted spots are clear and symmetric. We note that this symmetry depends strongly on the relative intensity of three interfering beams. Only a small difference of their intensities, the SRGs will be deformed.

4.2.4 Conclusions and Discussions

In this chapter, we have fabricated SRGs basing on two kinds of materials: passive SU8 photoresist and active DR1–PMMA copolymer. The mechanisms of SRG formations are different. Shrinkage effect is a key of SRGs on SU8 photoresist, in which materials move from low irradiation intensity to high intensity areas. In contrast, SRGs formation on DR1/PMMA is due to the mass transport effect, in which the polymer migrates from regions of high intensity to regions of low intensity. For each case, the dependence of grating depth on fabrication parameters such as dosage, interference periodicity, polarization, etc, was investigated in details.

SRGs based-passive polymer makes the shrinkage effect becoming useful. Both 1D and

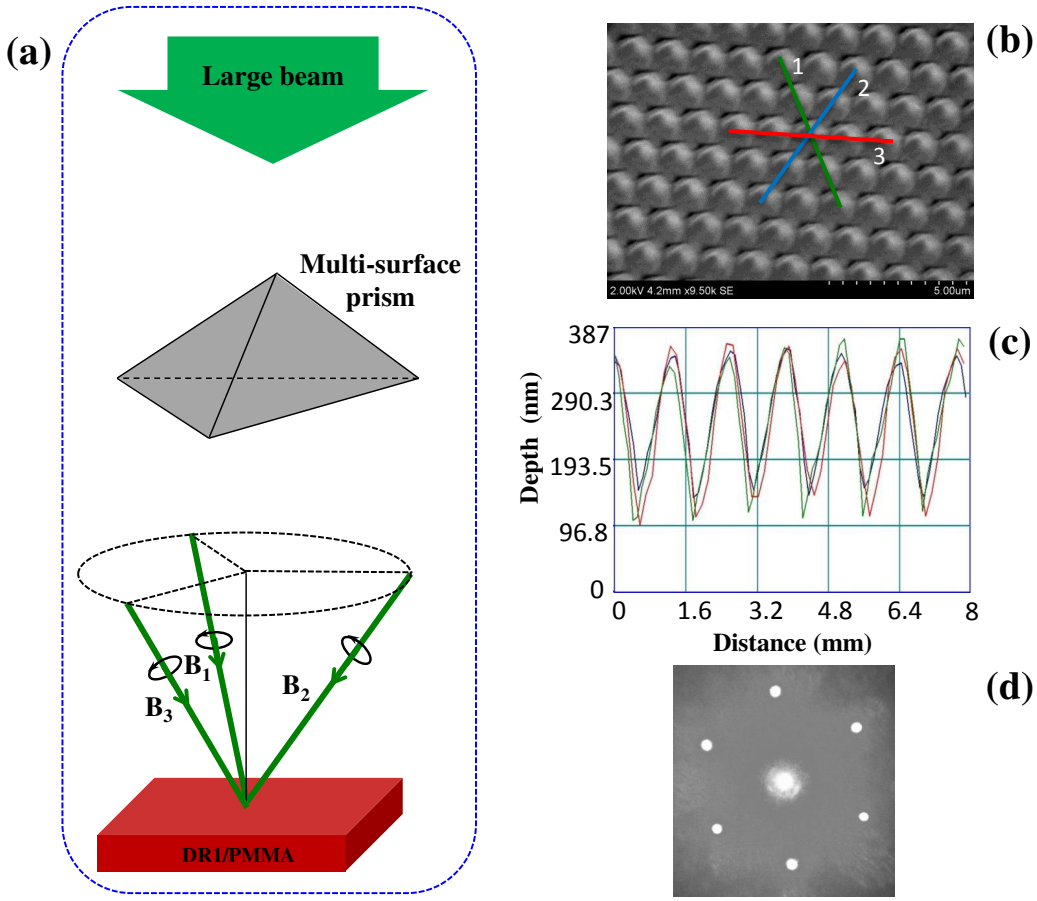


Figure 4.10: Realization of 2D periodic and symmetric SRG structure by one exposure of three-beam interference pattern. (a) A large and uniform laser beam comes into a multi-surface prism and it is devided into three sub-beams corresponding to surfaces denoted as A_1, A_2, and A_3, respectively. Three beams are overlapped at an area in which a DR1/PMMA film was placed for the fabrication. (b) SEM image of a 2D SRG structure produced by three-beam interference with circular polarizations configuration. (c) Surface modulation along three particular directions, as shown in (b), of the fabricated 2D SRG structure. (d) Experimental diffraction pattern of the fabricated 2D SRG structure.

2D SRGs are easy to be fabricated by multi-exposure two-beam interference technique without developing process. However, the best grating depth reaches only 223 nm and SU8-based SRGs are only applied for passive devices, for instant, microlens arrays, LED, etc.

Active polymer based SRGs are more interesting due to the potential application in both linear and nonlinear optics. Due to the mass transport effect, active SRGs were fabricated by one-exposure multi-beam interference technique. By controlling the polarization of laser beams, our method allowed achieving SRGs with rather good diffraction efficiency and grating depth. The best case allows a SRG with 410 nm depth. These gratings are good candidates for applications in photonic devices such as: waveguide couplers, filters, polarization discriminators, etc [135, 136]. Besides, fabrication of 3D SRGs is still a challenge, which requires further study and combination of multiple SRGs.

One of the most interesting applications of active SRGs is enhancement of the nonlinear optics signal in waveguide resonance grating structures, which will be investigated in the next chapter.

Chapter 5

Realization of quasi-phase-matching structures and application for second-harmonic generation

5.1 Introduction

After the first observation of the second-harmonic generation by Franken and co-workers [34], the nonlinear optics domain became a major theme in physics research, for both basic and applied aspects. Nonlinear optics offers a host of fascinating phenomena such as: frequency mixing processes, self-focusing, multi-photon absorption, etc. Nowadays, frequency mixing or coupling between different frequencies is a common tool to create new light. Double frequency (also called second-harmonic generation (SHG)) is one of the most important applications of frequency mixing. With this technique, one can generate a coherent radiation at frequencies shorter than that of available lasers. In SHG the input wave (or fundamental wave, ω) generates a nonlinear polarization wave, which oscillates with twice the frequency (2ω) of the input wave (or half the wavelength of the input wave). To achieve an efficient second-harmonic signal output at the end of a nonlinear crystal, it is important that these nonlinear polarization waves propagate in phase. However, SHG is a phase sensitive process and the optical dispersion of crystals gives rise to different phase-velocities between interacting light waves with different frequencies. In other words, the refraction index decreases monotonically as a function of wavelength (or increases as a

function of frequency). This makes phase matching impossible in most frequency mixing processes. Therefore the frequency conversion efficiencies are small when phase matching does not occur.

Many methods have been proposed for phase matching purpose, e.g., birefringent phase matching [137, 138], modal phase matching [139, 140], achromatic phase matching [141], and quasi-phase matching (QPM) [35, 36]. For the first twenty-five years of nonlinear optics, the employed dominant method was birefringent phase matching (BPM). Indeed, birefringent materials have different refractive indices for different polarizations. Therefore, the difference in phase velocity between interacting light waves with different frequencies due to dispersion is balanced. However, this technique has certain drawbacks. For example, it is only applied for birefringent materials whereas not all nonlinear materials display birefringence, and it is very sensitive to temperature, and presents a walk-off effect, etc. Besides, QPM technique has numerous advantages, for example, high conversion efficiency of nonlinear interactions, no walk-off, and applicable for all nonlinear materials. QPM is nowadays the method of choice for high-efficiency frequency conversion. In QPM structures, the sign of the second-order nonlinear susceptibility, $\chi^{(2)}$, is spatially modulated with an appropriate period, whereas the first order susceptibility, $\chi^{(1)}$, remains spatially constant.

Originally, the QPM structures were proposed to 1D geometry and applied mainly to waveguide devices [142–145]. These 1D QPM structures are easier to produce and are now commercially available. However, due to a single modulation period, 1D QPM can not be used for frequency conversion of multiple waves at the same time. Berger [38] suggested to extend the QPM method to 2D structure. 2D QPM structures possess more abundant reciprocal lattice vectors (RLV), allowing multiple nonlinear process in different directions. Since then, a great amount of theoretical and experimental works have been done on 2D QPM structures [40, 41, 43, 146–148].

In principle, QPM technique can be applied for all nonlinear materials. The most difficulty of QPM technique is the fabrication of such structure at micrometer scale. Depending on the nonlinear process and the employed material, an appropriate technique can be used. For ferroelectric crystals, the periodic domain inversion can be easily realized by electron-beam poling [149], electric-field poling [150] or high-voltage atomic force

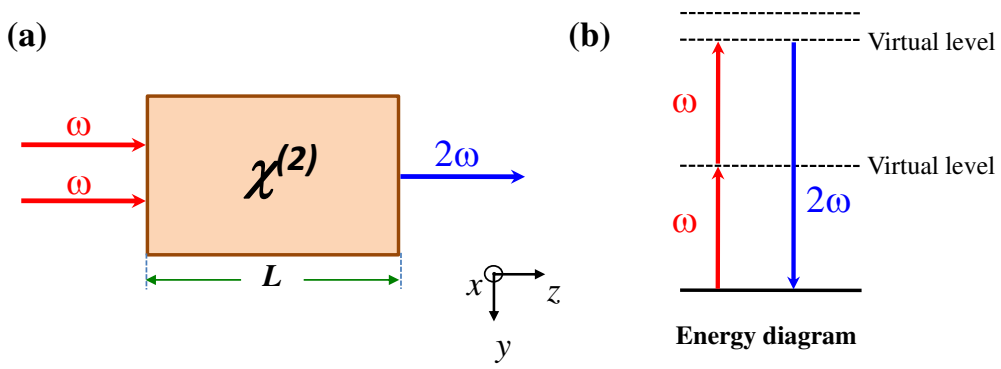


Figure 5.1: (a) Second-harmonic generation (SHG) effect. Two photons of the same frequencies, ω, are sent to a nonlinear material possessing a nonlinear susceptibility, $\chi^{(2)}$, L is the length of nonlinear crystal. The new light (double frequency 2ω, or a half of the wavelength) is generated along the propagation of fundamental wave ω. (b) Illustration of the energy levels diagram of SHG process.

microscope (AFM) [151], etc. Orientation pattern of periodically poled in semiconductor film, such as GaAs, utilizes all-epitaxial techniques [144]. Nonlinear polymer materials have received particular attention due to their large nonlinear coefficients and it is easy to process these materials into optical devices. Many techniques have been employed in recent years to obtain polymeric periodic poling structures such as photobleaching [152], direct laser writing [153, 154], two-beam interference [155], and all optical poling [156].

In this work, we demonstrate a versatile method to fabricate desired 1D and 2D QPM structures on polymer materials, and investigate their use for efficient SHG.

5.2 Theoretical analysis

5.2.1 Second-harmonic generation (SHG) effect

All materials present a nonlinear response when exposed to high enough light intensity. It is the reason that the nonlinear optical effects were discovered in 1961 soon after the invention of the laser in 1960.

Applying the electromagnetic fields, each wave has a wave vector $\mathbf{k}_j$, and oscillates at frequency ω_j (j = 1, 2, 3, ...), onto a nonlinear material, the molecular dipole moments

are induced. The total electric field inside the nonlinear crystal can be express as:

$$\mathbf{E}(\mathbf{r},t) = \sum_j \mathbf{A}_j(\mathbf{r},\omega_j)e^{-i(\omega_j t - \mathbf{k}_j\mathbf{r})} + c.c. \tag{5.1}$$

In case of sufficiently high intensity, the induced polarization, which is defined as the induced dipole moment per volume unit, consists of a linear ($\mathbf{P}_L$) part and a nonlinear ($\mathbf{P}_{NL}$) part:

$$\begin{aligned}\mathbf{P} &= \mathbf{P}_L + \mathbf{P}_{NL} \\ &= \epsilon_0\chi^{(1)}\mathbf{E} + \sum_j \mathbf{P}_j^{NL}(\mathbf{r},\omega_j),\end{aligned} \tag{5.2}$$

where $\mathbf{r}$ is the coordinate vector, ϵ_0 is the permittivity of free space, and $\chi^{(1)}$ is known as the linear susceptibility. The new electromagnetic field could be generated by the nonlinear part of the induced polarization. Starting from Maxwell's equations and by using the slowly varying amplitude approximation, the final linearized equation for the field generated by the induced polarization is governed by:

$$\frac{d\mathbf{A}_j(\mathbf{r},\omega_j)}{dr} = i\frac{\omega_j}{2\epsilon_0 c n_j}\mathbf{P}_j^{NL}(\mathbf{r},\omega_j)e^{-ik_j\mathbf{r}}, \tag{5.3}$$

where c is the velocity of light in vacuum, n_j is the refractive index of material for j-wave.

We will focus on the SHG (j = 1, 2, 3, and $\omega_1 = \omega_2 = \omega$, $\omega_3 = 2\omega$), an important phenomenon in nonlinear optics. Assuming that the plane waves propagate along the z-direction, as shown in Figure 5.1(a). The SHG process is governed by the second-order polarization:

$$\mathbf{P}^{2\omega}(z,t) = 2\epsilon_0\chi^{(2)}(2\omega,\omega,\omega)\mathbf{E}^{\omega}(z,t)\mathbf{E}^{\omega}(z,t). \tag{5.4}$$

The coupled-amplitude equations in this case are:

$$\frac{dA_1(\omega)}{dz} = \frac{dA_2(\omega)}{dz} = \frac{i\omega\chi^{(2)}}{cn_\omega}A_1^*(\omega)A_3(2\omega)e^{i\Delta kz}, \tag{5.5}$$

$$\frac{dA_3(2\omega)}{dz} = \frac{i\omega\chi^{(2)}}{cn_{2\omega}}A_1^2(\omega)e^{-i\Delta kz}, \tag{5.6}$$

where $A_1(\omega) = A_2(\omega)$ is the amplitude of the fundamental waves, $A_3(2\omega)$ is the amplitude of the second harmonic (SH) wave and n_ω and $n_{2\omega}$ are the refractive indices of the nonlinear medium at the wavelength of the fundamental and SH waves, respectively. Using the

parametric approximation, the intensity of SH wave can be calculated by:

$$\begin{aligned} I_{2\omega} &= \frac{n_{2\omega} c \epsilon_0}{2} |A_3(2\omega, z)|^2 \\ &= \Gamma^2 d_{eff}^2 I_\omega^2 z^2 \sin c^2(\frac{\Delta k z}{2}), \qquad \text{where } \Gamma = \frac{8\omega^2}{n_\omega^2 n_{2\omega} c^3 \epsilon_0} \end{aligned} \tag{5.7}$$

As we see in Eq. (5.7), the SHG efficiency depends on many parameters, for example, the nonlinear coefficient d_{eff} (or $\chi^{(2)}$), the intensity (I_ω) of fundamental wave, the length of nonlinear crystal (z), etc. The most important term that affects the nonlinear conversion is Δk, which appeared in the function "$\sin c^2(\Delta k z/2)$". Δk is called wave vector mismatch (or phase mismatch), which is caused by the dispersion of the nonlinear material and is determined by:

$$\begin{aligned} \Delta k &= k_{2\omega} - 2k_\omega \\ &= \frac{4\pi}{\lambda}(n_{2\omega} - n_\omega) = \frac{\pi}{l_c}, \end{aligned} \tag{5.8}$$

where k_ω and $k_{2\omega}$ are the wave numbers at the fundamental and the SH waves, respectively, and $l_c = \lambda/4(n_{2\omega} - n_\omega)$ is the coherence length. To maximize the SHG intensity, we must set $\Delta k = 0$ (perfect phase-matching). This phase-matching condition is only achieved when $n_{2\omega} = n_\omega$.

For any medium, there always exists the dispersion effect, so that the fundamental and SH waves travel at different phase velocities, resulting is an inequality $n_{2\omega} > n_\omega$. Therefore the perfect phase matching condition, $\Delta k = 0$, is generally impossible. As mentioned before, by using the birefringent property (BPM technique) of certain materials, the phase-matching condition can reached.

Nevertheless, not all crystals display birefringence property. For isotropic materials, we never get $n_{2\omega} = n_\omega$. Besides, the low nonlinear coefficient is also a drawback of the BPM technique. In contrast, the QPM technique allows to overcome all these problems. This technique was theoretically proposed one year after the discovery of SHG but it was not used due to difficulties in fabricating microstructures. In the late 1980s, the advent and rapid evolution of lithographically controlled patterning led to a revolution in fabrication of desire QPM structures on nonlinear materials. The QPM, therefore, has become an easier and more efficient way to enhance the efficiency of nonlinear interactions.

5.2.2 Quasi-phase matching (QPM) technique

The different phase velocities between the waves due to the dispersion of the material leads to the continuous phase slip between them. This effect is illustrated in Figure 5.2(a) and called mismatching. The blue arrows indicate the phasors corresponding to the complex amplitude contributions from different parts of the nonlinear crystal to the harmonic wave. The inverted phase after each coherence length leads to the alternation in the direction of the power flow and resulting in destructive each other. The frequency conversion efficiency is therefore very low. QPM technique, as shown in Figure 5.2(b), though does not allow to achieve a perfect phase matching but it allows to compensate the mismatching effect, resulting in an increase of SH signal along the propagation of the fundamental wave. Herein, the sign of the nonlinear susceptibility ($\chi^{(2)}$) of the material is reversed every coherence length. The modulation period of $\chi^{(2)}$ is therefore double of the coherence length ($\Lambda = 2l_c$). Nevertheless, inverting the sign of the nonlinear susceptibility requires complex technique and consuming energy. Another way, called QPM-particular can be also used, as shown in Figure 5.2(c). In this configuration, the modulation of nonlinear coefficient is $+/0/+/0/+$ instead of $+/-/+/-/+$ of traditional QPM. Figure 5.2(d) presents the SH signal as a function of nonlinear crystal length. In the perfect phase matching (blue curve), the SH signal increases quadratically as a function of the crystal length. The SH signal of QPM structure (red curve) is also fast, but, not as quickly as that of perfect case. Specially, the QPM-particular (green curve) case only reaches $1/\pi^2$ efficiency of perfect case but it is widely used due to the simplicity in fabrication.

The theory of QPM has been discussed by many groups. Based on the research reported by Fejer [35] on 1D QPM and Berger [38] on 2D QPM, the calculation for QPM structures can be expressed as follow. Applying a quasi-plane-wave on QPM structure, the SH field can be generated and represented by:

$$E_{2\omega}(\mathbf{r}, t) = \frac{1}{2} A_{2\omega}(\mathbf{r}) e^{i(2\omega t - \mathbf{k}_{2\omega}\mathbf{r})} + c.c, \tag{5.9}$$

where $\mathbf{r} \equiv z$ in the 1D QPM case and $\mathbf{r} \equiv (x, y)$ in the 2D QPM case. The couple-amplitude equation is calculated by:

$$\frac{dA_{2\omega}}{d\mathbf{r}} = -2i\frac{\omega^2}{c^2} A_\omega^2 \chi^{(2)}(\mathbf{r}) e^{i\Delta\mathbf{k}\mathbf{r}}. \tag{5.10}$$

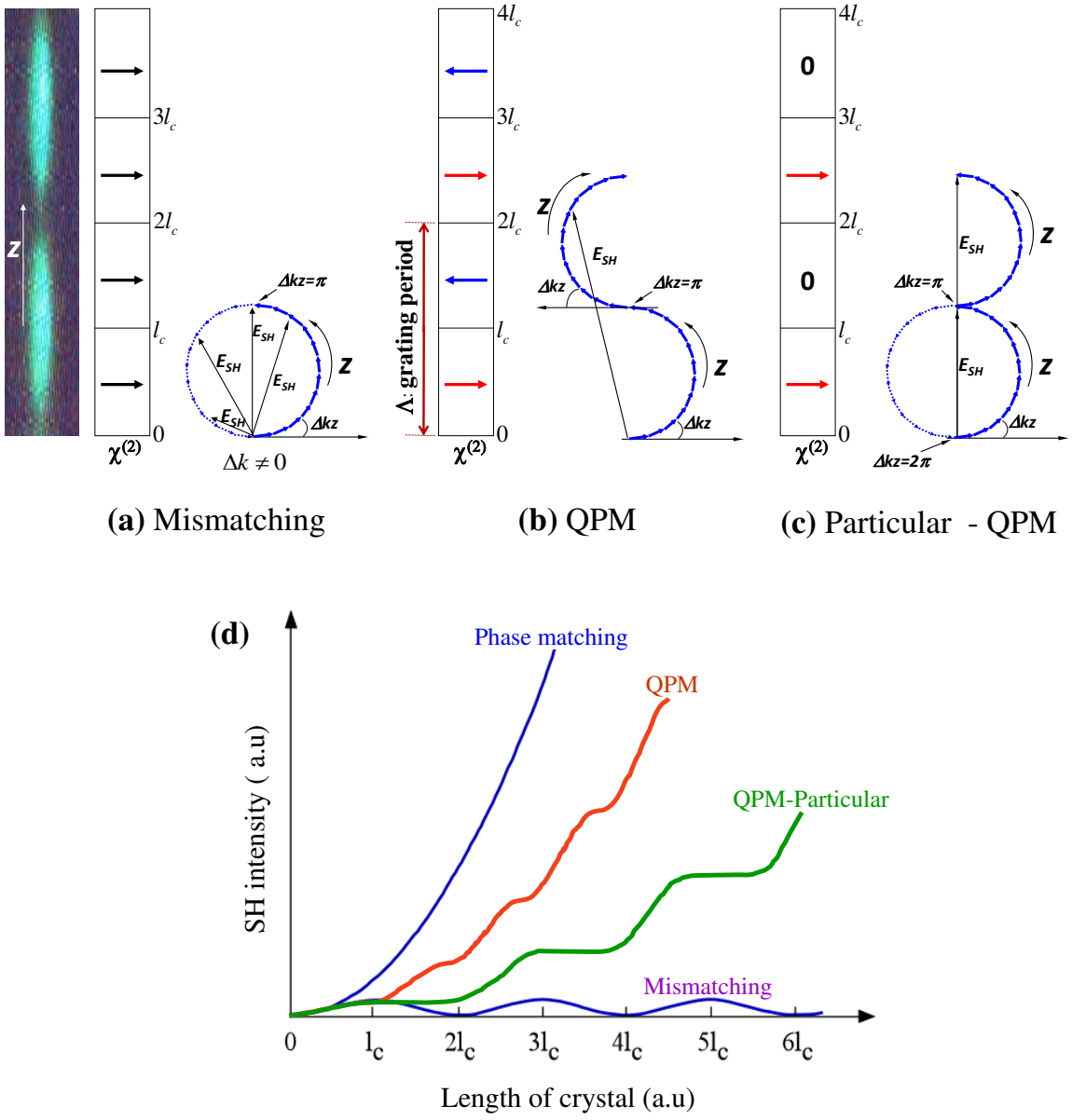


Figure 5.2: Nonlinear optical property of nonlinear materials. (a) The mismatching case, no $\chi^{(2)}$ modulation. The SHG signal is canceled after one period of $2l_c$. (b) The modulation of $\chi^{(2)}$ in QPM structure leads to a rapid growth of the SH field along the propagation. (c) Particular-QPM, the modulation of the nonlinear coefficient in between a non-zero value and null nonlinearity allows phase matching with smaller efficiency than conventional QPM case. Although, it is easier in fabrication and was applied for polymer materials. (d) The dependence of SH intensity on the length of nonlinear crystal for all cases: mismatching, perfect phase matching, QPM and particular-QPM.

For each case, 1D QPM or 2D QPM, this equation has own express.

5.2.2.1 One-dimensional QPM structures

In one-dimensional case, the QPM structure is only considered along z-axis. The nonlinear crystal is divided in different domains. Each has own sign of nonlinear coefficient, $\pm d_{\text{eff}}$ ($d_{\text{eff}} = \chi^{(2)}/2$). The coupled-amplitude equation (5.6) can be written as follow:

$$\frac{dA_{2\omega}}{dz} = \frac{i\omega}{cn_{2\omega}} A_{\omega}^2 \chi^{(2)}(z) e^{-i\Delta kz} = \Gamma d(z) e^{-i\Delta kz}, \tag{5.11}$$

where $d(z)$ is the spatially varying nonlinear coefficient. For perfect conventional phase matching: $d(z) = d_{\text{eff}}$.

Assuming that the length of the nonlinear crystal is L, the amplitude of SH wave at the end of this crystal can be calculated as:

$$A_{2\omega}(L) = \Gamma \int_0^L d(z) e^{-i\Delta kz} dz, \tag{5.12}$$

or

$$A_{2\omega}(L) = \frac{i\Gamma d_{\text{eff}}}{\Delta k} \sum_{j=1}^{N} g_j [e^{-i\Delta k z_j} - e^{-i\Delta k z_{j-1}}], \tag{5.13}$$

where N is the number of domains, g_j is the sign of $d(z_j)$ and z_j is the coordinate of the j^{th} domain. The sign changes in a perfect structure at position $z_{j,0}$ which is chosen to satify

$$e^{-i\Delta k_0 z_{j,0}} = (-1)^j, \tag{5.14}$$

where Δk_0 is the wave vector mismatch at the fundamental desired wavelength. Besides, we have:

- $z_{j,0} = mkl_c$, for the symmetry of odd-order QPM
- $z_{j,0} = [mj + (-1)^j] l_c$, for the symmetry of even-order QPM

where m is the order of QPM.

Substituting (5.14) to (5.13), we obtain the output field as:

$$A_{2\omega}(L) = \frac{i\Gamma d_{\text{eff}}}{\Delta k} 2N \tag{5.15}$$

For a perfect structure $N = L/ml_c = L\Delta k/m\pi$, Eq. (5.15) becomes

$$A_{2\omega}(L) = i\Gamma d_{\text{eff}} \frac{2}{m\pi} L \tag{5.16}$$

and the SHG intensity is calculated by

$$I_{2\omega}(L) = |A_{2\omega}(L)|^2 = \Gamma^2 d_{\text{eff}}^2 L^2 \frac{4}{m^2\pi^2}. \tag{5.17}$$

We can see that the SHG intensity in QPM structure is reduced by a factor $4/m^2\pi^2$, as compared to that of a perfect conventional phase matching. However, in practice, the QPM technique allows obtaining better conversion efficiency, because we can choose a best orientation of nonlinear crystal (highest $\chi^{(2)}$), which is difficult with BPM technique. In QPM technique, the factor is optimized at the first-order of QPM, corresponding to $m = 1$. The conversion efficiency therefore is more efficient. Moreover, it is affected by other parameters such as: duty cycle, the period error, etc. The duty cycle, $D = l/\Lambda$ is the ratio between the negative area (or positive) and the period of QPM structures. The optimum value of D is demonstrated to be 50% for the odd-order of QPM [35]. Normally, the fabricated QPM structures are not perfect. The grating period, the fundamental wavelength, the angle between the grating vector and the fundamental wave vector, and the temperature have an acceptance bandwidth in which the conversion efficiency remains high. All of them were studied in very detail by Fejer *et al.* [35].

Although conversion efficiency in QPM structures is rather good, the fabrication of $+d_{eff}$/-d_{eff} modulation seems complicated. Another technique called QPM-particular is proposed and widespread used, though its conversion efficiency is lower than QPM, due to the fabrication technique and the potential applied in polymer materials. In the particular case, which illustrated in Figure 5.3(c), the nonlinear coefficient is modulated by $+d_{eff}/0$. In this case, the output field is given by

$$A_{2\omega}(L) = \frac{i\Gamma d_{\text{eff}}}{\Delta k} N = i\Gamma d_{\text{eff}} \frac{1}{m\pi} L, \tag{5.18}$$

therefore, the SHG intensity as

$$I_{2\omega}(L) = \Gamma^2 d_{\text{eff}}^2 L^2 \frac{1}{m^2\pi^2}. \tag{5.19}$$

The SHG intensity in this case is reduced by a factor of $1/m^2\pi^2$ as compared to perfect phase matching.

Various 1D QPM structures have been achieved by modifying period or structures of nonlinear crystals and employed for different applications. For instance, dual-periodic optical superlattice structure was applied for OPA (optical parametric amplification) and OPO (optical parametric oscillator) [157], fan-out structure was applied for tunable blue laser [158], etc. Moreover, the use of quasi-periodic gratings allowed to have simultaneously multiple SHG [159–162]. Alternatively, 2D QPM provides greater flexibility and allows simultaneously realization of several frequency conversion processes.

5.2.2.2 Two-dimensional QPM structures

2D QPM structure becomes the object of huge amounts of theoretical and experimental studies over the last few years, after the first proposal of Berger in 1998 [38]. It is indicated that SHG signals can be generated simultaneously in different directions in the plane of 2D structure. The efficiency of 2D QPM processes are proportional to the corresponding 2D Fourier series coefficient, which depends on the filling factor. It is also demonstrated that multiple wavelengths generated by 2D QPM structure are more interesting than quasi-periodic 1D QPM structure.

To calculate the SHG conversion efficiency in 2D QPM structure, we assume that a linear polarization fundamental wave (ω) propagates in the transverse plane of the structure and generates a specific linear polarization SHG wave (2ω). The coupled-amplitude equation in this case is governed by:

$$\frac{dA_{2\omega}}{d\mathbf{r}} = -2i\frac{\omega^2}{c^2}A_\omega^2\chi^{(2)}(\mathbf{r})e^{i(\mathbf{k}_{2\omega}-2\mathbf{k}_\omega)\mathbf{r}}. \tag{5.20}$$

Since the nonlinear susceptibility is periodic it can be written as a Fourier series,

$$\chi^{(2)}(\mathbf{r}) = \sum_{m,n}\kappa_{m,n}\cdot e^{-i\mathbf{G}_{m,n}\cdot\mathbf{r}}, \quad m,n\in\mathbb{Z} \tag{5.21}$$

where $\kappa_{m,n}$ is the Fourier coefficient. $\mathbf{G}_{m,n}$ is the reciprocal lattice vector of the structure, which is defined by two reciprocal lattice vectors as:

$$\mathbf{G}_{m,n} = m\mathbf{b}_1 + n\mathbf{b}_2, \tag{5.22}$$

where (m,n) represents the QPM order, and $\mathbf{b}_1$ and $\mathbf{b}_2$ are the reciprocal lattice vectors.

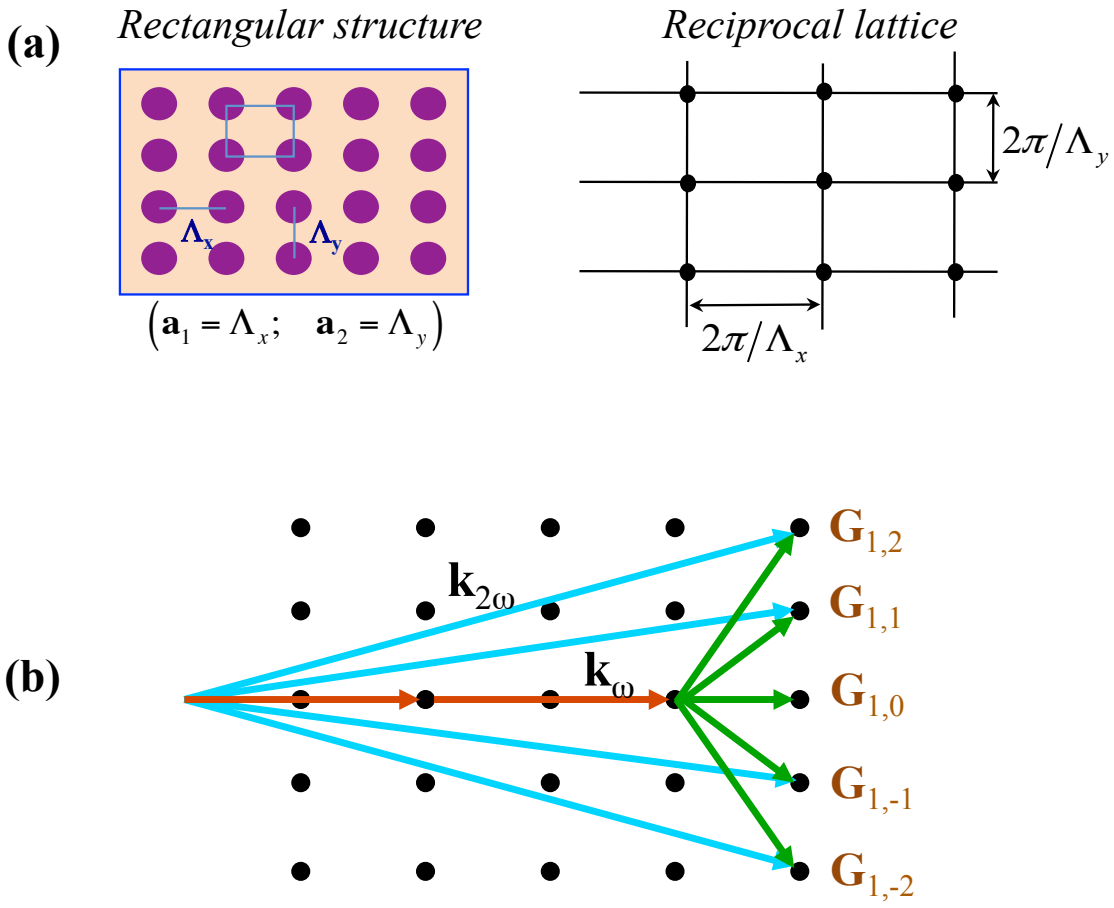


Figure 5.3: 2D rectangular QPM structure. (a) The primitive vectors of real lattice (a_1, a_2) and the reciprocal lattice vectors ($2\pi/\Lambda_x$, $2\pi/\Lambda_y$) are used to identify the Fourier coefficient ($G_{m,n}$) of the nonlinear susceptibility. The nonlinear conversion efficiency depends on this coefficient. (b) Illustration of different values of reciprocal vectors allowing multiple QPM processes.

Insert $\chi^{(2)}$ expression in Eq. (5.20), the SH field appears to be related to a sum of $\exp[i(\mathbf{k}_{2\omega} - 2\mathbf{k}_{\omega} - \mathbf{G}_{m,n})\mathbf{r}]$. The QPM condition is now

$$\mathbf{k}_{2\omega} - 2\mathbf{k}_{\omega} - \mathbf{G}_{m,n} = 0. \tag{5.23}$$

Assume that the structure is rectangular with area $a(\mathbf{r})$, length L and width W. The SH amplitude after an interaction length of L, with considering the zero of $g(\mathbf{r})$ outside the QPM structure, and the integration area $a(\mathbf{r}) = rect(x/L) \cdot rect(y/W)$, is:

$$\begin{aligned} A_{2\omega}(\Delta\mathbf{k}) &= \frac{-2i\omega^2 E_{\omega}^2 d_{ij}}{k_{2\omega} c^2 W} \iint_{a(\mathbf{r})} g(\mathbf{r}) exp^{-i\Delta\mathbf{k}\cdot\mathbf{r}} \mathrm{da} \\ &= \frac{-i\omega E_{\omega}^2 d_{ij}}{n_{2\omega} c W} G(\Delta\mathbf{k}), \end{aligned} \tag{5.24}$$

where $g(\mathbf{r})$ is a normalized and dimensionless function representing the space dependence of the nonlinear coefficient function and $G(\Delta\mathbf{k})$ is the 2D Fourier transform of $g(\mathbf{r})$.

Assume that the phase matching, $\Delta\mathbf{k}_{m,n} = \Delta\mathbf{k} - \mathbf{G}_{m,n} = 0$, can be reached at (m, n) QPM order. The SH intensity after an interaction length L is calculated by:

$$I_{2\omega}(L) = \frac{2\omega^2 d_{ij}^2 |\mathbf{G}_{m,n}|^2}{n_{2\omega} n_{\omega}^2 c^3 \epsilon_0} I_{\omega}^2 L^2. \tag{5.25}$$

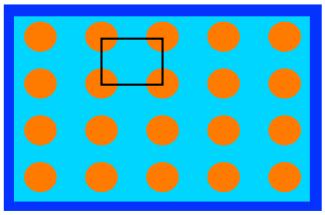
As we can see, for the 2D case, the Fourier coefficient is $\mathbf{G}_{m,n}$ whereas in 1D case, this coefficient is $\mathbf{G}_m$. The interaction efficiency is proportional to the absolute square of the Fourier coefficient and we consider this as the normalized efficiency.

Figure 5.3(a) shows the rectangular QPM structure with primitive vectors of the real lattice ($\mathbf{a}_1$, $\mathbf{a}_2$) and the reciprocal lattice vectors ($\mathbf{b}_1 = 2\pi/\mathbf{a}_1$, $\mathbf{b}_2 = 2\pi/\mathbf{a}_2$), respectively. Three vectors $\mathbf{k}_{\omega}$, $\mathbf{k}_{2\omega}$ and $\mathbf{G}_{m,n}$ may be collinear or noncollinear to others. The SHG is therefore formed in different directions for a given fundamental wavelength. Figure 5.3(b) shows the different phase-matched directions corresponding to different orders of $\mathbf{G}_{m,n}$ of the nonlinear susceptibility in the 2D rectangular lattice.

The Table 5.1 shows the Fourier coefficients for five possible 2D lattices of circular motif and rectangular motif [163]. These two motifs represent two basic cases of 2D modulation of the nonlinear coefficient. The circular motif is suitable for materials that are nearly isotropic in the (xy) plane. The rectangular motif is suitable for strongly anisotropic materials. We can see that for each type of lattice, there are some QPM orders providing significantly higher conversion efficiency than the neighbor orders. Moreover,

Fourier coefficient of a (a) circular motif and (b) rectangular motif

Lattice types	Fourier coefficients
(a) Fourier coefficient of a circular motif	
Hexagonal	$G_{mn} = \frac{2R}{a\sqrt{m^2+n^2+mn}} J_1\left(\frac{4\pi R}{a\sqrt{3}}\sqrt{m^2+n^2+mn}\right)$
Square	$G_{mn} = \frac{2R}{a\sqrt{m^2+n^2}} J_1\left(\frac{2\pi}{a} R\sqrt{m^2+n^2}\right)$
Rectangular	$G_{mn} = \frac{2R}{\sqrt{(ma_2)^2+(na_1)^2}} J_1\left[2\pi R\sqrt{\left(\frac{m}{a_1}\right)^2+\left(\frac{n}{a_2}\right)^2}\right]$
Centered-rectangular	$G_{mn} = \frac{2R\cdot 2\cos\gamma}{a\sqrt{m^2+4n^2\cos^2\gamma-4mn\cos^2\gamma}} J_1\left(\frac{2\pi R}{a\sin\gamma}\sqrt{m^2+4n^2\cos^2\gamma-4mn\cos^2\gamma}\right)$
Oblique	$G_{mn} = \frac{2R}{\sqrt{a_1a_2}\sqrt{\frac{m^2a_2}{a_1}+\frac{n^2a_1}{a_2}-2mn\cos\gamma}} J_1\left(\frac{2\pi R}{\sin\gamma\sqrt{a_1a_2}}\sqrt{\frac{m^2a_2}{a_1}+\frac{n^2a_1}{a_2}-2mn\cos\gamma}\right)$
(b) Fourier coefficient of a rectangular motif	
Hexagonal	$G_{mn} = \frac{4XY}{a^2\sqrt{3}}\operatorname{sinc}\left(m\frac{X}{a}\right)\operatorname{sinc}\left[\frac{Y}{a\sqrt{3}}(m+2n)\right]$
Square	$G_{mn} = \frac{2XY}{a^2}\operatorname{sinc}\left(m\frac{X}{a}\right)\operatorname{sinc}\left(n\frac{Y}{a}\right)$
Rectangular	$G_{mn} = \frac{2XY}{a_1a_2}\operatorname{sinc}\left(m\frac{X}{a_1}\right)\operatorname{sinc}\left(n\frac{Y}{a_2}\right)$
Centered-rectangular	$G_{mn} = \frac{4XY}{a^2\tan\gamma}\operatorname{sinc}\left(m\frac{X}{a}\right)\operatorname{sinc}\left[\frac{Y}{a\tan\gamma}(-m+2n)\right]$
Oblique	$G_{mn} = \frac{2XY}{a_1a_2\sin\gamma}\operatorname{sinc}\left(m\frac{X}{a_1}\right)\operatorname{sinc}\left[\frac{Y}{\sin\gamma}\left(\frac{-m\cos\gamma}{a_1}+\frac{n}{a_2}\right)\right]$



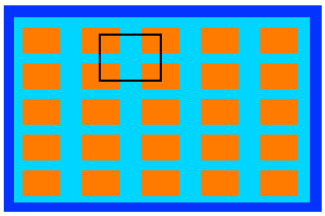


Table 5.1: Fourier coefficients of two different motifs of 2D QPM structures. (a) Fourier coefficient of a circular motif. This motif is suitable for materials that are nearly isotropic in the xy plane. (b) Fourier coefficient of a rectangular motif. This motif is suitable for strongly anisotropic materials. For each case, five different types of Bravais lattices are listed [163].

this efficiency also depends on the filling factor, lattice periodicity or the propagation angle inside the structures.

In early experiment of QPM, ferroelectric materials such as $LiNbO_3$, $LiTaO_3$, $KNbO_3$, KTP, etc., were used for enhancement of SHG signal [150, 164]. The most common method to achieve the periodically modulated structures of ferroelectric domains, which related to the polarization and the sign of nonlinear coefficient, is electrical field poling technique. In this method, mask lithography is used to create a periodic pattern on a photoresist layer, which was deposited on the sample surface. Then, a thin metal film is evaporated on the pattern surface. The high poling voltage is then applied to reverse the sign of nonlinear coefficient. This technique depends on numerous factors during the whole patterning and poling processes such as the quality of the mask, the material used for the electrode, the control of the rise and fall time of the voltage, etc. The domains sometimes are not homogeneous over the depth of crystal. Nowadays, the fabrication techniques and the materials were well developed and optimized. Besides, the nonlinear polymer materials with large nonlinear-optical susceptibility, easy to tailor for specific properties, become more interesting for QPM applications. Various techniques have been employed to fabricate periodically nonlinear coefficient structures in polymer materials such as pulse-poling procedure [165], photo-thermal poling principle [166], direct laser writing [153], and two-beam interference [155], etc. Similar to the case of 1D QPM structures, 2D polymeric QPM can be realized with a the periodical modulation between non-zero value and null nonlinearity ($+d_{eff}/0$), which is again called 2D particular-QPM. This case has lower conversion efficiency than that of the conventional QPM structure but it is simpler and easier for fabrication. Several methods are developed to fabricate 2D particular-QPM structures such as direct laser writing, photobleaching, interference, etc. In this thesis, we propose an alternative method, interference-based, to fabricate particular-QPM structure in 1D and 2D configurations. For 3D structure, in general, some theoretical explorations were carried out [44, 45], but, unfortunately, the fabrication of 3D QPM structures is extremely difficult and till now almost no successful work has been reported.

5.3 Realization and characterization of QPM structures using DR1/PMMA nonlinear material

To optimize the SHG signal by using QPM structures, we fabricated SU8-based photonic structures with a modulation of $\chi^{(1)}$ by interference technique and then filled the nonlinear material DR1/PMMA into these structures with a purpose of creating a modulation of $\chi^{(2)}$. These structures now become particular QPM structures with a periodic modulation of $\chi^{(2)}$: $\chi^{(2)}/0/\chi^{(2)}/0/\chi^{(2)}$.

5.3.1 Sample preparation

The period of 1D QPM structure was calculated as a function of fundamental wavelength and the refractive index of fundamental and SH wave [35]. It is given by

$$\Lambda_{QPM} = \frac{m\lambda_\omega}{2(n_{2\omega} - n_\omega)}, \tag{5.26}$$

where m is the QPM order, Λ_{QPM} is the $\chi^{(2)}$ grating period, and λ_ω is the fundamental wavelength.

Figure 5.4(a) shows the refractive index of SU8 and DR1/PMMA obtained by ellipsometry measurement. This is an optical technique for investigating the dielectric properties such as refractive index, thickness, composition, etc. The ellipsometric parameters Φ, the amplitude component, and Δ, the phase difference, associate with Snell's law leading to calculate the index of refraction as a function of wavelength. The refractive index of SU8 changes very little along the wavelength range from 0.6 μm to 2 μm. While the nonlinear material DR1/PMMA shows an evident dependence of refractive index on the wavelength, especially in visible and near-infrared ranges. From Eq. (5.26) we seen that the relationship between the coherence length ($l_c = \Lambda/2$) of the polymer domain with Δn, the difference refractive index at fundamental and SH waves ($\Delta n = n_{2\omega} - n_\omega$) is inversely proportional. Hence, the larger difference of refractive indices, the shorter coherence length.

Another parameter affects the conversion efficiency of QPM is duty cycle (D), which is determined by the ratio between the period (Λ) and the positive section length (l). The calculation of Fejer *et al.* shows that the optimum value for duty cycle is 50%. As well

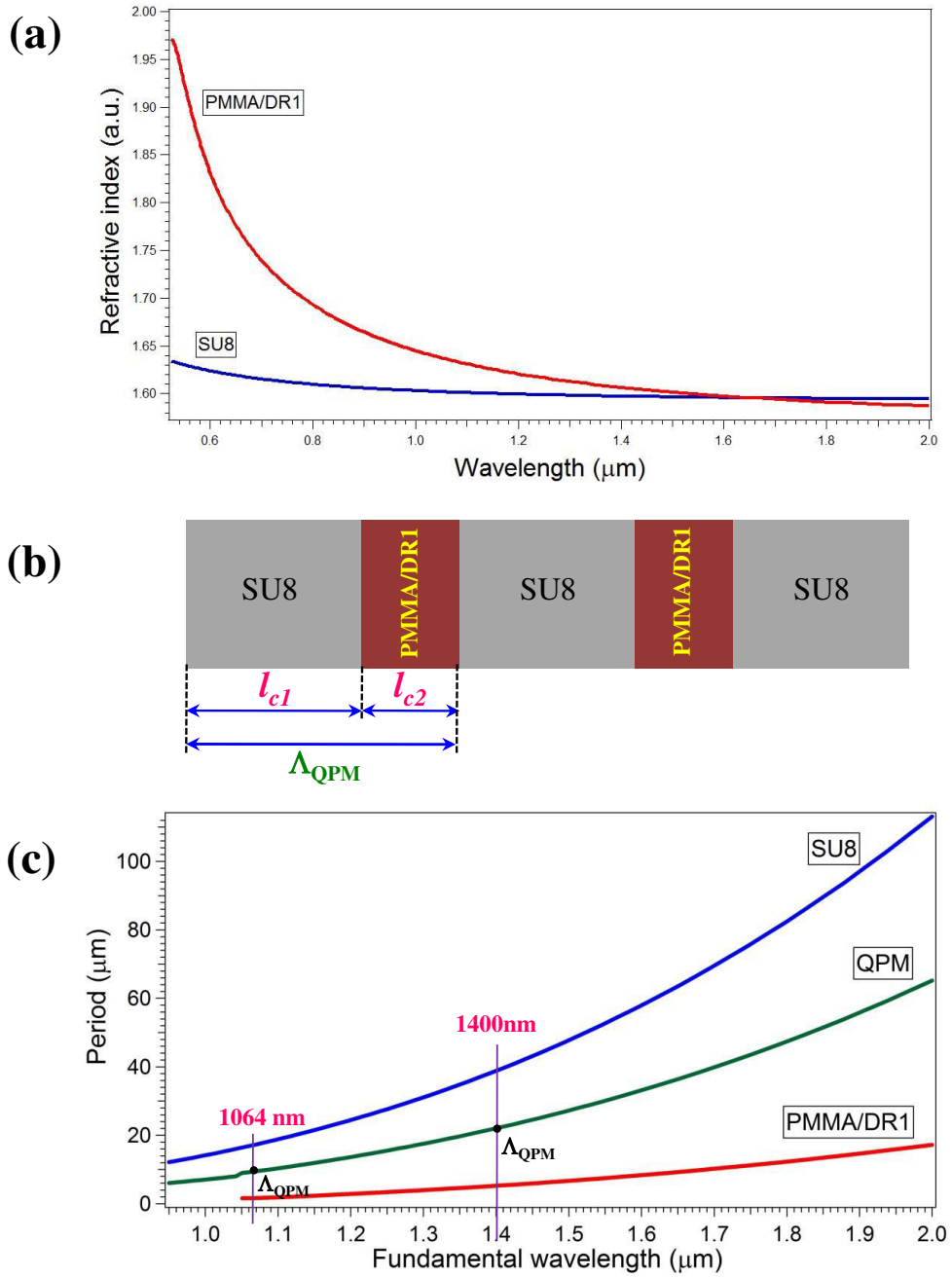


Figure 5.4: (a) Refractive indices of SU8 photoresist and of copolymer PMMA/DR1, measured by ellipsometry. (b) Illustration of 1D QPM structure, where Λ_{QPM}, l_{c1}, l_{c2} are the period, the length of SU8 and the length of DR1/PMMA domains, respectively. (c) The period of 1D QPM structure is calculated as a function of fundamental wave. If the wavelength of fundamental wave is 1064 nm, the period is 9.5 μm with 8.5 μm of SU8 domain and 1.0 μm of copolymer DR1/PMMA domain. In case of λ_ω = 1400 nm, the QPM period is 21.5 μm with 19 μm of SU8 domain and 2.5 μm of copolymer domain.

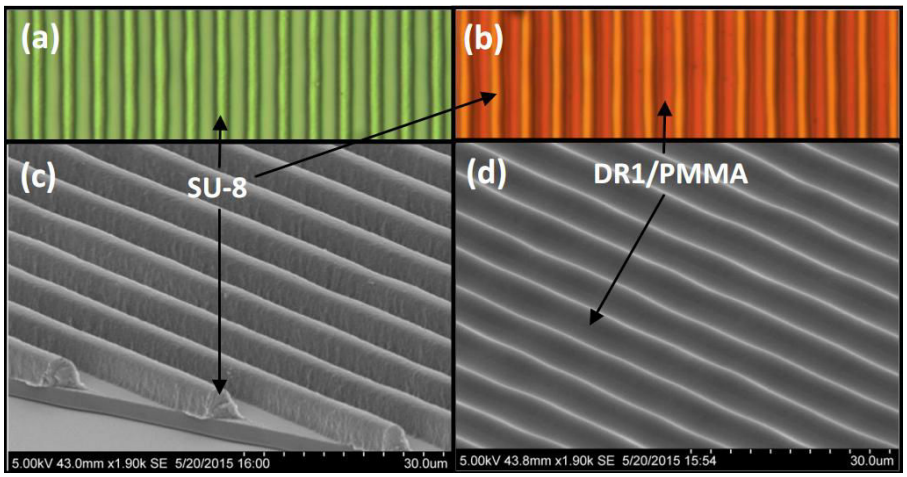


Figure 5.5: (a) and (c): Images of SU8-based 1D PC structure obtained by optical microscope and SEM, respectively. (b) and (d) are optical microscope and SEM images of same structure after filling with DR1/PMMA copolymer.

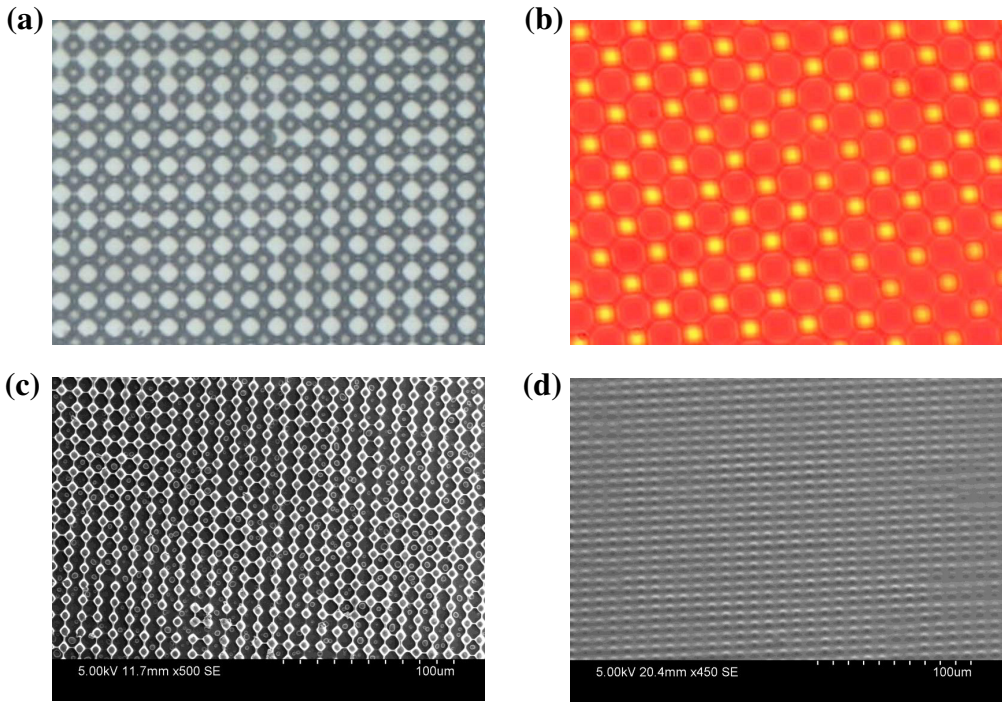


Figure 5.6: (a) and (c): Images of SU8-based 2D square PC structure obtained by optical microscope and SEM images, respectively. (b) and (d) are corresponding optical and SEM images after filling with DR1/PMMA copolymer.

as the analysis of Fejer, two consecutive domains with opposite sign of nonlinear coefficient are called a building block. The total length of the block corresponds to a period of QPM structure ($\Lambda_{QPM} = l_{c1} + l_{c2}$), as shown in Figure 5.4(b) l_{c1} ($= \Lambda_{SU8}/2$) and l_{c2} ($= \Lambda_{DR1/PMMA}/2$) are the length of SU8 domain and DR1/PMMA domain, respectively. These values are identified from the refractive indices of SU8 and DR1/PMMA at fundamental (ω) and SH (2ω) waves, and are illustrated in Figure 5.4(c). The QPM period as a function of fundamental wavelength presents very clearly the length of building block (Λ_{QPM}) and the length of SU8 and DR1/PMMA domains. For instance, to obtain SHG at wavelength 1064 nm, the QPM period should be 9.5 μm in which the length of SU8 (l_{c1}) and DR1/PMMA domains (l_{c2}) are 8.5 μm and 1.0 μm, respectively. Or for the conversion wavelength at 1400 nm, the QPM structure possesses parameters as: $\Lambda_{QPM} =$ 21.5 μm, $l_{c1} = 19$ μm, $l_{c2} = 2.5$ μm.

Based on this calculation, the 1D PC structure is fabricated on SU8 photoresist by two-beam interference technique. The fabrication process is the same as in chapter 3. In fact, the thickness of the sample is as thick as good to facilitate focusing the fundamental wave into the QPM structure. However, in our experiment, the thickness of structure is limited to 25 μm due to the absorption effect of SU8 photoresist. The exposure dosage is controlled to get proper filling factor, therefore obtaining desired l_{c1} and l_{c2} thickness. The structures were then filled by DR1/PMMA copolymer by spin-coater and annealed in an oven for 2 hours at 120°C to remove the solvent. After fabricated, the samples are verified by optical microscope and SEM (scanning electron microscope). Figures 5.5(a,c) show optical microscope and SEM images of a 1D PC structure without copolymer. The structure filled with copolymer is shown in Figs. 5.5(b,d). 2D square QPM structure was also fabricated and shown in Fig. 5.3.3. Finally, the nonlinear property was obtained by using corona poling technique.

5.3.2 Creation of $\chi^{(2)}$ by corona poling method

According to the fabrication technique, the QPM structure belongs to the particular case of QPM technique, as discussed previously. Originally, the nonlinear polymer (DR1/PMMA) is centrosymmetric due to the random orientational distribution of nonlinear chromophores. To create a strong nonlinear optical effect ($\chi^{(2)}$), these chromophores need to be aligned

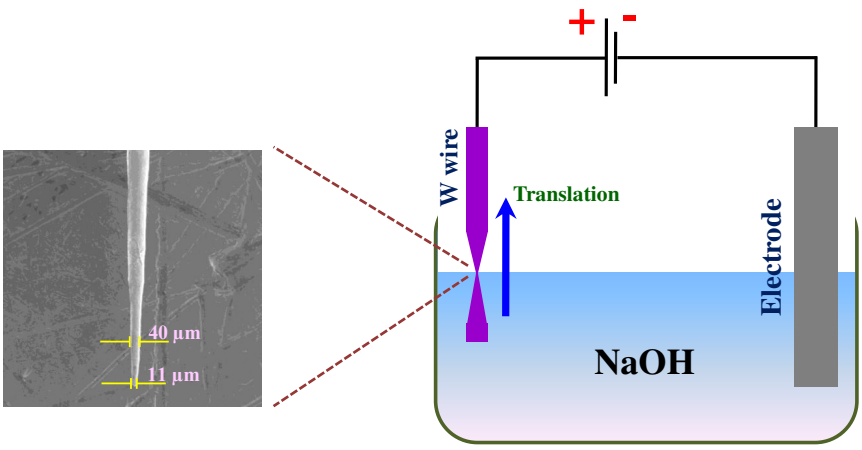


Figure 5.7: Electro-chemical etching setup. Tungsten wire with 0.4 mm diameter was connected to the positive electrode and was immersed in NaOH 2M solution. Negative electrode was placed onto a stainless steel column that is also immersed in NaOH. A DC voltage of 3V was applied to electrodes and the tip was moved very slowly by a distance of 50 μm for every 2 minutes. The fabrication taken 30 minutes and the tip with a diameter of 11 μm was obtained, as shown in the image in left.

by an electric field poling or a corona poling technique.

5.3.2.1 Corona poling technique

For the corona poling setup, a sharp tip is a very important element. Tungsten (W) tip was prepared by an electro-chemical etching technique. The fabrication of such tip is shown in Figure 5.7. A tungsten wire of 0.4 mm diameter was immersed in a 2M NaOH solution, and a DC voltage of 3V was applied to electrodes. The electro-chemical redox reaction can be expressed as follow:

$$\mathrm{W(s) + 2OH^- + 2H_2O \longleftrightarrow WO_4^{2-} + 3H_2 \uparrow} \tag{5.27}$$

The tip was then moved slowly in vertical direction by a distance 50 μm for every 2 minutes. The etching process was finished when the sharp tip is arrived at the interface of NaOH solution and air. Figure 5.7(left) represents a SEM image of the fabricated tip

with a diameter of 11 μm.

5.3.2.2 Corona poling process

The W-tip is connected to the positive electrode of a high DC voltage (4.5 kV) in corona poling setup as shown in Fig. 5.8(a). The QPM sample is placed on a hot plate and connected to the negative electrode of the DC source. The distance from the W-needle and the face of the poling sample is about 2 cm. The poling efficiency depends on this distance, on the quality of the sample and on the surrounding atmosphere.

Once a high voltage (4.5 kV) is applied to the W-needle, the surrounding air will be ionized and acted on the sample surface. High electric field is created inside the sample and orient the polymer's dipoles. The orientation of copolymer molecules will remain relatively unchanged unless the sample is heated. Therefore, the sample is heated to 110°C, temperature being below the glass transition temperature of DR1/PMMA copolymer (T_g = 125°C). The heating and cooling rates affect significantly to effective corona poling. In our case, the sample is ramped up from room temperature to 110°C for 10 minutes at the normal atmosphere. Then the high voltage (4.5 kV) is applied for 30 minutes (at 110°C). Finally, the temperature is cooled down to ambient temperature while the poling field was maintained. This is an important step because it allows the polymer's dipole solidifying while aligned. A whole of corona process, represented in Fig. 5.8(b) finishes in 60 minutes and the sample became a QPM structure with a spatial periodic modulation of nonlinear property $\chi^{(2)}/0/\chi^{(2)}/0/\chi^{(2)}$... according to the alternation between DR1/PMMA and SU8 materials. This corona poling technique was employed for creation of all 1D and 2D QPM structures studied in this thesis. We note that the same technique could be used to obtained 3D QPMs, that cannot be achieved by other techniques.

5.3.3 Experimental results

A schematic presentation of optical setup to measure SHG signal is given in Fig. 5.9. In this setup, a SuperK COMPACT supercontinuum lasers of NKT Photonics Corp. (λ = 440 - 2400 nm) with a repetition rate of 25 kHz, a pulse width $<$ 2 ns and an average power of 109 mW is used as fundamental light source. The incident beam is spectrally selected by a band pass filter and then focused to the sample by an objective lens. The

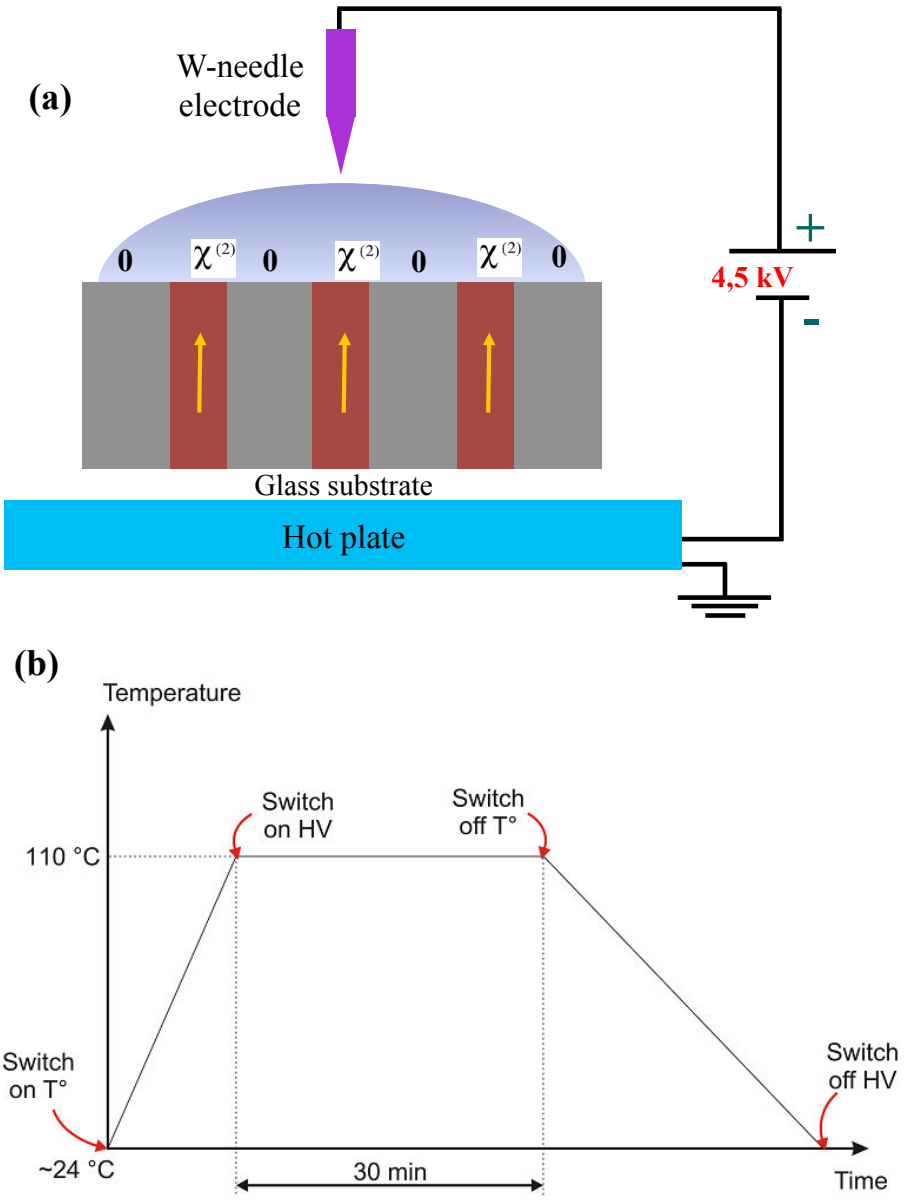


Figure 5.8: (a) Corona poling setup. The W-tip, which is etched by electro-chemical etching, was connected to the positive electrode of a high DC voltage source. The sample was connected to the negative electrode and placed on a hot plate. When a high voltage (4.5 kV) is applied, an arc electric appears on the sample surface and align DR1 molecules of nonlinear material (DR1/PMMA). The linear material (SU8) is not affected. (b) The corona poling process. At the beginning, the sample is heated from room temperature to 110°C, then, high voltage is applied for 30 minutes. Finally, the sample is cooled down to ambient temperature (hot plate is off) while the poling field is kept on.

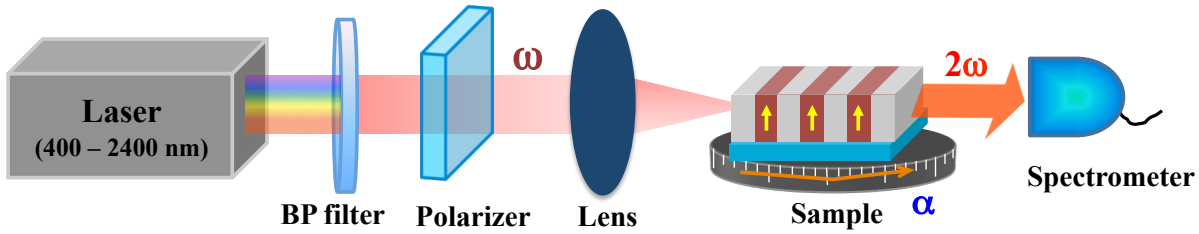


Figure 5.9: SHG setup in longitudinal QPM configuration. A band pass filter selects the fundamental beam from a white light source. This beam (linear polarization) is sent to the sample via an objective lens. The sample is fixed on a rotation stage, which allows to vary the angle between the sample and the laser beam. The SHG signal is collected by a spectrometer.

polarization mode of fundamental beam is ensured by a polarizer. The QPM sample is placed on a rotational stage, which can control the orientation between the fundamental beam and the sample by an angle α. The SHG signals are finally detected by an Ocean spectrometer.

In this experiment, we have used a band pass filter with a wavelength centered at 1400 nm. To investigate the enhancement of SHG signal by QPM structure, the samples were designed and fabricated with parameters corresponding to this fundamental wave. SHG signal from a poled DR1/PMMA uniform film is also measured to compare with those obtained by the QPM structures.

In practice, there exist different ways to send the fundamental beam into the QPM structures. The fundamental laser beam can propagate in parallel or in perpendicular (or at an arbitrary angle) to the grating vector of the QPM structures. This leads to different types of SHG, which satisfied the momentum conservation law such as: collinear QPM or longitudinal QPM (the fundamental and SH beams propagate in parallel to the QPM grating vector), Raman-Nath [167] that refers to as transverse QPM condition, and Čerenkov SHG [168], which can be realized with and without QPM condition, etc.

In our experiments, we have tried with different possibilities. Figure 5.10 shows the SHG wave at 700 nm obtained with an uniform poled film DR1/PMMA and with a 1D QPM structure in the frame of collinear QPM. The sample was rotated by an angle α

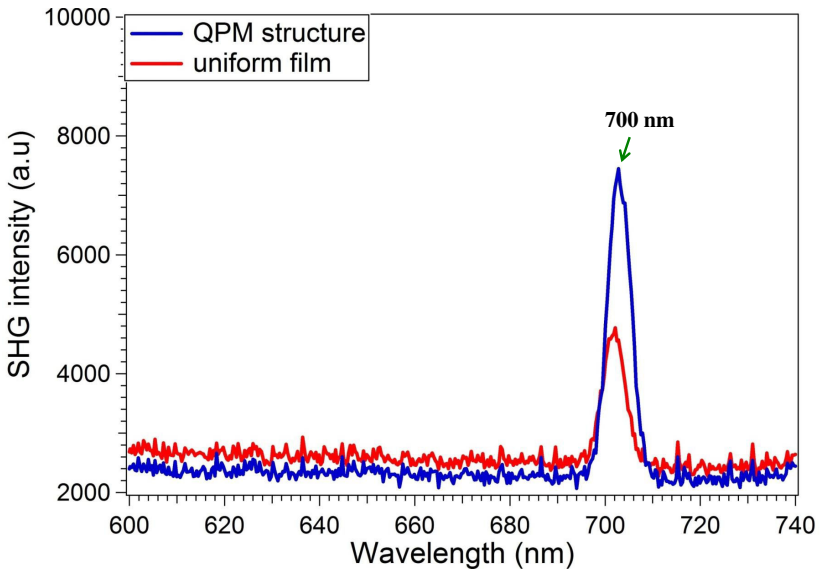


Figure 5.10: SHG wavelength at 700 nm of a poled uniform film and a poled QPM 1D structure with fundamental wave at 1400 nm.

to optimize the SH signal. In the optimum condition, it can be seen that, the SH signal produced by QPM structure is slightly higher than that of a DR1/PMMA copolymer thin film. The role of QPM structure in increasing the conversion efficiency is therefore not very much and depends strongly on the position of the focal spot with the domain walls. This can be explained by the fact that the QPM structure has limited thickness, and it is very difficult to coupling the fundamental light into the QPM structure and to let it propagating through the length of the crystal. Actually, the fundamental light has been focused into the QPM structure and immediately went out of the crystals. With limited film thickness, it is difficult to realize standard QPM technique (collinear propagation) to have high SHG efficiency.

We then considered two latter cases by sending the fundamental beam in perpendicular direction with respect to the grating vector. Figure 5.11 illustrates the experimental setup used for this measurement. The fundamental laser beam was sent into normal direction with respect to the sample surface. The disadvantage of this technique is the limited propagation length due to the film thickness of the QPM structure, which results in a weak SHG effect. However, this way allows to manipulate the SHG signal and beam profile at the output of the crystal, and that can be interesting for some applications such

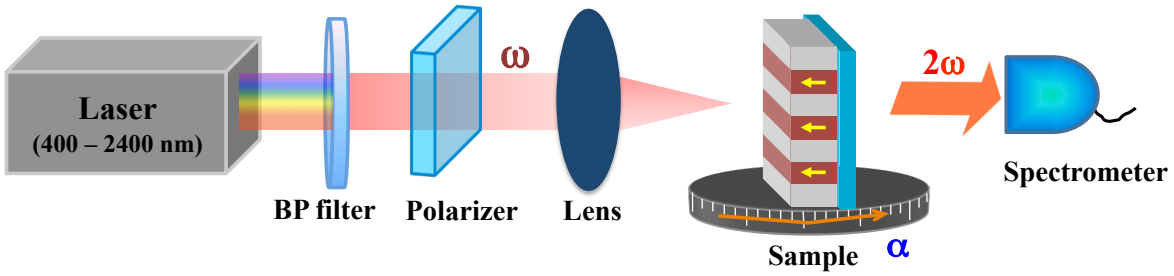


Figure 5.11: SHG setup in transverse QPM configuration. A band pass filter selects the fundamental beam from a white light source. This beam (linear polarization) is sent to the sample via an objective lens. The sample is fixed on a rotation stage, which allows to vary the angle between the sample and the laser beam. The SHG signal is collected by a spectrometer.

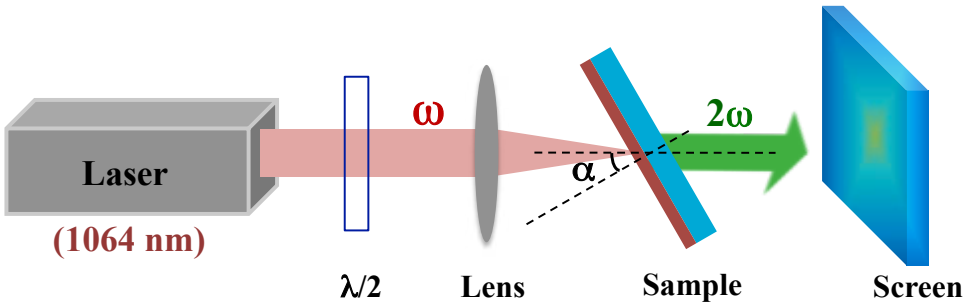


Figure 5.12: Experimental setup using a fundamental wave at 1064 nm. The half-wave plate is used to control the polarization of fundamental laser beam. The beam is then focused by a lens into the QPM sample which can be rotated an α angle around propagation axis.

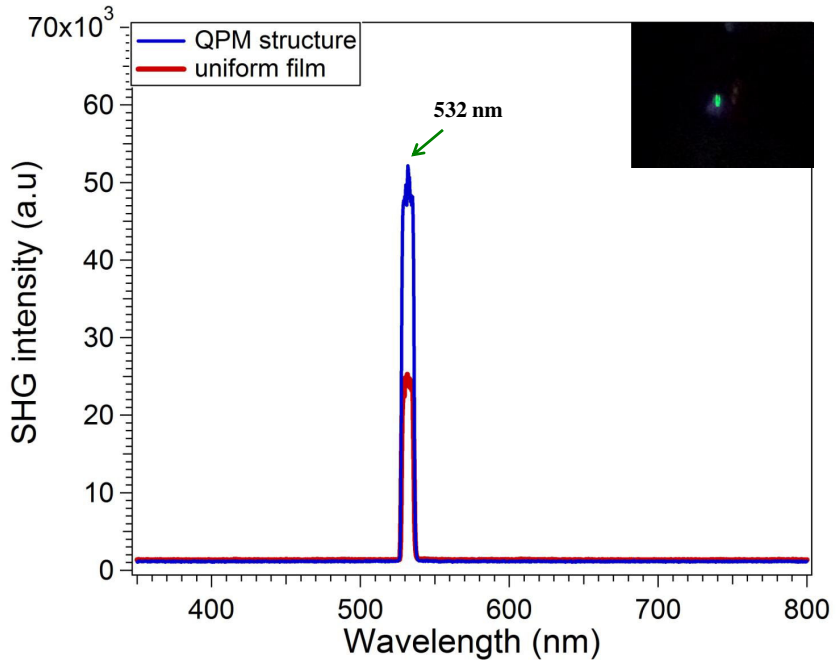


Figure 5.13: SHG signal generated by a fundamental laser at 1064 nm on an uniform DR1/PMMA film and on 1D QPM structure. The inset shows a SHG image achieved by the QPM structure.

as beam shaping.

In this case, because the SHG signal was created from a laser source (fundamental wavelength = 1400 nm) with a modest average power (about 100 μW), the SH signal was detected by the spectrometer, but it was not possible to be observed by eye or by an infrared card. Therefore, it is impossible to analyse the type of SHG, *i.e.* Raman-Nath or Čerenkov SHG. No nonlineat diffraction orders was observed. Therefore, in order to observe the SHG signal by eye to easily understand what happens when working with transverse QPM, we have built a new experimental setup using a stronger excitation source (pulsed laser with an average power of 80 mW) at the wavelength of $\lambda = 1064$ nm.

Figure 5.12 illustrates this new experimental setup. By using either a polymer thin film or a QPM structure fabricated on DR1/PMMA, the SHG signal can be easily obtained on a screen and can be observed very clearly by eye, as shown in inset image of Fig. 5.13. The image shows a green spot corresponding to the wavelength 532 nm, *i.e.*, SH wave of 1064 nm. The intensity, which is measured by spectrometer, is still only a bit larger

than that obtained by an uniform film. However, there is no evidence about the nonlinear diffraction, and we cannot clearly explain the Raman-Nath or Cerenkov effect.

However, we observed a diffraction effect of the fundamental beam, which allows to explain why the SH signal is quite weak. Indeed, by using a sensitive infrared camera or infrared card (see Fig. 5.14), we observed a strong diffraction pattern of the fundamental beam. In fact, there is a difference of refractive indices between DR1/PMMA and SU8 materials, as shown in Fig. 5.4(a). This difference creates a $\chi^{(1)}$ grating, which diffracts both fundamental and SH waves, thus reducing the SHG signal. Moreover, SEM images, shown in Figs. and , indicate that the SU8 structure filled with DR1/PMMA copolymer does not have flat surface. This effect is illustrated in Fig. 5.15(a). It causes an air/polymer grating, which results in a strong diffraction effect of the fundamental wave and thus decrease the SHG signal. As future work, we propose to overcome this effect by preparing a thick film and etching it to get flat surface, as illustrated in Figs. 5.15(b) and (c).

5.4 Discussions and Conclusions

In summary, in this chapter, we have studied theoretically and experimentally the QPM technique to improve the frequency conversion efficiency. Firstly, the double frequency (SHG) effect was investigated in details and QPM technique, which is easy and efficient way, was chosen to compensate the phase mismatch. Then, the theory for 1D and 2D QPM structures was analyzed. 1D QPM is the well-known structure, which was proposed in a pioneering paper on frequency conversion. However, it allows to optimize the SHG in an unique direction. Whereas 2D QPM, which was proposed by Berger, can generate simultaneously multiple SHG in different directions. We have fabricated two kinds of QPM structure by two-beam interference technique to improve the conversion efficiency.

This fabrication technique used SU8, a linear material, as a template, then filled DR1/PMMA nonlinear material. QPM fabricated structure was then verified by transmission microscope and SEM. A home-made corona poling setup was then applied to create the nonlinear property of DR1/PMMA material. We also fabricated an uniform DR1/PMMA film for reference. Two setups with different excitation laser sources were

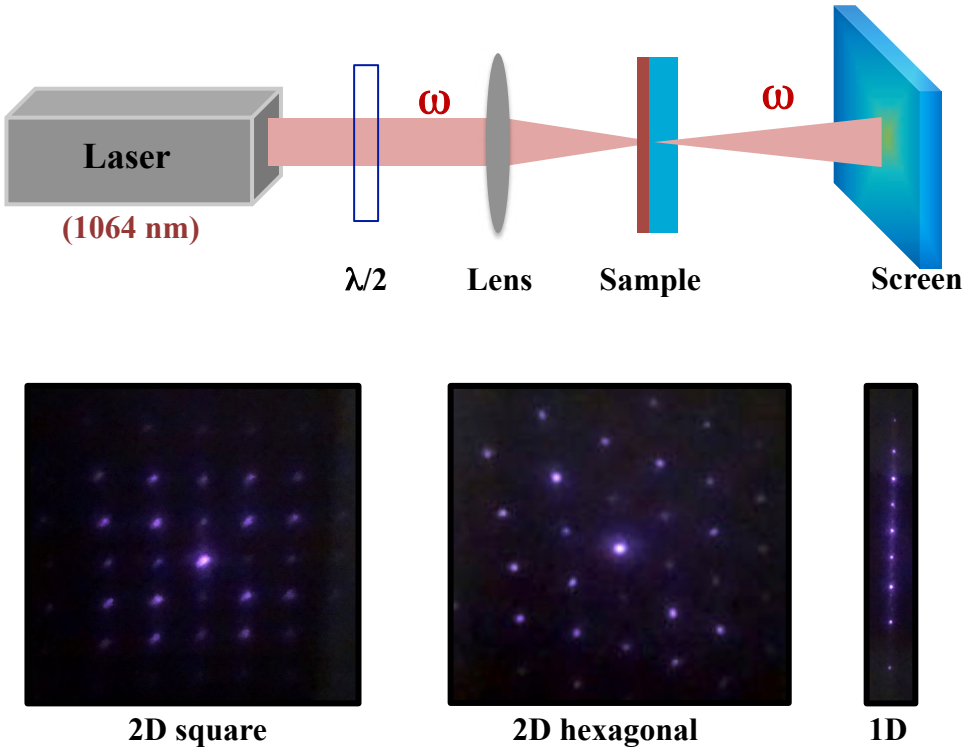


Figure 5.14: Diffraction effect of the QPM structures, observed by the fundamental beam at 1064 nm. Top: experimental setup; Bottom: diffraction patterns obtained by 1D and 2D (square and hexagonal) structures.

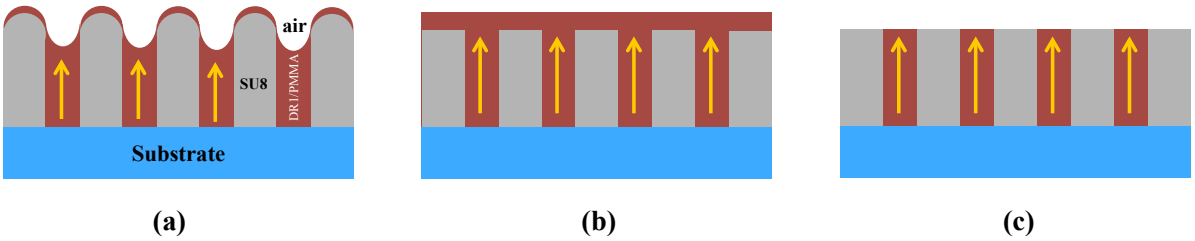


Figure 5.15: (a) Illustration of the air/polymer grating caused by the non-flat surface of SU8 structure filled with DR1/PMMA. (b) and (c) Overcoming this effect by filling a thicker DR1/PMMA layer into the SU8-based photonic structure by spin coater and following with an etching process to obtain a flat SU8/DR1/PMMA surface.

built to measure the SHG signal of QPM structures. Firstly, the laser beam with a wavelength of 1400 nm separated from a white light pulsed laser was used as a fundamental wave. The SHG signal at 700 nm was obtained at the longitudinal QPM condition. Nevertheless, the intensity of this fundamental wave is too weak (about 100 μW) and this QPM condition is also sensitive to the position of the focal spot, whereas, the thickness of structure is too thin to coupling in the fundamental beam. Therefore the SH signal is not so high and cannot be seen by eye or by an infrared card. In order to observe the SHG signal to understand more about QPM technique, a higher power laser was used. A Nd:YAG pulsed laser with an average power of 85 mW was used and generated very strong SH signal that can be caught on a screen. However, when comparing the measured signal to that obtained by an uniform film, the conversion efficiency from QPM structure is just a bit higher. This result may be explained by many reasons. Firstly, the thickness limitation of structure leads to difficulty in coupling the fundamental wave into QPM structure. For the future work, this drawback could be overcome by increasing the thickness of SU8 sample to let the fundamental light pass through the QPM structure. The second reason is the $\chi^{(1)}$ grating, which causes by the difference of refractive indices of SU8 and DR1/PMMA materials. This grating diffracts both fundamental and SH waves. In order to remove completely this grating, DAST (4-N,N-dimethylamino-4′-N′-methylstilbazolium tosylate) microcrystals doped in SU8 film or DR1/SU8 structure, etc., are proposed. The air/polymer grating, which is formed by the non flat surface of QPM structure, also diffracts strongly the fundamental wave and thus reduce the SHG signal. This reason can omit by covering SU8 structure with thicker layer of DR1/PMMA, following an etching process to obtain a flat SU8/DR1/PMMA surface. All these solutions will be continued in the future works.

Moreover, this fabrication technique opens a potential way to fabricate 3D QPM, which is extremely difficult and not successful up to now.

Chapter 6

Optimization of nonlinear optics effects by waveguide resonance grating (WRG) coupling

Waveguide resonant grating (WRG) combines characteristics of diffraction by periodic structures (also called surface relief gratings) with waveguide properties. This structure allows light diffracted by the grating coupling to a mode of the waveguide and generates very sharp reflection and transmission anomalies associated with the guided mode resonance (GMR) effect [169]. WRG at the resonant mode can produce strong local field at the surface of the grating, which is very useful for numerous applications such as the narrow band filters [170], nonlinear optical process, optical switch [171], and high-sensitivity sensors [172], etc. Especially, WRG can be used to enhance the fluorescence signal [173] or the second-harmonic generation (SHG) of the materials [61, 62]. There are many WRG configurations [174, 175], each of them possessing own advantages and proper applications.

In this chapter, we investigated theoretically and experimentally the so-called all polymer-based WRGs and we demonstrated their applications for enhancement of SHG.

6.1 Theoretical calculation

6.1.1 Property of WRG

A WRG consists of at least one diffraction grating deposited onto one waveguide. Resonance effect occurs when the incident light diffracted from the grating couples to the guided modes of the waveguide.

A diffraction grating splits and diffracts incident light to several beams propagating in different directions. The diffraction configuration when an incident light comes to a 1D surface grating is illustrated in Figure 6.1. The directions of these beams (also called the angles of the diffracted modes) are related to the wavelength and grating parameters through grating equations as follow:

- Reflection region:

$$n_{\mathrm{ref}} \sin \theta_{\mathrm{m}} = n_i \sin \theta_{\mathrm{i}} - m\frac{\lambda}{\Lambda}, \tag{6.1}$$

- Transmission region:

$$n_{\mathrm{tr}} \sin \theta_{\mathrm{m}} = n_i \sin \theta_{\mathrm{i}} - m\frac{\lambda}{\Lambda}, \tag{6.2}$$

where:

- n_{ref}, n_{tr} and n_{i} denote the refractive indices of reflection, transmission and incident regions, respectively.

- θ_{i} and θ_{m} are the incident angle and angle of m^{th} diffraction mode, respectively.

- λ and Λ denote the wavelength of incident beam and the grating period, respectively.

The grating equation only informs the directions of the modes and do not allow to quantitatively evaluate the intensity of each diffractive beam. The later one depends strongly on parameters of grating, in particular the grating shape. Figure 6.1 illustrates, for example, a grating with a sinusoidal profile.

A waveguide is a structure that guides electromagnetic waves. There are many different geometries of waveguides, which are used for different purposes. Light is confined in the waveguide by total internal reflection effect. When a diffraction grating and slab waveguide are brought into proximity and the angle of a diffracted mode matches the angle of a guided mode, the resonance effect happens. The regions of guide-mode resonance are

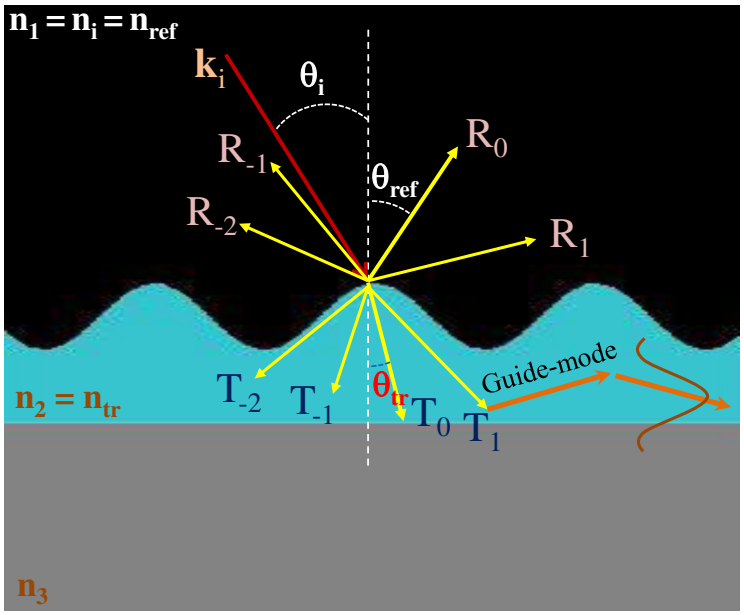


Figure 6.1: Configuration and mechanism of a waveguide resonant grating. The angles θ_{ref} represent the angles of the wave vector of the m^{th} reflected wave with respect to the z axis. The angle θ_{tr} are the corresponding angles for the transmission waves. The angle of incidence θ_{inc} is arbitrary. When the angle of a diffracted light from a surface grating matches the angle of a guided-mode of waveguide, the resonance effect occurs.

predicted by the inequality [176]:

$$\max\{n_1, n_3\} \leq |n_1 \sin\theta_{\text{i}} - m\frac{\lambda}{\Lambda}| < n_2 \tag{6.3}$$

where n_1 and n_3 are the refractive indices of the media surrounding waveguide-grating, n_2 is the refractive index distribution of grating layer.

However, in order to correctly calculate the response of a WRG structure, it is necessary to numerically model the WRG structure and realize the calculation from fundamental Maxwell's equations.

6.1.2 Numerical calculations

6.1.2.1 Numerical method

There exists different simulation methods allowing to model an arbitrary WRG structure and to obtain its optical properties. Each method presents its own advantage, such as

required time processing, computer memory, or simulation precision. In this work, we adopted a very well-known simulation method, finite-difference time domain (FDTD), which allows to achieve rapidly and precisely the optical properties of all polymer-based WRGs. This method allows us to get the approximate solutions of electrodynamics problems. FDTD workground was first set in 1928 with the publication of Courant, Friedrichs and Lewy. However, it only became popular since 1980s thanks to the revolution of information technology [177]. Recently, with the assistance of modern computers, FDTD becomes a powerful technique for researchers to predict the electromagnetic response of any structure, for example, WRGs.

As the other finite-difference modeling methods, FDTD is grid-based. It means that computational domains will be meshed into minor units, mostly in cube shape, with associated vector components of the **E** field and **H** field, which are firmed by Maxwell equations. In simulation, the **E** and **H** fields are determined at every point in space, forward in time. On the other hand, FDTD is a time-domain method, so it can cover a wide frequency range with a single simulation run. Thanks for these advantages, FDTD provides us a natural way to treat with any electrodynamics problems, especially with periodic structures and broadband-sources in WRGs complications [178]. Consequently, we chose FDTD method and commercial Lumerical^{TM} FDTD software for our study.

6.1.2.2 Simulation parameters

Thanks to the flexibility of FDTD method and Lumerical software, various WRG configurations, published in literature, have been verified with excellent agreement. Indeed, we are able to construct multilayer or monolayer models, with changeable grating parameters (period, depth, refractive indices, etc.), sources parameters (wavelength ranges, incident angle, polarizing modes, etc.) and grating profiles (1D or 2D, wavy, blade or square, etc.). We note that in such software, grid resolutions and boundary conditions need to be chosen precisely to avoid systems errors and compromise simulation times as well as simulation accuracies. Different WRG structures have been investigated, which provided different interesting properties. In order to compare with the experimental results realized in this work, we present in this dissertation only the 1D WRG case with a sinusoidal profile, as shown in Fig. 6.2. The simulation parameters, for different simulations presented in dif-

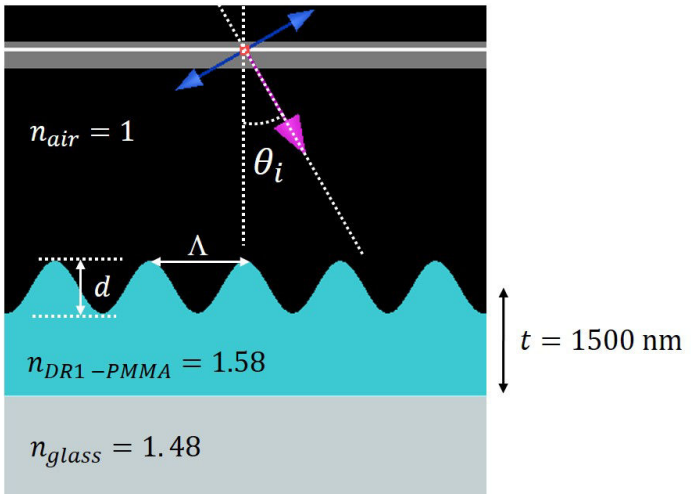


Figure 6.2: 2D side view of simulating model for a all-polymer-based WRG. The swept parameters used in simulation are Λ = 800 - 1200 nm, d = 50 - 400 nm, θ_i = 0° - 60°, λ = 800 - 1000 nm and source modes TE, TM. The fixed parameters are t = 1500 nm, refractive indices of glass, DR1/PMMA and air are 1.48, 1.58 and 1, respectively.

ferent sections of this chapter, were selected and categorized into two groups as describing below:

- Fixed parameters:

  The 1D sinusoidal grating profile was chosen, because it is the most similar to structure fabricated by two-beam interference method (see chapter 4). Neglecting the dispersion effect, the refractive index of glass, DR1/PMMA and air were kept at 1.48, 1.58 and 1, respectively. The thickness grating combined with waveguide is t = 1500 nm. Note that those values are close to experimental parameters.

- Swept parameters:

  We swept the grating depth from d = 50 nm to d = 400 nm and period from Λ = 500 nm to Λ = 2000 nm. Incident angle, wavelength, and source mode were also varied from θ_i = 0° to θ_i = 80°, λ = 400 nm to λ = 2000 nm from TE to TM modes, respectively. In addition, monitors were set within computation domain to analyze reflection spectra along with electromagnetic field distributions. Results were normalized to the reflection spectra obtained from a thin films (no grating)

and evaluated right after each simulation to confine the parameters, with a purpose of the fastest convergence.

6.1.2.3 Simulation results

Figure 6.3 shows simulation results of reflections spectra as a function of excitation wavelength and of incident angle for 1D sinusoidal WRG with $\Lambda = 1000$ nm. As can be seen in Figs. 6.3(a) and (c), at grating depth d = 50 nm, there are two curves of resonant peaks across downward from left-top to the right. If we kept unchanged all the parameters while increase the grating depth to d = 400 nm, the resonant peaks slightly shift to the left and become much more distinguishable (Figs. 6.3(b) and (d)). This resonant peaks of a grating coupled to a waveguide can be explained as following: basically, a WRG is consisted of a low refractive index substrate and a high refractive index waveguide, covered with a grating layer (lower effective refractive index); when a light beam is sent to the surface of the grating, it will be diffracted towards the waveguide, and can be coupled into guided-mode. This leads to a strong local field resonance. In the resonance mode, strong local electrical field at the grating layer will be generated as shown in Fig. 6.4. The light can be then coupled out by the same grating, resulting in an enhancement of reflection signal. This WRG therefore produces very sharp reflection peaks and transmission dips, if the income lights are under resonant conditions, i.e., appropriated incident angle, frequency and polarization. It is evident that there exists the resonances for both TE and TM modes, which are very close to each other. The reflection intensities of these modes are slightly different, as it will be shown and compared with experimental results in next section. According to these results, we emphasize on two remarkable reflection peaks around $\lambda = 850$ nm - 950 nm, when a light beam is oriented at the incident angle of $\theta_i = 35° - 45°$. Furthermore, the peak is red shifted when the incident angles are decreased and vice-verse. By achieving sharp reflection peaks in simulations, we can handle all WRG parameters needed for resonance, which can be used for fabricating WRGs with selective properties.

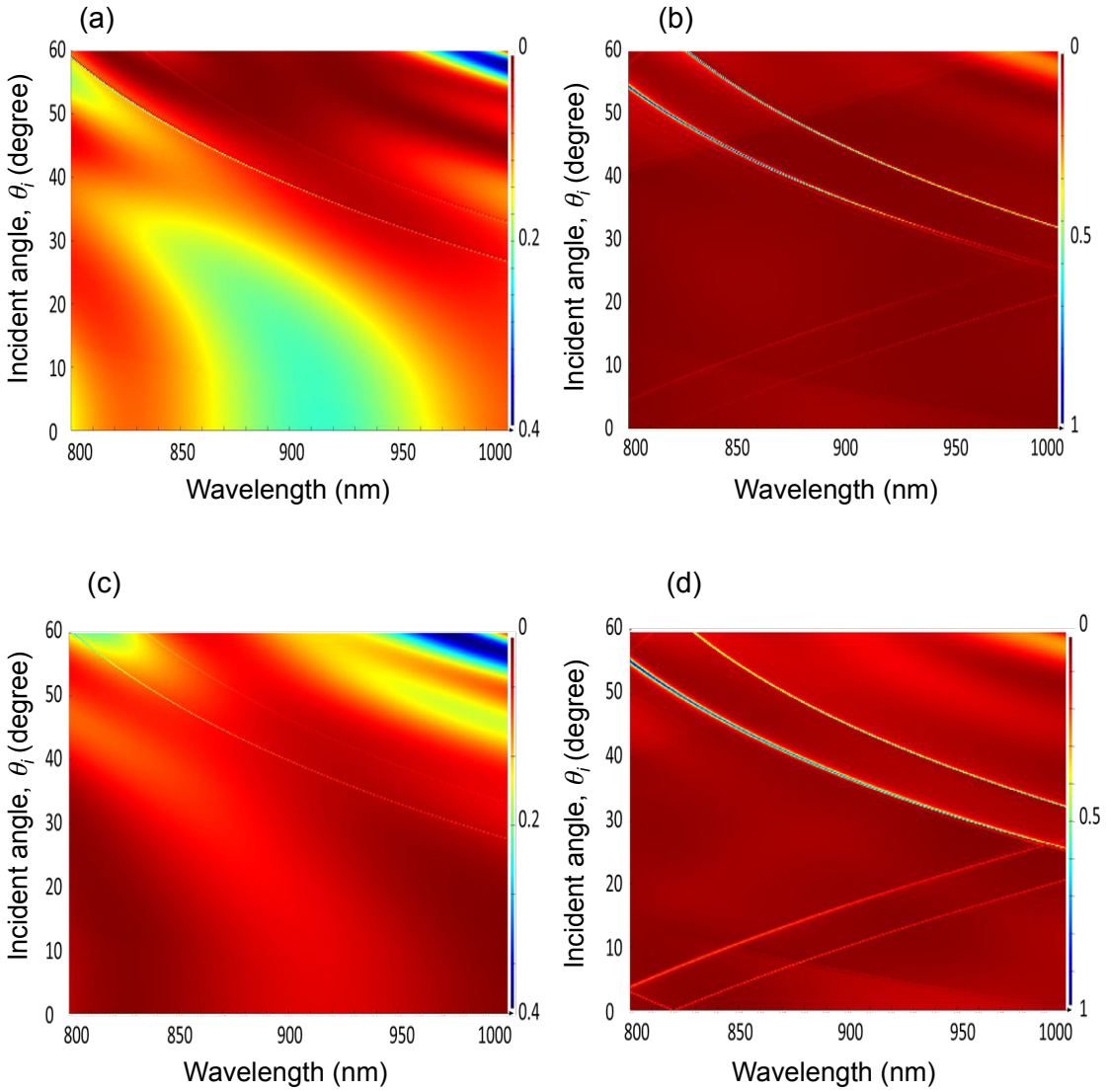


Figure 6.3: Mapping of reflection intensity as a function of incident angle (θ_i) and wavelength (λ) of a light beam directing to 1D surface grating (Λ = 1000 nm). (a) TM mode, d = 50 nm. (b) TM mode, d = 400 nm. (c) TE mode, d = 50 nm. (d) TE mode, d = 400 nm.

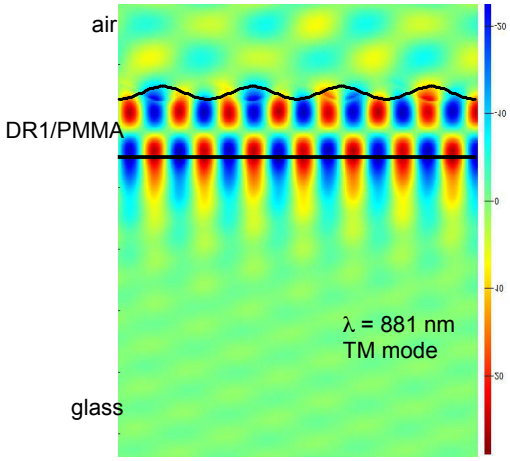


Figure 6.4: Strong local electrical field of 1D WRG with Λ = 1000 nm, grating depth d = 400 nm, at TM mode of λ = 881 nm.

6.2 Fabrication and characterization of all-polymer-based WRGs

6.2.1 WRGs structure based on copolymer DR1/PMMA

In the design of our WRG sample, both grating and waveguide were based on nonlinear polymer DR1/PMMA. Firstly, a polymer film was spin-coated on a glass substrate with a thickness of 1500 nm. Then a SRG was formed on the surface of this film by interference technique, similar to SRG formation process described in chapter 4. Different 1D SRGs have been fabricated according to the WRG simulation requirements.

6.2.2 Characterization of WRGs

To measure properties of WRG, the probe beam with λ = 800 - 1000 nm is sent to the sample and the zero-order diffraction (reflection beam) is monitored by a spectrometer. This probe beam makes an α angle ($\alpha = \theta$ in simulation) with respect to the sample surface. The depth of SRG and therefore the configuration of WRG can be controlled by the exposure time. The SRG period can also be easily changed by adjusting the incident angle of two interfering beam.

The resonance effect in WRG structure happens only for a certain wavelength and

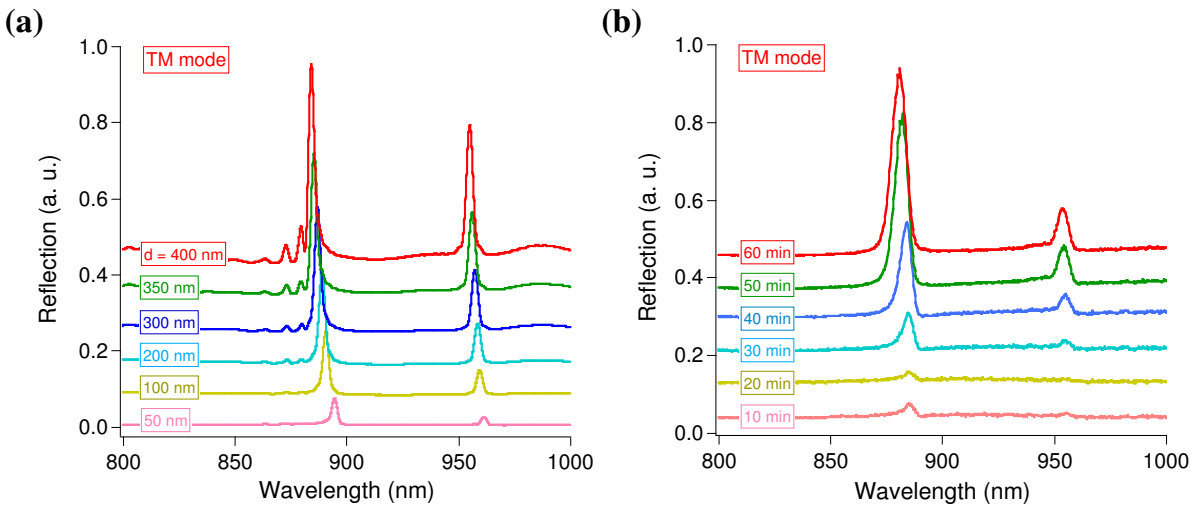


Figure 6.5: Reflection spectra of TM mode as a function of grating depth, measured at α = 40°. (a) calculation results; (b) experimental results.

incident angle of probe beam, depending on the grating parameters (period, depth, geometry...) and the refractive indices of the surrounding media.

At the GMR mode the very sharp reflection and near zero transmission anomalies are generated. To understand more about the WRG characteristics, we have monitored the reflected spectra as a function of grating depth and angle of the incident light.

6.2.2.1 Reflection spectra as a function of grating depth

Figure 6.5 shows the normalized reflecting spectra (TM mode, α = 40°) obtained at different exposure times, during the SRG formation. As we can observe in experimental results, there are two resonance peaks centered at the wavelength of λ = 880 nm and λ = 955 nm. Their amplitudes increase proportionally with the exposure times (as well as grating depths), which is perfectly consistent with the simulation results shown in Fig. 6.5(a). Furthermore, by calculations, we predicted that the resonant peaks are slightly blue-shifted with the SRG depth. That statement is also proven evidently by the experimental results. The reason of this moving is the changing of effective refractive index when the grating depth changes. In fact, there are some insignificant mismatches between the calculations and experiments. For instance, the resonant peaks in experimental results

seem to be broader than calculated ones, or there are some trivial peaks close to first significant resonant peak in simulations but not in experiments. That could be explained by the influence of the non-uniformity of SRGs, i.e., the variation of period and amplitude. The other minor factors such as spectra of probe source, refractive indices, measuring scale, etc., are also contributed to the difference between experiment and calculation.

6.2.2.2 Reflection spectra as a function of incident angle

The relationships between probe incident angle (α) and reflection spectra are illustrated evidently in Fig. 6.6. We note that the simulation results in Figs. 6.6(b) and (d) are extracted from the mapping results (Fig. 6.4). As the previous forecasts, in general, with both polarizing TE and TM modes, when we rise up the angle, the peaks will be shifted to the left. The shifted rates are about 8 - 10 nm/1°. Likewise, the relative distances between two resonant peaks slightly shrink also. The experimental results show a remarkable similarity to the theoretical predictions. Comprehensively, the two experimental resonant peaks are blue-shifted and closer apart to each other by the increment of the incident angle (α) for both TE and TM modes. The relative positions of resonant peaks in simulation and experiment also come to an agreement. Here again, there are some small differences between calculation and experiment. Besides the reasons stated in the last subsection, there are some additional factors such as error of rotating holders, alignment of the incident beam, etc.

At this moment, we conclude that it is possible to obtain a WRG using purely polymer materials. The theoretical and experimental results show a strong enhancement of reflection signal at some particular wavelengths corresponding to the GMR. This leads to many interesting applications, in particular for nonlinear optics effect of laser based on polymer materials.

In the next section, we will demonstrate an important application of such WRG.

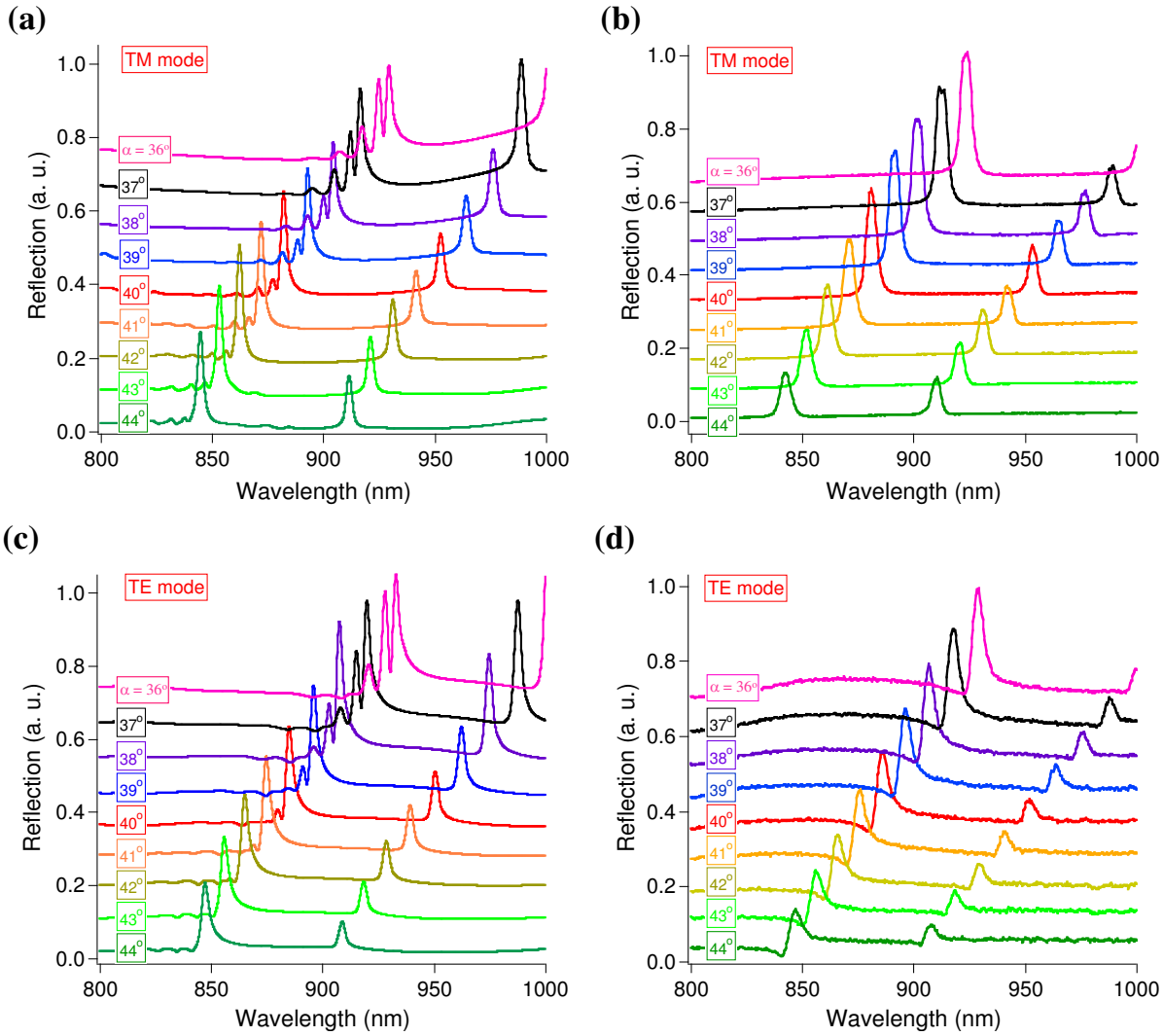


Figure 6.6: Reflection spectra as a function of incident angles (α), measured at maximal grating depth. (a) TM mode, calculation; (b) TM mode, experiment; (c) TE mode, calculation; (d) TE mode, experiment.

6.3 Enhancement of the second-harmonic generation by WRG coupling

According to the previous chapter, SHG intensity is given by

$$I_{2\omega} = \Gamma^2 d_{eff}^2 I_\omega^2 z^2 \sin c^2(\frac{\Delta k z}{2}), \tag{6.4}$$

where I_ω and $I_{2\omega}$ are the intensity of fundamental and SH waves, respectively. d_{eff} is the nonlinear coefficient and z is the length of nonlinear crystal.

We seen that the SHG intensity ($I_{2\omega}$) is proportional to the square of the intensity of fundamental wave (I_ω). The increase of the fundamental intensity leads to enhancement of the SHG signal. This suggests to employ the GMR effect of WRG structure. Indeed, if we can design and fabricate a WRG, which produces resonant peak at exact fundamental wavelength, the electrical field as well as the fundamental intensity will be improved dramatically, resulting in a high nonlinear conversion process.

The copolymer DR1/PMMA is a linear material under normal condition, i.e., the molecules are oriented randomly, hence the second-order nonlinear coefficient ($\chi^{(2)}$) is zero. To prepare for above purpose, all-polymer-based WRG structure needs to be reoriented by a corona poling method, which is already shown in the last chapter.

6.3.1 Dependence of SHG on incident angle (α)

First, we utilized a poled azopolymer film, without grating, to determine the relationship between the SH signal and the incident angle α, between the fundamental beam and the normal vector of sample surface. Figure 6.7 illustrates the experimental setup used to measure SHG signal of all polymer-based WRGs. The spectrometer shows obviously a SH signal at $\lambda_{2\omega} = 707$ nm as shown in the inset of Fig. 6.8. We then measured the intensity of this SH peak for different samples and at different α - angles. Theoretically, with $\alpha = 0°$, dipole vectors in sample are perpendicular to electrical vector of the fundamental beam, therefore, no SH is generated for the reason that there is no interaction between those vectors. By the increment of α - angle, the interaction is upturn. As the results, the SH signals rise up and get maximum when $\alpha = 90°$ or dipole vectors and electrical vectors are parallel with each other. However, experimentally, at very high α - angle,

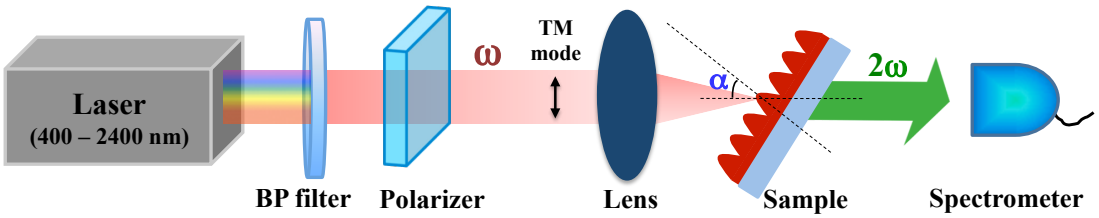


Figure 6.7: Experimental setup of SHG. A bandpass filter centered at $\lambda_\omega = 1414$ nm was used to select a "single" wavelength from a super-continuum light source. The laser beam is focused into the sample by a lens. The sample is positioned on a rotation stage, which allows to control the orientation of the sample with respect to the incident beam by an angle α.

fundamental light could not be coupled into the thin films and the SHG signal becomes weak. We found experimentally that the SHG signal reaches the highest value at $\alpha = 55°$ - $60°$, as shown in Fig. 6.8. This observation helps us optimizing the parameters of WRG structures. It means that we need to design and to fabricate a WRG, which can generate resonant peaks at a fundamental wavelength of $\lambda = 1414$ nm (chosen wavelength for demonstration) and at incident angle of $\alpha = 55°$ - $60°$.

6.3.2 Optimization of SHG signal by WRGs

By FDTD simulation, we found that the gratings whose periods (Λ) are in between 1600 nm and 2000 nm, can satisfy the criteria of producing resonant peak at $\lambda = 1414$ nm around $\alpha = 55°$ - $60°$. We therefore designed and fabricated different kinds of gratings with periods of $\Lambda = 2000$ nm, $\Lambda = 1800$ nm, $\Lambda = 1700$ nm, and $\Lambda = 1600$ nm, respectively. Figure 6.9(a) presents the mapping of reflection intensity as a function of incident angle (θ) and fundamental wavelength (λ_ω) of a TM mode. This result indicates a resonant peak at $\lambda_\omega = 1414$ nm corresponding a 55^o incident angle. Figure 6.9(b) compares the electrical field distributions between non-grating surface and a WRG with TM mode. The fundamental wave is enhanced thanks to coupling into resonant modes of WRG structure. Therefore, the SH signal is expected to be higher.

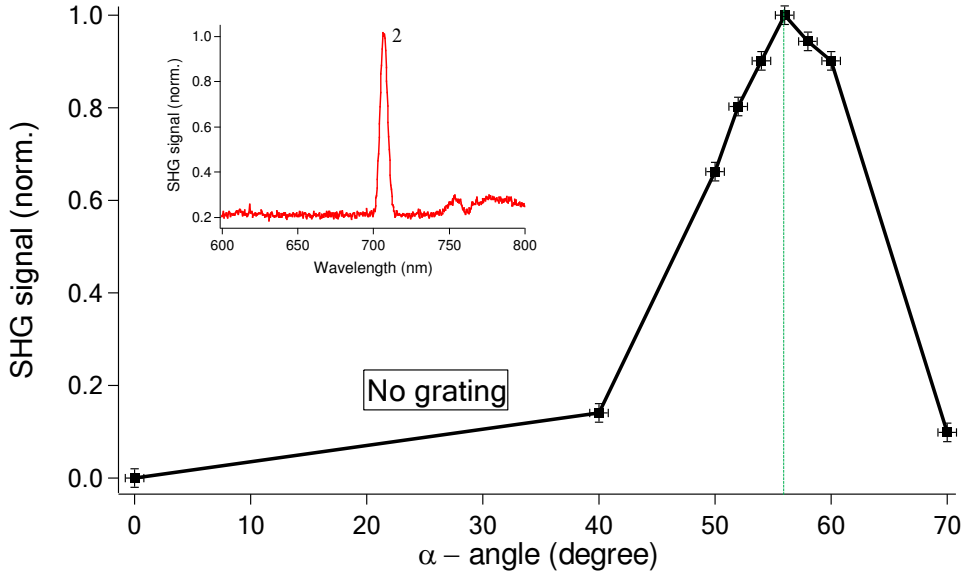


Figure 6.8: SHG signal generated by a DR1/PMMA copolymer thin film as a function of incident angle. Inset shows the SH spectrum at 707 nm.

The fabrication of WRGs were realized by the two-beam interference technique as previously demonstrated. Afterward, all these samples were corona poled and SHG were recorded by the experimental setup as shown in Figure 6.7.

As we can be seen in Figure 6.9(c), the SH signals in uniform thin film get maximum at angle $\alpha_{\max} = 55°$. By the first optimization of the grating sample, $\Lambda = 2000$ nm, the SH signal is enhanced due to the resonance effect at the incident angle of $\alpha = 62°$. This resonance angle decreases while the SH signal is strongly enhanced in case of grating samples possessing $\Lambda = 1800$ nm and/or $\Lambda = 1700$ nm, which are strictly consistent with the calculating results. The SHG is improved because of the fact that the resonant angle approaches to optimal $\alpha_{\max}$ - angle. Comparing to no-grating reference sample, the SH signal obtained by the WRG with $\Lambda = 1700$ nm is enhanced by 25 times.

6.4 Conclusions

In this chapter, we have successfully demonstrated the resonance of all-polymer based WRGs and their use for optimization of SHG signal. We first studied the basic theory

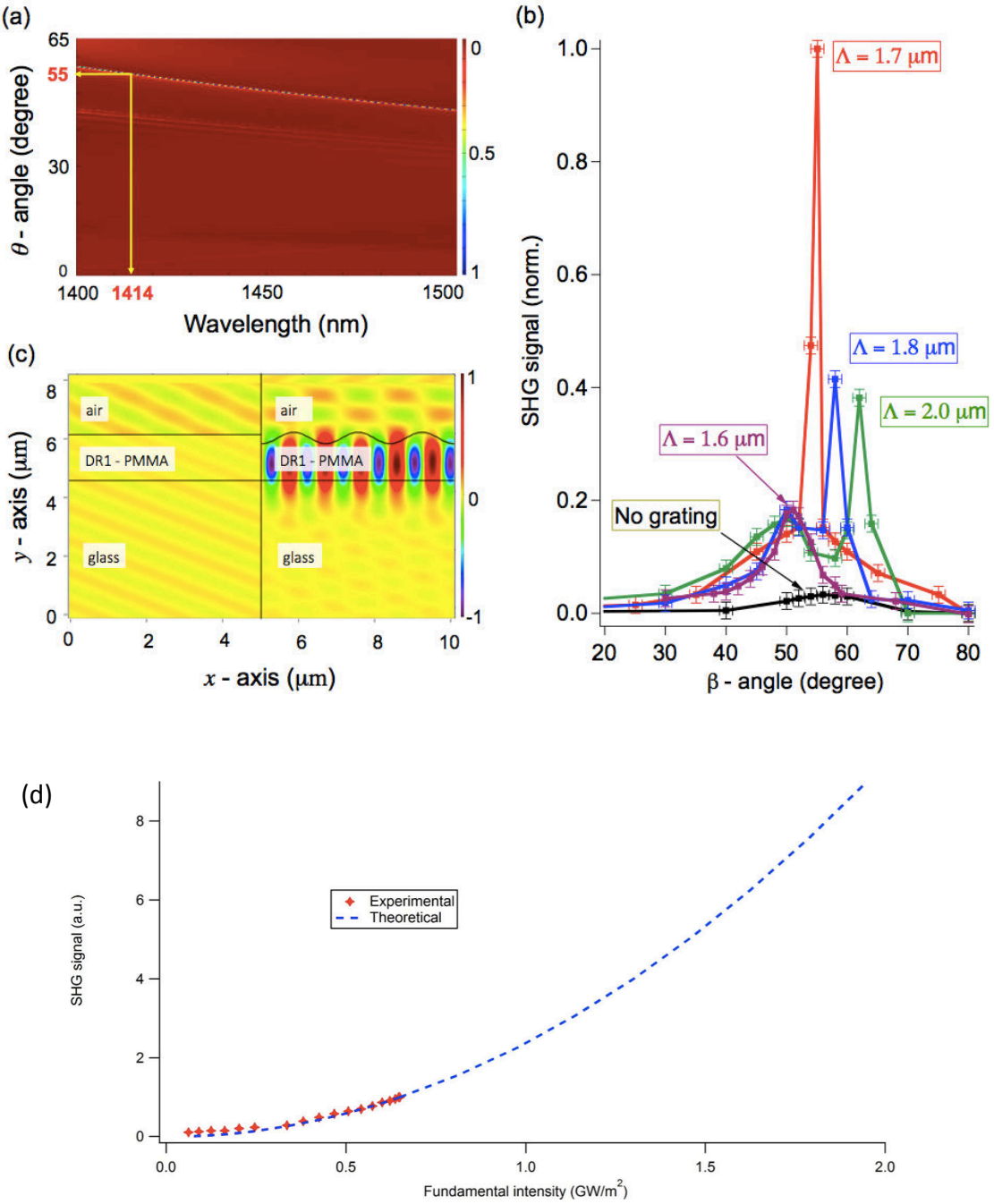


Figure 6.9: (a) Theory: mapping of reflection intensity (TM mode) as a function of incident angle (θ) and wavelength (λ) of a light beam sent to a 1D surface grating, Λ = 1700 nm; (b) Experiment: optimization of SH signal using WRGs with different periods (Λ). The signal was recorded at different incident angles (β) of the fundamental laser. (c) Theory: electrical field distributions (TM mode) of a light beam in an uniform surface (left) and a WRG (right) at a resonant wavelength $\lambda = 1414$ nm, as indicated in (a). (d) SH intensity ($I_{2\omega}$) as a function of fundamental intensity (I_{ω}).

of the resonant modes of a simple grating coupled waveguide. The exact optical properties of any WRG were then numerically simulated by using finite-difference time domain method, performed with a commercial Lumerical software. We are able to fabricate 1D SRGs in DR1/PMMA thin films by a simple interference technique, with designed parameters as well as characteristics. Thanks to the strong local electrical field in WRG, which are generated under guided-mode resonance condition, we demonstrated the SHG enhancement by a factor of 25, as compared to the result obtained by a sample without grating. It has a great agreement between theory and experiment. With 25 times greater than the uniform film, WRG structure has various promising applications such as plasmonic WRGs coupling, pulse-sharpers and sensors, etc.

Conclusion and Prospects

In this thesis, the potential in fabricating different geometries of photonic structures (PSs), such as one-dimensional, two-dimensional, and three-dimensional, periodic, or quasi-periodic of the two-beam interference method was theoretically and experimentally demonstrated. The fabricated structures are then applied for nonlinear applications to improve the frequency conversion efficiency.

In the first part, the advantages of two-beam interference technique comparing to other multi-beam interference techniques were analyzed. In fact, multi-beam interference method can create various types of photonic structures depending on the number and the configuration of interfering beams. Nevertheless, this standard method is very sensitive in beams alignment and non-flexible in fabricating different photonic structures. The two-beam interference technique associated with multi-exposure overcomes these problems and becomes a simple and efficient tool in PSs fabrication. Different PSs were fabricated as desired, using multiple exposures at appropriate orientation of the sample. The period of PS changes easily by varying the angle between two interfering beams. Specially, this setup allows the fabrication of 3D structures with close lattice constants in three dimensions, which is difficult to be achieved by multi-beam interference method. However, fabrication of an uniform and thick PS is a common problem of the optical lithography, in particular, the interference method. Indeed, the influence of material absorption on the uniformity of structures is significant when increasing the sample thickness. We have demonstrated a method which allow to compensate the diminution of the interference pattern intensity, due to the absorption effect, by an uniform assisted beam propagating in opposite direction with respect to two interference beams. In such situation, the final structure is always determined by the two-beam interference pattern, but the experimental results shown that the fabricated structures are uniform and their thickness can reach 25 μm. To

continue raising the thickness of PS, the very low absorption effect of used material was applied. Indeed, by using a high power laser at $\lambda = 532$ nm, it was demonstrated that PSs with a thickness as thick as 600 μm can be fabricated in SU8 negative photoresist. Nevertheless, the thermal effect due to long exposure time and high power of the excitation laser limits the use of this technique. Besides, SRG, one of interesting PSs was also fabricated and optimized in this work. Two types of polymer (active and passive polymers) with two different mechanisms for grating forming were employed. The creation of SRG based on passive polymer (SU8) is due to the shrinkage effect of this negative photoresist whereas the one based on active polymer (DR1/PMMA) is due to the mass transport effect of DR1 molecules. We have also seen that the groove depth of SRG based on active polymer is deeper than that of passive ones. The dependence of grating depth on fabrication parameters was also investigated. These structures were then utilized in waveguide resonant grating (WRG) for enhancement of nonlinear conversion effect.

In the second part, the polymer-based PSs fabricated by two-beam interference technique were applied in nonlinear applications. In fact, one of the reasons for diminution of SHG signal in nonlinear materials is the mismatching effect, which caused the destructive interference of the SH wave along the propagation inside the nonlinear crystal. QPM structures solved this problem by a modulation of the nonlinear coefficient, $\chi^{(2)}$, in periodical manner. In this work, the fabrication and characterization of 1D and 2D QPM structures have been realized. In order to fabricate QPM structures, two steps are required. Firstly, 1D and 2D PSs with a modulation of refractive index, between SU8 and air, were prepared. Then, the nonlinear material (DR1/PMMA) was filled in the air holes positions. The modulation of nonlinear susceptibility $\chi^{(2)}$ is obtained by using corona poling technique. The enhancement of SHG in all polymer-based QPM structures were then characterized. It is worth to mention that the SHG signal generated by QPM structures only reached a factor of 2 comparing to the result obtained by a homogeneous nonlinear film. Different reasons for this low conversion efficiency were identified. The optimization of QPM structures parameters for higher conversion efficiency is proposed as prospect of this work. Besides, we have demonstrated an alternative way to enhance the nonlinear conversion efficiency by increasing the fundamental intensity thanks to the strong local field in guided-mode resonance of WRG structure. This WRG structure is

engineered by a combination of a SRG and a waveguide based on DR1/PMMA active polymer. The theoretical, numerical and experimental of guided-mode resonance effect of WRG structure have successfully demonstrated. The WRG structure was simulated by using finite-difference time domain (FDTD) method and experimentally realized by two-beam interference technique. The optical measurements were also performed such as the relationship between probe incident angle and reflection spectra or the proportion of grating depth and reflection spectra. In particular, the strong local field at guided-mode resonance of WRG was employed to enhance the SHG signal by a factor of 25, as compared to the SH signal generated by the sample without grating. This result opens promising applications in photonic devices.

In summary, this work has successfully used the two-beam interference technique for fabrication of various types of polymer-based PSs. 1D, 2D, and 3D periodic and quasi-periodic PSs were fabricated with controllable parameters. The applications of these structures for nonlinear optics were investigated. This work can be continued with some prospects detailed as follow:

- It is necessary to optimize the ultra-thick photonic structures fabricated by very low absorbance of material at visible range. To eliminate the thermal effect, it requires to reduce the exposure intensity of the excitation source. A little bit increase of the material absorption by adding photo-initiator may be a solution. These structures then become good candidates for 2D and 3D QPM structures.

- We will continue the optimization of all polymer-based WRG structures for increasing the frequency conversion efficiency. Besides, the use of WRG structures for other applications such as enhancement of fluorescent signal or laser effect will be investigated.

Bibliography

[1] P. Vukusic and J. R. Sambles. Photonic structures in biology. *Nature*, **424**:852, 2003.

[2] Cas Smith. http://www.terrapinbrightgreen.com/blog/2014/06/biomimicry-photonics/.

[3] Dario Borghino. http://www.gizmag.com/moth-eye-biomimicry-safer-x-rays/23206/.

[4] U. Steiner. http://steiner.bss.phy.cam.ac.uk/people/copy-of-projects/photonic-structures-in-nature.

[5] J. V. Sanders. Colour of precious opals. *Nature*, **204**:1151, 1964.

[6] A. Blaaderen. Opals in a new light. *Science*, **282**:887, 1998.

[7] L. Reyleigh. On the remarkable phenomenon of crystalline reflecxion described by prof. stokes. *Phil. Mag.*, **26**:257, 1888.

[8] E. Yablonovitch. Inhibited spontaneous emission in solid-state physics and electronics. *Phy. Rev. Lett.*, **58**:2059–2062, 1987.

[9] S. John. Strong localization of photons in certain disordered dielectric superlattices. *Phy. Rev. Lett.*, **58**:2486–2489, 1987.

[10] I. Park, S. Kim, G. J. Lee, and Y. P. Lee. Design and optical properties of two-dimensional photonic crystals: A finite-difference time-domain numerical simulation study. *J. Korean Phys. Soc.*, **59**:3267, 2011.

[11] S. Mohammadi, A. A. Eftekhar, A. Khelif, H. Moubchir, R. Westafer, W. D. Hunt, and A. Adibi. Complete photonic bandgaps and bandgap maps in two-dimensional silicon photonic crystal plates. *Electron. Lett.*, **43**, 2007.

[12] Grant R. Fowles. *Introduction to Modern Optics*. Dover, New York, 1975.

[13] Pochi. Yeh. *Optical Waves in Layered Media*. Wiley - Blackwell, New York, 1988.

[14] A. Alagappan and P. Wu. Geometrically distributed one-dimensional photonic crystals for light-reflection in all angles. *Optic Express*, **17**:11550–11557, 2009.

[15] O. Painter, R. K. Lee, A. Scherer, A. Yariv, J. D. O'Brien, P. D. Dapkus, and I. Kim. Two-dimensional photonic band-gap defect mode laser. *Science*, **284**:1819, 1999.

[16] A. Mekis, J. C. Chen, I. Kurland, S. Fan, P. R. Villeneuve, and J. D. Joannopoulos. High transmission through sharp bends in photonic crystal waveguides. *Phy. Rev. Lett.*, **77**:3787–3790, 1996.

[17] B. D'Urso, O. Painter, J. O'Brien, T. Tombrello, A. Yariv, and A. Scherer. Modal reflectivity in finite-depth two-dimensional photonic-crystal microcavities. *J. Opt. Soc. Am. B*, **15**:1155–1159, 1998.

[18] J. C. Knight. Photonic crystal fibers. *Nature*, **424**:847, 2003.

[19] K. Nozaki, T. Tanabe, A. Shinya, S. Matsuo, T. Sato, H. Taniyama, and M. Notomi. Sub-femojoule all-optical switching using a photonic-crystal nanocavity. *Nature Photonic*, **4**:477, 2010.

[20] A. Tandaechanurat, S. Ishida, D. Guimard, S. Nomura, M. Iwamoto, and Y. Arakawa. Lasing oscillation in a three-dimensional photonic crystal nanocavity with a compelte bandgap. *Nature Photonics*, **5**:91, 2011.

[21] S. A. Rinne, F. G. Santamaria, and P. V. Braun. Embedded cavities and waveguides in three-dimensional silicon photonic crystals. *Nature Photonics*, **2**:52, 2008.

[22] J. D. Joannopolous, S. G. Johnson, J. N. Winne, and R. D. Meade. *Photonic crystals: Molding the flow of light*. Princeton University, 2008.

[23] M. Boroditsky, R. Vrijen, T. F. Krauss, R. Coccioli, R. Bhat, and E. Yablonovitch. Spontaneous emission extraction and purcell enhancement from thin-film 2d photonic crystals. *J. Lightware Technol*, **17**:2096, 1999.

[24] S. Fan, P. R. Villneuve, and J. D. Joannopoulos. High extraction efficiency of spontaneous emission from slab of photonic crystal. *Phys. Rev. Lett*, **78**:3294, 1997.

[25] Y. Dong, H. Zhao, J. Song, F. Gao, C. Cheng, Y. Chang, G. Du, M. B. Yu, and G. Q Lo. Low threshold two-dimensional organic photonic crystal distributed feedback laser with hexagonal symmetry based on sin. *Appl. Phys. Lett*, **92**:223309, 2008.

[26] L. J. Martínez, B. Alén, I. Prieto, J. F. G. López, M. Galli, L. C. Andreani, C. Seassal, P. Viktorovitch, and P. A. Postigo. Two dimensional surface emitting photonic crystal laser with hybrid triangular-graphite structure. *Opt. Express*, **17**:15043, 2009.

[27] H. Takano, Y. Akahane, T. Asano, and S. Noda. In-plane-type channel drop filter in a two-dimensional photonic crystal slab. *Appl. Phys. Lett.*, **84**:2226, 2004.

[28] A. Sugitatsu, T. Asano, and S. Noda. Line-defect-waveguide laser integrated with a point defect in a two-dimensional photonic crystal slab. *Appl. Phys. Lett.*, **86**:171106, 2005.

[29] Z. Zhang, M. Dainese, L. Wosinski, S. Xiao, and M. Qiu. Optical filter based on two-dimensional photonic crystal surface-mode cavity in amorphous silicon-on-silica struture. *Appl. Phys. Lett.*, **90**:041108, 2007.

[30] M. Makarova, J. Vuckovic, H. Sanda, and Y. Nishi. Silicon-based photonic crystal nanocavity light emitters. *Appl. Phys. Lett.*, **89**:221101, 2006.

[31] J. G. Fleming and S. Y. Lin. Three-dimensional photonic crystal with a stop band from 1.35 to 1.95 μm. *Opt. Lett.*, **24**:49–51, 1999.

[32] S. Noda, K. Tomoda, N. Yamamoto, and A. Chutinan. Full three-dimensional photonic bandgap crystals at near-infrared wavelengths. *Science*, **289**:604–606, 2000.

[33] M. O. Jensen and M. J. Brett. Square spiral 3d photonic bandgap crystals at telecommunications frequencies. *Opt. Express*, **13**:3348, 2005.

[34] P. A. Franken, A. E. Hill, C. W. Peters, and G. Weinreich. Generation of optical harmonics. *Phys. Rev. Lett.*, **7**:118, 1961.

[35] M. M. Fejer, G. A. Magel, D. H. Jundt, and R. L. Byer. Quasi-phase-matched second harmonic generation: tuning and tolerances. *IEEE J. Quantum Electron*, **28**:2631, 1992.

[36] J. A. Armstrong, N. Bloembergen, J. Ducuing, and P. S. Pershan. Interactions between light waves in a nonlinear dielectric. *Phys. Rev.*, **127**:1918, 1962.

[37] P. A. Franken and J. F. Ward. Optical harmonics and nonlinear phenomena. *Rev. Mod. Phys.*, **35**:23, 1963.

[38] V. Berger. Nonlinear photonic crystals. *Phys. Rev. Lett.*, **81**:4136, 1998.

[39] S. Saltiel and Y. S. Kivshar. Phase matching in nonlinear $\chi^{(2)}$ photonic crystals. *Opt. Lett.*, **25**:1204, 2000.

[40] X. H. Wang and B. Y. Gu. Nonlinear frequency conversion in 2d $\chi^{(2)}$ photonic crystals and novel nonlinear double-circle construction. *Eur. Phys. J. B*, **24**:323, 2001.

[41] N. G. R. Broderick, G. W. Ross, H. L. Offerhaus, D. J. Richardson, and D. C. Hanna. Hexagonally poled lithium niobate: A two-dimensional nonlinear photonic crystal. *Phys. Rev. Lett.*, **84**:4345, 2000.

[42] P. Xu, S. H. Ji, S. N. Zhu, X. Q. Yu, J. Sun, H. T. Wang, J. L. He, Y. Y. Zhu, and N. B. Ming. Conical second harmonic generation in a two-dimensional $\chi^{(2)}$ photonic crystal: A hexagonally poled litao3 crystal. *Phys. Rev. Lett.*, **93**:133904, 2004.

[43] C. Canalias, M. Nordlof, V. Pasiskevicius, and F. Laurell. A ktiopo$_4$ nonlinear photonic crystal for blue second harmonic generation. *Appl. Phys. Lett.*, **94**:081121, 2009.

[44] J. Chen and X. Chen. Phase matching in three-dimensional nonlinear photonic crystals. *Phys. Rev. A*, **80**:013801, 2009.

[45] J. Chen and X. Chen. Generation of conical and spherical second harmonics in three-dimensional nonlinear photonic crystals with radial symmetry. *J. Opt. Soc. Am. B*, **28**:241, 2011.

[46] A. V. Balakin, V. A. Bushuev, N. I. Koroteev, B. I. Mantsyzov, I. A. Ozheredov, and A. P. Shkurinov. Enhancement of second-harmonic generation with femtosecond laser pulses near the photonic band edge for different polarizations of incident light. *Opt. Lett.*, **24**:793, 1999.

[47] Y. Dumeige, P. Vidakovic, S. Sauvage, I. Sagnes, and J. A. Levenson. Enhancement of second-harmonic generation on a one-dimensional semiconductor photonic band gap. *Appl. Phys. Lett.*, **78**:3021, 2001.

[48] M. Scalora, M. J. Bloemer, A. S. Manka, J. P. Dowling, C. M. Bowden, R. Viswanathan, and J. W Haus. Pulsed second-harmonic generation in nonlinear, one-dimenstional, periodic structures. *Phys. Rev. A*, **56**:3166, 1997.

[49] D. Antonucci, D. de Ceglia, A. D'Orazio, M. De Sario, V. Marrocco, V. Petruzzelli, and F. Prudenzano. Enhancement of the shg efficiency in a doubly resonant 2d - photonic crystal microcavity. *Opt. Quant. Electron*, **39**:353, 2007.

[50] F. F. Ren, R. Li, C. Cheng, J. Chen, Y. X. Fan, J. Ding, and Wang. H. T. Low - threshold and high - efficiency optical parametric oscillator using a one - dimensional single - defect photonic crystal with quadratic nonlinearity. *Phys. Rev. B*, **73**:033104, 2006.

[51] J. Martorell and R. Corbalan. Enhancement of second harmonic generation on a periodic structure with a defect. *Opt. Commun.*, **108**:319, 1994.

[52] P. Rochon, E. Batalla, and A. Natansohn. Optically induced suface gratings on azoaromatic polymer films. *Appl. Phys. Lett.*, **66**:136, 1995.

[53] D. Y. Kim, S. K. Tripathy, L. Li, and J. Kumar. Laser-induced holographic surface relief gratings on nonlinear optical polymer films. *Appl. Phys. Lett.*, **66**:1166, 1995.

[54] G. L. Yurista, A. A. Friesem, E. Pawlowski, L. Kuller, R. Ludwig, H. G. Weber, A. Donval, E. Toussaere, and J. Zyss. Hybrid semiconductor polymer resonant grating waveguide structures. *Opt. Mater.*, **17**:149, 2001.

[55] T. Matsui, M. Ozaki, K. Yoshino, and F. Kajzar. Fabrication of flexible distributed feedback laser using photoinduced surface relief grating on azo-polymer film as a template. *Japanese J. Appl. Phys.*, **41**:1386, 2002.

[56] C. Ye, K. Y. Wong, Y. He, and X. Wang. Distributed feedback sol-gel zirconia waveguide lasers based on surface relief gratings. *Opt. Express*, **15**:936, 2007.

[57] G. Kranzelbinder, E. Toussaere, D. Josse, and J. Zyss. Progress in erasable and permanent polymer based dfb-structures with multicolour tunable laser emission. *Synthetic Metals*, **121**:1617, 2001.

[58] D. Wright, E. Brasselet, J. Zyss, G. Langer, A Pogantsch, K. F. Iskra, T. Neger, and W. Kern. All-optical tunability of holographically multiplexed organic distributed feedback lasers. *Opt. Express*, **12**:325, 2004.

[59] D. Wright, E. Brasselet, J. Zyss, G. Langer, and W. Kern. Dye-doped organic distributed-feedback lasers with index and surface gratings: the role of pump polarization and molecular orientation. *J. Opt. Soc. Am. B*, **21**:944, 2005.

[60] F. Lemarchand, A. Sentenac, E. Cambrill, and H. Giovannini. Study of the resonant behaviour of waveguide gratings: increasing the angular tolerance of guided-mode filters. *J. Opt. A: Pure Appl. Opt.*, **1**:545, 1999.

[61] M. Siltanen, S. Leivo, P. Voima, M. Kauranen, P. Karvinen, P. Vahimaa, and M. Kuittinen. Strong enhancement of second-harmonic generation in all-dielectric resonant waveguide grating. *Appl. Phys. Lett*, **91**:111109, 2007.

[62] A. Saari, G. Genty, M. Siltanen, P. Karvinen, P. Vahimaa, M. Kuittinen, and M. Kauranen. Giant enhancement of second-harmonic generation in multiple diffraction orders from sub-wavelength resonant waveguide grating. *Opt. Express*, **18**:12298, 2010.

[63] A. C. Edrington, A. M. Urbas, P. Derege, C. X. Chen, T. M. Swager, N. Hadjichristidis, M. Xenidou, L. J. Fetters, J. D. Joannopoulos, Y. Fink, and E. L. Thomas. Polymer-based photonic crystals. *Adv. Mater.*, **6**:421, 2001.

[64] C. Paquet and E. Kumacheva. Nanostructured polymers for photonics. *Materials today*, **11**:48, 2008.

[65] G. V. Freymann, A. Ledermann, M. Thiel, I. Staude, S. Essig, K. Busch, and M. Wegener. Three-dimensional nanostructures for photonics. *Adv. Funct. Mater.*, **20**:1038, 2010.

[66] Microchem. http://www.microchem.com/pdf/su-82000datasheet2100and2150ver5.pdf.

[67] A. Katchalsky. Rapid swelling and deswelling of reversible gels of polymeric acids by ionization. *Exper.*, **5**:319, 1949.

[68] P. J. Cottinet, D. Guyomar, B. Guiffard, L. Lebrun, and C. Putson. *Electrostrictive polymers as high-performance electroactive polymers for energy harvesting.* InTech, 2010.

[69] A. Natansohn and P. Rochon. Photoinduced motions in azobenzene-based amorphous polymers: Possible photonic devices. *Adv. Mater.*, **11**:1387, 1999.

[70] R. R. Rojo, S. Yamada, H. Matsuda, and D. Yankelevich. Large near-resonance third-order nonlinearity in an azobenzene functionalized polymer film. *Appl. Phys. Lett.*, **72**:1021, 1998.

[71] T. Ikeda and Y. Wu. Photoinduced alignment behavior of polymer liquid crystals containing azobenzene moieties in the side chain. *Pure. Appl. Chem.*, **71**:2131, 1999.

[72] T. Ikeda. Photomodulation of liquid crystal orientations for photonic applications. *J. Mater. Chem.*, **13**:2037, 2003.

[73] J. A. Delaire and K. Natakani. Linear and nonlinear optical properties of photochromic molecules and materials. *Chem. Rev.*, **100**:1817, 2000.

[74] E. Yablonovitch, T. J. Gmitter, and K. M. Leung. Photonic band structure: The face-centered-cubic case employing nonspherical atoms. *Phys. Rev. Lett*, **67**:2295, 1991.

[75] T. F. Krauss and S. De la rue, R. M. an Brand. Two-dimensional photonic-bandgap structures operating at near-infrared wavelengths. *Nature*, **383**:699, 1996.

[76] K. O. Hill, B. Malo, F. Bilodeau, D. C. Johnson, and J. Albert. Bragg gratings fabricated in monomode photosensitice optical fiber by uv exposure through a phase mask. *Appl. Phys. Lett.*, **62**:1035, 1993.

[77] D. Xu, K. P. Chen, K. Ohlinger, and Y. Lin. Nanoimprinting lithography of a two-layer phase mask for three-dimensional photonic structure holographic fabrications via single exposure. *Nanotechnology*, **22**:035303, 2011.

[78] C. Vieu, F. Carcenac, A. Pepin, Y. Chen, M. Mejias, A. Lebib, L. Manin-Ferlazzo, L. Couraud, and H. Launois. Electron beam lithography: resolution limits and applications. *Appl. Suf. Science*, **164**:111, 2000.

[79] S. Y. Chou, P. R. Krauss, and P. J. Renstrom. Nanoimprint lithography. *J. Vac. Sci. Technol. B*, **14**:4129, 1996.

[80] H. Hatate, M. Hashimoto, H. Shirakawa, Y. Fujiwara, Y. Takeda, H. Nakano, and T. Tatsut. Fabrication of inp submicron pillars for two-dimensional photonic crystals by reactive ion etching. *Jpn. J. Appl. Phys.*, **37**:7172, 1998.

[81] A. Mata, A. Fleischman, and S. Roy. Fabrication of multi-layer su8 microstructures. *J. Micromech. Microeng*, **16**:276, 2006.

[82] H. B. Sun, S. Matsuo, and Misawa. H. Three-dimensional photonic crystal structures achieved with two-photon absorption photopolymerization of resin. *Appl. Phys. Lett.*, **87**:786, 1999.

[83] M. Straub and M. Gu. Near-infrared photonic crystals with higher-order bandgaps generated by two-photon photopolymerization. *Opt. Lett.*, **27**:1824, 2002.

[84] M. Deubel, G. V. Freymann, M. Wegener, S. Pereira, K. Busch, and C. M. Soukoulis. Direct laser writing of three-dimensional photonic-crystal templates for telecommunications. *Nature mat.*, **3**:444, 2004.

[85] M. T. Do, T. T. N. Nguyen, Q. Li, H. Benisty, I. L. Ledoux-Rak, and N. D. Lai. Submicrometer 3d structures fabrication enabled by one-photon absorption direct laser writing. *Opt. Express*, **21**:20964, 2013.

[86] N. D Lai, W. P. Liang, J. H. Lin, C. C. Hsu, and C. H. Lin. Fabrication of two- and three-dimensional periodic structures by multi-exposure of two-beam interference technique. *Opt. Express*, **13**:9605, 2005.

[87] N. D. Lai, T. S. Zheng, D. B. Do, J. H. Lin, and C. C. Hsu. Fabrication of desired three-dimensional structures by holographic assembly technique. *Appl. Phys. A*, **100**:171, 2010.

[88] V. Berger, O. G. Lafaye, and E. Costard. Photonic band gaps and holography. *J. Appl. Phys*, **82**:60–64, 1997.

[89] M. Campbell, D. N. Sharp, R. G. Harrison, M. T. Denning, and A. J. Turberfield. Fabrication of photonic crystals for the visible spectrum by holographic lithography. *Nature*, **404**:53, 2000.

[90] S. Shoji and S. Kawata. Photofabrication of three-dimensional photonic crystals by multibeam laser interference into a photopolymerizable resin. *Appl. Phys. Lett.*, **76**:2668, 2000.

[91] E. G. Loewen and E. Popov. *Diffraction gratings and applications*. New York: Dekker, 1997.

[92] A. Yariv and M. Nakamura. Periodic structures for integrated optics. *IEEE J. Quantum Electron.*, **13**:233, 1977.

[93] P. E. Dyer, R. J. Farley, and R. Giedl. Analysis of grating formation with excimer laser irradiated phase masks. *Opt. Commun.*, **115**:327, 1995.

[94] V. Berger, O. G. Lafaye, and E. Costard. Silicon periodic structures and their liquid crystal composites. *Solid State Phenomena*, **156 - 158**:547, 2010.

[95] G. Barillaro, A. Diligenti, M. Benedetti, and S. Merlo. Silicon micromachined periodic structures for optical applications at $\lambda = 1.55$ μm. *Appl. Phys. Lett*, **89**:151110, 2006.

[96] X. L. Yang, L. Z. Cai, and Y. R. Wang. Larger bandgaps of two-dimensional triangular photonic crystals fabricated by holographic lithography can be realized by recording geometry design. *Opt. Express*, **12**:5850, 2004.

[97] W. Pang, L. Nakagawa and Y. Fainman. Fabrication of two-dimensional photonic crystals with controlled defects by use of multiple exposures and direct write. *Appl. Opt.*, **42**:5450, 2003.

[98] A. Shishido, I. B. Diviliansky, I. C. Khoo, and T. S. Mayer. Direct fabrication of two-dimensional titania arrays using interference photolithography. *Appl. Phys. Lett.*, **79**:3332, 2001.

[99] I. B. Diviliansky, A. Shishido, I. C. Khoo, and T. S. Mayer. Fabrication of two-dimensional photonic crystals using interference lithography and electrodeposition of cdse. *Appl. Phys. Lett.*, **79**:3392, 2001.

[100] G. Lee, S. H. Song, C. H. Oh, and P. S Kim. Arbitrary structuring of two-dimensional photonic crystals by use of phase-only fourier gratings. *Opt. Lett*, **29**:2539, 2004.

[101] D. Ambrosini, F. Gori, and D. Paoletti. Destructive interference from three partially coherent point sources. *Opt. Commun.*, **254**:30–39, 2005.

[102] N. D. Lai, J. H. Lin, and C. C. Hsu. Fabrication of highly rotational symmetric quasi-periodic structures by multiexposure of a three-beam interference technique. *Appl. Opt.*, **46**:5645, 2007.

[103] N. D. Lai, J. H. Lin, D. B. Do, W. P. Liang, Y. D. Huang, T. S. Zheng, Y. Y. Huang, and C. C. Hsu. *Fabrication of two- and three-dimensional photonic crystals*

and photonic quasi-crystals by interference technique, chapter 12, pages 253–278. Holography, Research and Technologies. INTECH, 2011.

[104] Y. C. Zhong, S. A. Zhu, H. M. Su, H. Z. Wang, J. M. Chen, Z. H. Zeng, and Y. L. Chen. Photonic crystal with diamondlike structure fabricated by holographic lithography. *Appl. Phys. Lett.*, **87**:061103, 2005.

[105] N. D. Lai, J. H. Lin, Y. Y. Huang, and C. C. Hsu. Fabrication of two- and three-dimensional quasi-periodic structures with 12-fold symmetry by interference technique. *Opt. Express*, **14**:10746, 2006.

[106] L. Wu, Y. Zhong, C. T. Chan, and K. S. Wong. Fabrication of large area two- and three- dimensional polymer photonic crystals using single refracting prism holographic lithography. *Appl. Phys. Lett.*, **86**:241102, 2005.

[107] J. Chen, Jiang. W., X. Chen, L. Wang, S. Zhang, and R. T. Chen. Holographic three-dimensional polymeric photonic crystals operating in the 1550 nm window. *Appl. Phys. Lett.*, :093102, 2007.

[108] X. Wu. *Fabrication of 1D, 2D and 3D polymer-based periodic structures by mass transport effect*. PhD thesis, Ecole Normale Superieure de Cachan, 2013.

[109] M. Loncar, D. Nedeljkovic, T. Doll, J. Vuckovic, A. Scherer, and T. P. Pearsall. Waveguiding in planar photonic crystals. *Appl. Phys. Lett.*, **77**:1937, 2000.

[110] A. Chutinan and S. Noda. Waveguides and waveguide nebds in two-dimensional photonic crystal slabs. *Phys. Rev. B*, **62**:4488, 2000.

[111] Y. Akahane, T. Asano, B. S. Song, and S. Noda. High-q photonic nanocavity in a two-dimensional photonic crystal. *Nature*, **425**:944, 2003.

[112] T. T. N Nguyen, Q. L. Nguyen, J. Zyss, I. Ledoux-Rak, and N. D. Lai. Optimization of thickness and uniformity of photonic structures fabricated by interference lithography. *Appl. Phys. A*, **111**:279, 2013.

[113] S. W Lee and S. S Lee. Application of huygens-fresnel diffraction principle for high aspect ratio su8 micro-/nanotip array. *Opt. Lett*, **33**:40–42, 2008.

[114] T. A. Anhoj, A. M. Jorgensen, D. A. Zauner, and J. Hubner. The effect of soft bake temperature on the polymerization of su-8 photoresist. *J. Micromech. Microeng.*, **16**:1819, 2006.

[115] J. Dubendorfer and R. E. Kunz. Compact integrated optical immunosensor using replicated chirped grating coupler sensor chips. *Appl. Opt.*, **37**:1890, 1998.

[116] M. Wiki and R. E. Kunz. Wavelength-interrogated optical sensor for biochemical applications. *Opt. Lett.*, **25**:463, 2000.

[117] Z. Hegedus and R. Netterfield. Low sideband guided-mode resonant filter. *Appl. Opt.*, **39**:1469, 2000.

[118] D. L. Brundrett, E. N. Glytsis, and T. K. Gaylord. Normal incidence guided-mode resonant grating filters: design and experimental demonstration. *Opt. lett.*, **23**:700, 1998.

[119] N. Rajkumar and J. N. McMullin. V-groove gratings on silicon for infrared beam splitting. *Appl. Opt.*, **34**:2556, 1995.

[120] X. Zhu, Y. Xu, and S. Yang. Distortion of 3d su8 photonic structures fabricated by four-beam holographic lithography with umbrella configuration. *Opt. Express*, **15**:16546, 2007.

[121] Q. Sun, S. Juodkazis, N. Murazawa, V. Mizeikis, and H. Misawa. Freestanding and movable photonic microstructures fabricated by photopolymerization with femtosecond laser pulses. *J. Micromech. Microeng*, **20**:035004, 2010.

[122] D. C. Meisel, M. Diem, M. Deubel, F. Perez-Willard, S. Linden, D. Gerthsen, K. Busch, and M. Wegener. Shrinkage precompensation of holographic three-dimensional photonic-crystal templates. *Adv. Mater.*, **18**:2964, 2006.

[123] M. T. Do. *Fabrication of submicrometer 3D structures by one-photon absorption direct laser writing and applications.* PhD thesis, Ecole Normale Superieure de Cachan, 2015.

[124] T. M. de Jong, D. K. G. de Boer, and C. W. M Bastiaansen. Surface-relief and polarization gratings for solar concentrators. *Opt. Express*, **19**:15127, 2011.

[125] D. B. Do. *Fabrication of optical functional micro/nano periodic structures based on holographic lithography and direct laser writing technique*. PhD thesis, National Chung Cheng University, 2014.

[126] S. I. Chang, J. B. Yoon, H. Kim, J. J. Kim, B. K. Lee, and D. H. Shin. Microlens array diffuser for a light-emitting diode backlight system. *Opt. Lett.*, **31**:3016, 2006.

[127] C. Y. Wu, T. H. Chiang, and C. C. Hsu. Fabrication of microlens array diffuser films with controllable haze distribution by combination of breath fugures and replica molding methods. *Opt. Express*, **16**:19978, 2008.

[128] M. K. Wei and I. L. Su. Method to evaluate the enhancement of luminance efficency in planar oled light emitting devices for microlens array. *Opt. Express*, **12**:5777, 2004.

[129] C. J. Barrett, A. L. Natansohn, and P. L. Rochon. Mechanism of optically inscribed hing-efficiency diffraction gratings in azo polymer films. *J. Phys. Chem.*, **100**:8836, 1996.

[130] C. J. Barrett, P. L. Rochon, and A. L. Natansohn. Model of laser-driven mass transport in thin films of dye-functionalized polymers. *J. Chem. Phys.*, **109**:1505, 1998.

[131] T. G. Pedersen and P. M. Johansen. Mean-field theory of photoinduced molecular reorientaion in azobenzene liquid crystalline side-chain polymers. *J. Chem. Phys.*, **79**:2470, 1997.

[132] T. G. Pedersen, P. M. Johansen, N. C. R. Holme, P. S. Ramanujam, and S. Hvilsted. Mean-field theory of photoinduced formation of surface reliefs in side-chain azobenzene polymers. *J. Chem. Phys.*, **80**:89, 1998.

[133] P. lefin, C. Fiorini, and J. M. Nunzi. Anisotropy of the photoinduced translation diffusion of azo-dyes. *Opt. Mater.*, **9**:323, 1998.

[134] X. Wu, T. T. N. Nguyen, I. Ledoux-Rak, C. T. Nguyen, and N. D. Lai. *Optically accelerated formation of one- and two-dimensional holographic surface relief gratings on DR1/PMMA*, chapter 7. Holography - Basic Principles and Contemporary Applications. INTECH, 2013.

[135] P. Rochon, A. Natansohn, C. L. Callender, and L. Robitaille. Guided mode resonance filters using polymer films. *Appl. Phys. Lett.*, **71**:1008, 1997.

[136] M. Schmitz, R. Brauer, and O. Bryngdahl. Grating in the resonance domain as polarizing splitters. *Opt. Lett.*, **20**:1830, 1995.

[137] J. A. Giordmaine. Mixing of light beams in crystals. *Phys. Rev. Lett.*, **8**:19, 1962.

[138] P. D. Maker, R. W. Terhune, M. Nisenoff, and C. M. Savage. Effects of dispersion and focusing on the production of optical harmonics. *Phys. Rev. Lett.*, **8**:21, 1962.

[139] D. B. Anderson and J. T. Boyd. Wideband co_2 laser second harmonic generation phase matched in gaas thin-film waveguides. *Appl. Phys. Lett.*, **19**:266, 1971.

[140] J. P. van der Ziel, R. C. Miller, R. A. Logan, W. A. Nordland, and R. M. Mikulyak. Phase-matched second-harmonic generation in gaas optical waveguides by focused laser beams. *Appl. Phys. Lett.*, **25**:238, 1974.

[141] O. E. Martinez. Achromatic phase matching for second harmonic generation of femtosecond pulses. *IEEE J. Quant. Electron.*, **25**:2464, 1989.

[142] S. Kurimura, Y. Kato, M. Maruyama, Y. Usui, and H. Nakajima. Quasi-phase-matched adhered ridge waveguide in $linbo_3$. *Appl. Phys. Lett.*, **89**:191123, 2006.

[143] Y. Y. Zhu, X. J. Zhang, Y. Q. Lu, Y. F. Chen, S. N. Zhu, and N. B. Ming. New type of polariton in a piezoelectric superlattice. *Phys. Rev. Lett.*, **90**:053903, 2003.

[144] L. A. Eyres, P. J. Tourreau, T. J. Pinguet, C. B. Ebert, J. S. Harris, M. M. Fejer, L. Becouarn, B. Gerard, and E. Lallier. All-epitaxial fabrication of thick, orientation-patterned gaas films for nonlinear optical frequency conversion. *Appl. Phys. Lett.*, **79**:904, 2001.

[145] G. Martin, O. Alibart, R. Hierle, D. Josse, P. Baldi, and J. Zyss. Influence of the photodepoling parameters on quasiphase-matched second-harmonic generation and optical parametric fluorescence in polymer channel waveguides. *J. Appl. Phys.*, **96**:7112, 2004.

[146] C.-C. Hsu L.-H. Peng and Y.-C. Shih. Second-harmonic green generation from two-dimensional $\chi_{(2)}$ nonlinear photonic crystal with orthorhombic lattice structure. *Appl. Phys. Lett.*, **83**:3447, 2003.

[147] A. Chowdhury, C. Staus, B. F. Boland, T. F. Kuech, and L. McCaughan. Experimental demonstration of 1535–1555-nm simultaneous optical wavelength interchange with a nonlinear photonic crystal. *Opt. Lett.*, **26**:1353, 2001.

[148] Y. Zhang, Z. D. Gao, Z. Qi, S. N. Zhu, and N. B. Ming. Nonlinear cerenkov radiation in nonlinear photonic crystal waveguides. *Phys. Rev. Lett.*, **100**:163904, 2008.

[149] M. Yamada and K. Kishima. Fabrication of periodically reversed domain structure for shg in linbo$_3$ by direct electron beam lithography at room temperature. *Electron. Lett.*, **27**:828, 1991.

[150] L. E. Myers, R. C. Eckardt, M. M. Fejer, R. L. Byer, W. R. Bosenberg, and J. W. Pierce. Quasi-phase-matched optical parametric oscillators in bulk periodically poled linbo$_3$. *J. Opt. Soc. Am. B*, **12**:2102, 1995.

[151] G. Rosenman, P. Urenski, A. Agronin, Y. Rosenwaks, and M. Molotskii. Submicron ferroelectric domain structures tailored by high-voltage scanning probe microscopy. *Appl. Phys. Lett.*, **82**:103, 2003.

[152] G. L. J. A. Rikken, C. J. E. Seppen, S. Nijhuis, and E. W. Meijer. Poled polymers for frequency doubling of diode lasers. *Appl. Phys. Lett.*, **58**:435, 1991.

[153] X. Ni, M. Nakanishi, O. Sugihara, and N. Okamato. Fabrication of $\chi^{(2)}$ grating in poled polymer waveguide based on direct laser beam writing. *Opt. Rev.*, **5**:9, 1998.

[154] J. H. Lin, N. D. Lai, C. H. Chiu, C. Y. Lin, G. W. Rieger, J. F. Young, F. S. S. Chien, and C. C. Hsu. Fabrication of spatial modulated second order nonlinear

structures and quasi-phase matched second harmonic generation in a poled azo-copolymer planar waveguide. *Opt. Express*, **16**:7832, 2008.

[155] O. Sugihara, M. Nakanishi, Y. Che, C. Egami, Y. Kawata, and N. Okamoto. Single-pulse ultraviolet laser recording of periodically poled structures in polymer thin films. *Appl. Opt.*, **39**:5632, 2000.

[156] S. Tomaru, T. Watanabe, M. Hikita, M. Amano, Y. Shuto, I. Yokohama, T. Kaino, and M. Asobe. Quasi-phase-matched second harmonic generation in a polymer waveguide with a periodic poled structure. *Appl. Phys. Lett.*, **68**:1760, 1996.

[157] Y. H. Liu, X. J. Lv, Z. D. Xie, X. P. Hu, Y. Yuan, J. Lu, L. N. Zhao, G. Zhao, and S. N. Zhu. Amplification assisted optical parametric oscillator in the mid-infrafed region. *Appl. Phys. B*, **11**:4695, 2011.

[158] J. Zimmermann, J. Struckmeier, M. R. Hofmann, and J. P. Meyn. Tunable blue laser basaed on intracavity frequency doubling with a fan-structured periodically poled litao$_3$ crystal. *Opt. Lett.*, **27**:604, 2002.

[159] J. Feng, Y. Y. Zhu, and N. B. Ming. Harmonic generations in an optical fibonacci superlattice. *Pyhs. Rev. B*, **41**:5578, 1990.

[160] S. N. Zhu, Y. Y. Zhu, and N. B. Ming. Quasi-phase-matched third-harmonic generation in a quasi-periodic optical superlattice. *Science*, **278**:843, 1997.

[161] B. Y. Gu, B. Z. Dong, Y. Zhang, and G. Z. Yang. Enhanced harmonic generation in aperiodic optical superlattices. *Appl. Phys. Lett.*, **75**:2175, 1999.

[162] B. Y. Gu, Y. Zhang, and B. Z. Dong. Investigations of harmonic generations in aperiodic optical superlattices. *J. Appl. Phys.*, **87**:7629, 2000.

[163] A. Arie, N. Habshoosh, and A. Bahabad. Quasi phase matching in two-dimensional nonlinear photonic crystals. *Opt. Quant. Electron*, **39**:361, 2007.

[164] H. Karlsson and F. Laurell. Electric field poling of flux grown ktiopo$_4$. *Appl. Phys. Lett.*, **71**:3474, 1997.

[165] V. Taggi, F. Michelotti, M. Bertolotti, G. Petrocco, V. Foglietti, A. Donval, E. Toussaere, and J. Zyss. Domain inversion by pulse poling in polymer films. *Appl. Phys. Lett.*, **72**:2794, 1998.

[166] S. Yilmaz, S. Bauer, and R. G. Multhaupt. Photothermal poling of nonlinear optical polymer films. *Appl. Phys. Lett.*, **64**:2770, 1995.

[167] S. M. Saltiel, D. N. Neshev, W. Krolikowski, A. Arie, O. Bang, and Y. S. Kivshar. Multiorder nonlinear diffraction in frequency doubling processes. *Opt. Lett.*, **34**:848, 2009.

[168] S. M. Saltiel, Y. Sheng, N. V. Bloch, D. N. Neshev, W. Krolikowski, A. Arie, K. Koynov, and Y. S. Kivshar. Cerenkov-type second-harmonic generation in two-dimensional nonlinear photonic structures. *IEEE J. Quantum Electron.*, **45**:1465, 2009.

[169] T. Katchalski, G. L. Yurista, A. A. Friesem, G. Martin, R. Hierle, and J. Zyss. Light modulation with electro-optic polymer-based resonant grating waveguide structures. *Opt. Express*, **13**:4645, 2005.

[170] R. J. Stockermans and P. L. Rochon. Narrow-band resonant grating waveguide filters constructed with azobenzene polymers. *Appl. Opt*, **38**:3714, 1999.

[171] A. Mizutani, H. Kikuta, and K. Iwata. Numerical study in an asymmetric guided-mode rasonant grating with a kerr medium for optical switching. *J. Opt. Soc. Am. A*, **22**:355, 2005.

[172] D. Wawro, S. Tibuleac, R. Magnusson, and H. Liu. Optical fiber endface biosensor on resonances in dielectric waveguide gratings. *Proc. SPIE*, **3911**:86, 2000.

[173] P. Karvinen, T. Nuutinen, O. Hyvarinen, and P. Vahimaa. Enhancement of laser-induced fluorescence at 473 nm excitation with subwavelength resonant waveguide gratings. *Opt. Express*, **16**:16364, 2008.

[174] T. Katchalski, E. Teitelbaum, and A. A. Friesem. Towards ultranarrow bandwidth polymer-based resonant grating waveguide structures. *Appl. Phys. Lett.*, **84**:472, 2004.

[175] A. Donval, E. Toussaere, J. Zyss, G. L. Yurista, E. Jonsson, and A. A. Friesem. Novel polymer-based resonant grating-waveguide structures. *Synthetic Metals*, **124**:19, 2001.

[176] S. S. Wang and R. Magnusson. Theory and applications of guide-mode resonance filters. *Appl. Opt*, **32**:2606, 1993.

[177] A. Taflove and Hagness. S. C. *Computational electrodynamics: The Finite-difference time- domain method*. Artech House, 2005.

[178] Y. Hao and R. Mittra. *FDTD modeling of metamaterials: Theory and applications*. Artech House, 2008.